Faculty of Science and Engineering

School of Electrical Engineering, Computing and Mathematical Sciences

Broadband Echosounder Calibration and Processing for Frequency Dependent Target Strength and Phase Measurements

Arti Verma

This thesis is presented for the Degree of

Doctor of Philosophy

of

Curtin University

October 2019

Declaration of authorship

I Arti Verma, declare to the best of my knowledge that this thesis contains no material previously published by any other person except where due acknowledgement has been made.

This thesis contains no material which has been accepted for award of any other degree or diploma in any university.

All the data collection and experiments conducted in relation to the PhD were performed according to the Australian Code of Practise and the use of animals for scientific purpose.

Date 15/10/2019

Dedication

This thesis is dedicated to the two pillars of my life Rohan, and Punit.

Epigraph

"There's nothing wrong with enjoying looking at the surface of the ocean itself,
except that when you finally see what goes on underwater,
you realize that you've been missing the whole point of the ocean.
Staying on the surface all the time is like going to the circus
and staring at the outside of the tent."

— **Dave Barry**

Dreams are not those which comes while we are sleeping,
but dreams are those when you don't sleep before fulfilling them."

— **A.P.J. Abdul Kalam**

Abstract

The interpretation of backscattered echoes collected by a broadband echosounder is a challenge due to the complicated dynamics of the acoustic scatterers, the surrounding environment and the complexity of the system. This thesis aims to address these challenges by examining four particular aspects: 1) calibration of echosounder for target strength measurements; 2) characterisation of the geometrical and directional properties of the transducer; 3) extraction of the target phase and calibration of the echosounder for the target phase measurements; and finally, 4) the application of the three methods to obtain the acoustic signatures of in-situ marine organisms.

An algorithm was developed to calibrate the echosounder using the transducer system response as a function of frequency and the off-axis angle. The echosounder was calibrated for target strength by exclusively using the amplitude part of the system response. Whereas the same instrument was calibrated for the target phase by utilising the system response in the complex form.

A series of experiments were conducted offshore in Hobart using the Simrad EK80 scientific echosounder set to two transmission ramp settings' fast' and 'slow'. In accordance with a standard calibration set up, two spheres were used. Off-axis measurements were compensated using the system response calculated for the corresponding position. When compared to the compensation achieved with standard beam pattern model (modified Bessel function), the results exhibited a lower Root Mean Residual Error for both spheres at both ramps. As an advantage, the method did not need an evaluation of the effective beamwidth and took into account any variation from the nominal value.

Later the optimum geometrical parameter (the ratio of the distance between two centres and the radius) and the directional parameters (beamwidth and the beam pattern) of the transducer were determined. The method used an inversion approach by minimising the sum of the square of the difference between the measured and the modelled beam pattern. Minor variation in the parameters was observed from the respective nominal value. The results also confirmed the assumption of the broadband transducer as a transducer of a constant geometrical parameter.

Further, in a novel approach by using the complex system response, the broadband

echosounder was calibrated for the phase measurements. Three different variables were introduced to visualise the phase; absolute, differential and the residual phases. The frequency response of all the three-phase variables exhibited insensitivity to the target position within the acoustic beam and to the ramping of the transmit pulse. In spite of complications in signal processing, the differential and residual phase spectra agreed to the theoretically predicted value. This is significant as it confirms that the broadband echosounder can be confidently used to measure the target's phase response

The research uses the data from the two scientific surveys conducted onboard the *RV Investigator* in the Great Australian Bight region and the Southern Ocean. During the investigations, a set of simultaneous acoustic and optics data were collected from the mesopelagic depths (~200 – 1000 m) of the regions. Exploiting the developed techniques, the frequency spectrum of the target strength and the residual phase of the in-situ targets were obtained. A unique 3D spatial transformation technique was designed to provide ground-truthing to the single targets detected on the echogram in the still image. It was a complicated procedure as it involved three different coordinate systems (echosounder, world and camera) and technical operations such as rotation, translation, and scaling. Multiple targets were successively matched to their concurrent image. Through examples, the acoustic signature of three optically verified organisms; a squid, fish and gas inclusion targets were drawn.

The frequency response of the target strength and the residual phase of a spherical target was matched to the prediction, an inclusive numerical scattering model that predicted both the signal amplitude and phase. For a given set of parameters, the target strength-frequency response was matched to the measured value and for the same set of parameters, the residual phase spectra also matched to the predicted output. This result verified the concept of a target-induced phase distortion as a possible classifier and its potential application in the remote identification of marine organisms.

Acknowledgements

I would like to thank my supervisor Dr Alec Duncan for his support and guidance. His expertise in the use of physics-based principles in solving real-life problems has been an inspiration and a strong motivation during the course of my PhD. During the supervisory process, Dr Duncan ensured that we met on a regular basis to discuss my progress in order to achieve my research goals. It has been an honour to work under his guidance, and I look forward to working with him in the future.

I want to acknowledge the supervision and funding provided by my co-supervisor, Dr Rudy Kloser. His proficiency in the practical and theoretical aspects of ecosystem acoustics offered invaluable support. I am thankful to him for sharing his time and knowledge, providing opportunities to participate in scientific surveys and have access to state of the art technologies and associated data sets for use in this thesis.

I am indebted to Dr Igor Bray, who welcomed me to the Curtin University and provided valuable advice and encouragement on pursuing research when I moved to Australia.

I would like to thank the Federal Government of Australia for the Australian Postgraduate Award (APA) for the research scholarship. Special thanks to the Curtin University for the top-up scholarship which made my student life easier. The research funding from the Great Australian Bight Research program (GARBP) is also greatly acknowledged. Furthermore, I would like to thank the committee members of the GARBP for their constructive input.

I would like to express my gratitude to the acoustic team at CSIRO, Hobart for the help they provided me whilst I resided in Hobart and during the surveys. Tim Ryan offered unconditional support and technical guidance during the setting of my experiment. Haris Kunnath, Gordan Keith, Caroline Sutton, Ryan Downie, and Jeff Cordell are thanked for help during the surveys.

The planning and collection of data were enabled by the contribution of several people from different backgrounds. I would especially like to mention Matt Sherlock, who designed and modified the platforms to accommodate the acoustic and optics sensors. Thanks also to the crewmembers of the *RV Investigator* who worked hard through the day and night for the deployments.

I wish to thank the Echoview team for providing the software, especially Toby Jarvis and Briony Hutton. Special thanks go to Lars Nonboe from Simrad for offering the Matlab software package to process the Simrad EK80 broadband raw data.

Thank you Montserrat Landero, and Bec Wellard for the countless laughter, emotional support and gallons of coffee that we drunk in the name of achieving a PhD. Thanks to my friends Sven Gastauer and Sylvia Parsons for the fun we had together in the last four years.

I am grateful to my family for the unwavering support and love they provided. They stood like a backbone supporting me as I chased my dream. A big hug to my Mom and Dad, who flew from India to help me during the time I was struggling to manage home and work.

My son Rohan was the ray of hope whenever I struggled with this thesis. During my PhD, he transformed from a young boy to a matured teenager who would always motivate me to work hard.

Above all, thanks to my husband Punit, who was my trust, cushion, critic and biggest inspiration behind this PhD. He stood like a pillar behind me to make this PhD a reality. His belief in my strength and capabilities always inspired me to move ahead.

List of publications

Verma, A., Kloser, R. J., & Duncan, A. J. (2017). Potential use of broadband acoustic methods for micronekton classification. *Acoustics Australia, 45*(2), 353-361. https://doi.org/10.1007/s40857-017-0105-8

Conference paper included as a part of the thesis

Verma, A., Duncan, Alec, Kloser, Rudy J. (2016). *Developing active broadband acoustic methods to investigate the pelagic zone of the Great Australian Bight.* Paper presented at the 2nd Australasian Acoustical Societies Conference, ACOUSTICS 2016.

Statement of candidate contribution

Chapter 3: Calibration and Compensation of Off-axis Measurements of a Broadband Echosounder using the System Response

Contributors	Statement of contribution
Arti Verma	Wrote the manuscript, developed the algorithm for data processing, Wrote the codes and conducted the experiment and performed data analysis
Alec Duncan	Helped in the theoretical development of the method and algorithm development and reviewed the manuscript.
Rudy Kloser	Principle investigator of instrumentation for the experiment, supervised the experiment, guided analysis, interpretation and reviewed the manuscript.

Chapter 4: A Measurement Model Approach to Characterise a Broadband Split-beam Transducer.

Contributors	Statement of contribution
Arti Verma	Wrote the manuscript, developed the algorithm for data processing, wrote the codes, conducted the experiment and performed data analysis
Alec Duncan	Helped in the theoretical development of the method and algorithm development and reviewed the manuscript.
Rudy Kloser	Principle investigator of instrumentation supervised the experiment, guided analysis, interpretation and reviewed the manuscript.

Chapter 5: A Technique for Target Phase Extraction and Calibration of a Broadband Echosounder.

Contributors	Statement of contribution
Arti Verma	Wrote the manuscript, developed the algorithm for data processing, wrote the codes, conducted the experiment and performed data analysis.
Alec Duncan	Helped in the theoretical development of the method and algorithm development and reviewed the manuscript.
Rudy Kloser	Principle investigator of instrumentation and at sea voyage time, supervised the experiment, guided analysis and reviewed the manuscript.

Chapter 6: Potential use of Broadband Acoustic Methods for Micronekton Classification.

Contributors	Statement of contribution
Arti Verma	Wrote the manuscript, developed the algorithm for data processing, wrote the codes, conducted the experiment and performed data analysis.
Alec Duncan	Helped in the theoretical development of the method and algorithm development and reviewed the manuscript.
Rudy Kloser	Principle Investigator of the survey and supervised data collection, guided analysis, interpretation and reviewed the manuscript.

Chapter 7: In situ Target Strength and Target Phase Measurements of Optically Verified Micronekton.

Contributors	Statement of contribution
Arti Verma	Wrote the manuscript, developed the algorithm for data processing, Wrote the codes, conducted the experiment and performed data analysis.
Alec Duncan	Helped in the theoretical development of the method and algorithm development and reviewed the manuscript.
Rudy Kloser	Principle investigator for instrumentation and survey, supervised experiments, data collection, guided analysis, interpretation and reviewed the manuscript.

Table of Contents

List of Tables

List of Figures

List of Symbols

Symbols	Unit	Definition
r	m	The distance between the transducer and a target
θ	°	The off-axis angle or the polar angle in spherical coordinates
φ	°	The azimuth angle in spherical coordinates
x_c	m	The distance along the x axis in Cartesian coordinates
y_c	m	The distance along the y axis in Cartesian coordinates
a	m	Transducer radius
k	m	Wave number
c_w	m/s	Sound speed in the water
f	Hz	Frequency
ω	Hz	The angular frequency
f_c	Hz	Centre frequency
Δf	Hz	Frequency bandwidth
α	°	The angle coordinate along the major axis plane
β	°	The angle coordinate along the minor axis plane
α_{-3dB}	°	The angle from the transducer beam axis to the point of half power in α plane
β_{-3dB}	°	The angle from the transducer beam axis to the point of half power in β plane
α_0	°	Offset angle along α plane
β_0	°	Offset angle along β plane

$B(f,\theta)$	dimensionless	One-way beam pattern or the directivity at a point to the maximum value
J_1	dimensionless	The first order cylindrical Bessel function
$B_{model}(f,\theta)$	dimensionless	Modelled one-way beam pattern for a transducer
$B_{meas}(f,\theta)$	dimensionless	Measured one-way beam pattern for a transducer
$H(f)$	dimensionless	System response function
$H(f,0)$	dimensionless	System response function at the acoustic centre ($\theta = 0$)
$H(f,\theta)$	dimensionless	System response function angle at off-axis angle θ
$V_R(f)$	V	Received voltage at the receiver in the frequency domain
$V_T(f)$	V	Transmitted voltage in the frequency domain
$L_{TL}(f)$	V	The two-way transmission loss function
$CP_T(f)$	dimensionless	The autocorrelation of the transmit signal with a replica of the transmit signal
$CP_R(f)$	dimensionless	The cross correlation of the transmit signal with a replica of the transmit signal
$F_{bs}(f)$	m	Backscattering amplitude
$F_{bs,cal}(f)$	m	Modelled backscattering amplitude of a calibration sphere
$TS(f)$	dB *re* 1m^2	Compensated target strength of an object at with reference to the beam axis ($\theta = 0$)
$TS_{model}(f)$	dB *re* 1m^2	Modelled target strength of an object at beam axis ($\theta = 0$)
$TS_{meas}(f,\theta)$	dB *re* 1m^2	Measured uncompensated target strength of an object at off-axis angle θ
$\Delta TS(f)$	dB *re* 1m^2	Residual target strength or the difference between the compensated measured and modelled target strength
$S_v(f)$	m	The sum of the backscattering cross section per unit of water volume
ψ	dB	Equivalent two-way beam angle
ϕ	°	The phase difference between signals arriving at a pair of transducer segments

d	m	Segment distance or the separation between the centres of two halves
Λ	dimensionless	The angular sensitivity or the ratio of the phase angle to the geometric angle
x	dimensionless	x = kasinθ
$\overline{\sigma_i}$		The standard deviation of signals averaged for frequency
ξ	dimensionless	The geometrical parameter or the ratio of the transducer radius to the segment distance
ξ_{e1}	dimensionless	Frequency independent geometrical parameter
$\xi_{e2}(f)$	dimensionless	Frequency dependent geometrical parameter
ξ_0	dimensionless	Frequency independent offset in the geometrical parameter
ξ_1	dimensionless	Coefficient of the geometrical parameter varying linearly with the frequency
$B(f,\theta,\xi)$	dimensionless	One-way beam pattern parameterised to ξ
$\varphi_{bs}(f)$	°	The frequency spectrum of the absolute phase
$DP(f)$	°/Hz	The frequency response of the differential phase
$RP(f)$	°	The frequency response of the residual phase
$A(f,\theta)$	V	Amplitude part of the system response function
σ_{bs}	M^2	Backscattering cross section
τ	s	The signal pulse duration
a	m	The equivalent radius of a gas-filled sphere
δ		Damping constant
f_0	Hz	Resonant frequency
Q	dimensionless	Quality factor
α_w	dimensionless	The absorption coefficient of water

γ	dimensionless	The ratio of the specific heat of the body and the outer fluid
P_0	Pa	The pressure at the surface
ρ	kg/m^3	The density of a target
x_p, y_p, z_p	m	The PLAOS coordinate system
x_a, y_a, z_a	m	The echosounder coordinate system
x_o, y_o, z_o	m	The camera coordinate system
u, v	m	The photograph coordinate system
f_{oa}	m^{-1}	The focal length of the camera in air
f_{ow}	m^{-1}	The focal length of the camera in water
n_w	dimensionless	The refractive index of water
h	mm	The horizontal sensor size of the camera
w	mm	The vertical sensor size of the camera
h_{res}	dimensionless	The horizontal resolution in pixels
w_{res}	dimensionless	The vertical resolution in pixels
$[R_{az} R_{ay} R_{ax}]$	dimensionless	The rotational matrix along x, y and z directions in the echosounder coordinate system
$\begin{bmatrix} T_{xa} \\ T_{ya} \\ T_{za} \end{bmatrix}$	dimensionless	The translation vector along x, y and z directions in the echosounder coordinate system
$[R_{oz} R_{oy} R_{ox}]$	dimensionless	The rotational matrix along x, y and z directions in the camera coordinate system
$\begin{bmatrix} T_{xo} \\ T_{yo} \\ T_{zo} \end{bmatrix}$	dimensionless	The translation vector along x, y and z directions in the camera coordinate system

List of Acronyms

Acronym	Definition
PC	Pulse compression
LFM	Linear Frequency Modulated
FM	Frequency Modulated
CW	Continous Wave
GABRP	Great Australian Bight Research Program
PLAOS	The Profiling Langrangian Acoustic Optical System
ICP	Instrumented Corer Platform
MNF	Marine National Facility
GDP	Geometrical and Directional Parameters
GP	Geometrical Parameter
SNR	Signal to Noise Ratio
SARDI	The South Australian Research and Development Institute
RMSE	Root Mean Residual Error
LTI	Linear Time-Invariant

Chapter 1

General Introduction

Echosounders are instruments used to detect and locate echoes based on the principle of acoustic scattering. A basic echosounder comprises a transmitter, which feeds electric signals at a given frequency to a transducer that converts it to short bursts of sound, also known as pings. The acoustic waveforms propagate through the surrounding medium (water in this case) and undergo scattering from the objects present in the water. The backscattered echoes propagate to the receiver where they are converted back to electrical signals. They are then amplified by the receiver to compensate for the transmission loss and subsequently filtered, decimated and stored. The signals are then analysed to retrieve information about the scatterers such as location, size, material and even orientation.

Since the late 1960s echosounders have been used as a non-invasive synoptic tool to remotely study the marine organisms (Barham, 1966; Batzler, & Barham, 1963; Fernandes et al., 2002). Acoustic scattering is a complex phenomenon strongly dependent on the scatterer's physical and material properties, including its orientation and even behaviour (Foote, 1980; Martin Traykovski et al., 1998; McClatchie, Alsop, Ye, et al., 1996; Ona, 1990b; Simmonds, & MacLennan, 2005; Warren et al., 2002). Accurate interpretation of the backscattered echoes remains a challenge for the marine acousticians, especially in an open ocean environment with several biological and non-biological acoustic sources. Conventionally single-frequency narrowband echosounders were used for biomass and abundance estimate for fishes (Ehrenberg, 1974; Foote et al., 1986). However, the interpretation of backscattered energy for characterisation remained ambiguous due to the variability in the material properties, size and shape of the organisms being studied (MacLennan, 1990).

The use of multiple frequency echosounders improved the scenario by providing additional frequencies for quantifying the scatterer size and distribution from the backscattered echo (Holliday et al., 1989; Kloser et al., 2002; Pieper et al., 1990). They were successful in classifying in case of significantly different organisms (such as a fish and fluid-filled organisms or benthic and planktonic shelled organisms) (Martin et al., 1996; Stanton et al., 1996; Stanton et al., 2000).

The application of multi-frequency echosounder for species classification was limited by the number of discrete single frequencies available to map the acoustic spectrum of single targets. In such a situation, the availability of a continuous wide frequency range would enable visualisation of the spectral response of the acoustic energy. Further, the variation of the backscattered acoustic energy with frequency could be directly linked to a single target's characteristics, thus helping in their detection and classification. This is achieved through what is known as a broadband echosounder, which forms the subject of this thesis.

Theoretically, a broadband acoustic signal refers to one with high energy distributed across a wide band of frequency. For the echosounder to be able to resolve two nearby targets, they must be separated by at the least spatial resolution (Simmonds, & MacLennan, 2005). This could be attained by emitting pulses of shorter duration, which would require high signal amplitude and hence high instantaneous power. This would require strong convertors or high power, which can be costly and at the same time be unsafe to use. An alternative option is to use a broadband echosounder which increases the frequency bandwidth by modulating the frequency of the waveforms, to produce a swept frequency burst, also known as 'chirp'.

A broadband echosounder comes with the advantage of wide frequency bandwidth, higher spatial resolution and even higher signal to noise ratio. To utilise the broadband echo-sounding technology to its full potential, it is important that efforts are focused on the development of new signal processing techniques, use of new acoustic identifiers and resolving practical challenges in the implementation.

1.1 Remote sensing marine organisms (Micronekton)

The mesopelagic region (~200 to 1000 m) of the Great Australian Bight (Figure 2.7) and the Southern Ocean support a diverse range of micronekton (Figure 1.1 and Figure 1.2) (fishes, crustaceans, copepods, krill, squids) (Koslow et al., 1997; Williams, & Koslow,

1997; Young et al., 1996). Often perceived as economically and socially less significant, these ubiquitous animals form a critical constituent of the marine ecosystem. They are a crucial part of the food web dynamics playing an important role in the population distribution of the top-level pelagic predators (such as Juvenile southern bluefin tuna, turtles, fur seal and marine mammals) (Ward et al., 2008). Distributions of these animals are inherently complex, inconsistent and continuously variable under the influence of physical oceanographic processes (Béhagle et al., 2016; Sinclair, & Stabeno, 2002). Understanding the distribution pattern, biomass and the critical ecological process of this enigmatic community can provide a better understanding for future sustainable management of this resource. However, the dynamics of this community remains poorly understood due to a lack of appropriate sensors, unpredictable environmental conditions and selectivity of different sampling methods (acoustic, optics and nets).

Figure 1.1: A selection of samples from net catches collected from the mesopelagic depth of the Great Australian Bight region. (Photographs provided by Rudy Kloser).

Figure 1.2: A mix of mesopelagic and shallow water fish species (top) and crustacean (below) collected from the mesopelagic region. (Photo provided by *RV Investigator*).

The acoustic scattering method plays an important role in remote sensing and estimating the abundance and distribution of these organisms (Benoit-Bird, & Au, 2001; Kloser et al., 2002; Koslow et al., 1997; McClatchie, & Dunford, 2003). The unique ability of a broadband echosounder to preserve the spectral information of acoustic targets across a wide frequency bandwidth has opened new opportunities in the remote detection and characterisation of the micronekton community. Combining the broadband acoustic sensing technology with advanced operational platforms allows measuring the frequency

dependence of scattering from organisms to highest spatial resolution thereby assisting in species identification and classification (Dalen et al., 2003; Godø et al., 2014; Kloser, 1996; Verma et al., 2017).

1.2 Motivation

It is hypothesised that the commercial availability of broadband echosounders (for example, the Simrad EK80) could lead to a paradigm shift in the acoustic surveying technique. The need for unbiased information for identification and classification of marine organisms is driving research in the broadband acoustic method. Many new algorithms and practices are being applied to assist in the implementation of this new technology (Briseño-Avena et al., 2015; Islas-Cital et al., 2011a; Lavery et al., 2010; Stanton, & Chu, 2008). It is important to develop systematic processing and analysis techniques to provide a precise estimation of the scatter properties and reduce uncertainties. This requires the accurate calibration of the echosounder, characterisation of the transducer's parameters, use of additional acoustic identifiers and sufficient verification of the sampled organisms.

1.3 Aim of the thesis

The specific goals of the thesis were:

1. To develop an alternative technique to calibrate a broadband echosounder for measuring target strength as a function of frequency.

2. To determine the effective beamwidth of a transducer by using a measurement-model approach.

3. To develop appropriate indices to visualise the target induced phase distortion in the backscattered echo.

4. Calibrate the echosounder for phase measurement and use it to extract the frequency response of the target phase.

5. Demonstrate the application of the technique through the derivation of the in situ target strength of different organisms from the Great Australian Bight region.

6. Derive the frequency response of in situ target strength and phase for example targets of different species of micronekton from the Southern Ocean region.

7. Develop a technique to verify the presence of acoustic targets on the concurrent still image.

8. Demonstrate the reliability of target phase measurement by inverting the target strength and phase measured for an optically verified target.

1.4 Thesis outline

This is a hybrid thesis where each work is presented as an independent chapter with a separate introduction, method and discussion section. Research method and analyses relevant to each chapter are described to detail within the chapters. Efforts have been made to reduce the overlap between the introduction and method of each chapter.

Chapter 2 provides an overview of the different terminologies, methodologies, acoustic variables and processes of a broadband echosounder relevant to the research. The experiments and surveys undertaken as a part of the research are also briefly described.

In Chapter 3, a technique to extract the frequency response of the target strength using the transducer system response is presented. The technique was applied to calibrate a broadband echosounder to determine the on-axis sensitivity and achieve directivity compensation for off-axis angles. The feasibility of the technique is established through a set of acoustic backscattered signals from two standard sphere targets at two amplitude ramp settings.

In Chapter 4, the system response function is used to derive the effective geometrical and directional parameters of a split beam broadband transducer. An inversion approach was used to test the frequency dependency of the parameters. The hypothesis of the effective radius of a broadband transducer being constant across the frequency band was also tested.

Chapter 5 investigates the target induced phase distortion in the backscattered signal as a potential classifier; an algorithm is developed to derive the frequency response of the target phase. The concept is based on the use of both the system response and backscattered echoes in complex form. Three variables are used to visualise the signal phase, absolute, differential and residual phase. The developed technique was applied to calibrate the broadband echosounder for phase measurement for the two types of transmitting signals at all positions.

Chapter 6 is the preliminary application of the technique developed in Chapter 3 to derive the in situ target strength from the mesopelagic region of the Great Australian Bight. As examples, the frequency spectra of the target strength of two single targets are shown. The measured spectra are compared to the output of numerical acoustic scattering models. Some of the mathematical notations used in the chapter are different from other chapters as it was published in the first year of research (Verma et al., 2017).

Chapter 7 reports a combined acoustic-optics survey that was carried out in the mesopelagic region of the Southern Ocean. A technique is developed to visualise a single acoustic target on an echogram and on the concurrent still image. By using this transformation technique, the presence of several single targets such as squids, mesopelagic fishes and bubble-like targets on the echogram were confirmed. The frequency response of the target strength and residual phase of several targets were obtained. A numerical acoustic scattering model for a gas-filled sphere is developed to predict both the phase and target strength. The target strength and residual phase measurements of three resonant targets found at the different depths were fitted to the output of the models. This shows the ability of the phase to be used as an acoustic classifier.

Chapter 8 concludes the thesis with a general discussion of the significant findings, limitations, and recommendations for future research.

Chapter 2

Research Background

In this chapter, a brief introduction to the aspects of the broadband echosounder relevant to the thesis is given. For in-depth technical information of the acoustic scattering techniques, readers are referred to Medwin, and Clay (1998) and Simmonds, and MacLennan (2005) for implementation in fisheries. For technically comprehensive coverage of broadband methods in fisheries science, readers are referred to Demer et al. (2017).

2.1 Broadband echosounder

A broadband echosounder (such as Simrad EK80) transmits frequency-modulated waveforms instead of single-frequency waves like a conventional narrowband echosounder. This allows the target's scattering characteristics to be measured as a function of frequency. The backscattered echoes from consecutive pings are pulse compressed in time. The time-compressed pings are stacked to generate a two-dimensional range and time graph referred to as pulse-compressed echogram (Figure 2.1).

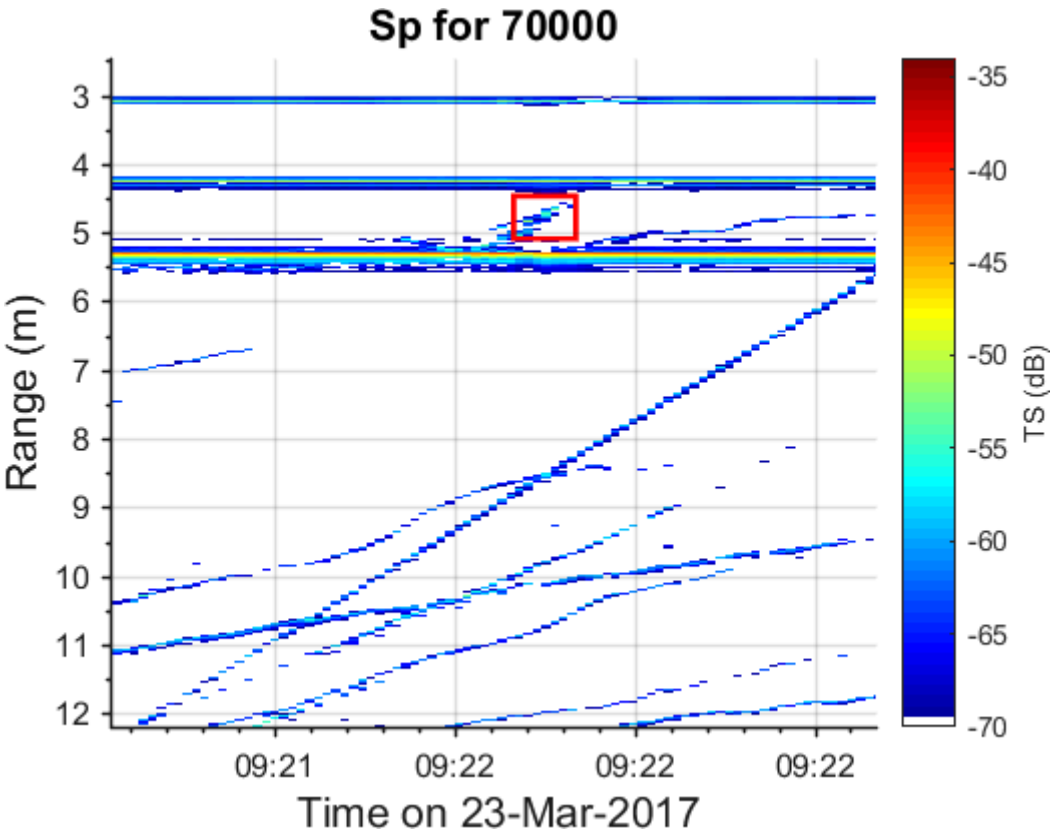

Figure 2.1: An example of pulse compressed echogram illustrating a single target enclosed in the red box.

2.1.1 Signal processing terminologies

2.1.1.1 Frequency modulated waveforms

A narrowband echosounder transmits a sound pulse or ping. This ping consists of several cycles at a constant frequency and amplitude. The frequency spread of this signal is narrow with most energy concentrated at the operating frequency. A broadband echosounder transmits a chirp or linear frequency modulated (LFM) signal. In an LFM

signal, the instantaneous frequency varies linearly with the time (Ehrenberg, & Torkelson, 2000). The wave has a broader continuous frequency bandwidth, Δf (Hz) spread on both sides of the centre frequency, f_c (Hz) covering a continuous range of frequency. The simulation of the narrowband and LFM waves in the time domain and their power spectra are shown in Figure 2.2.

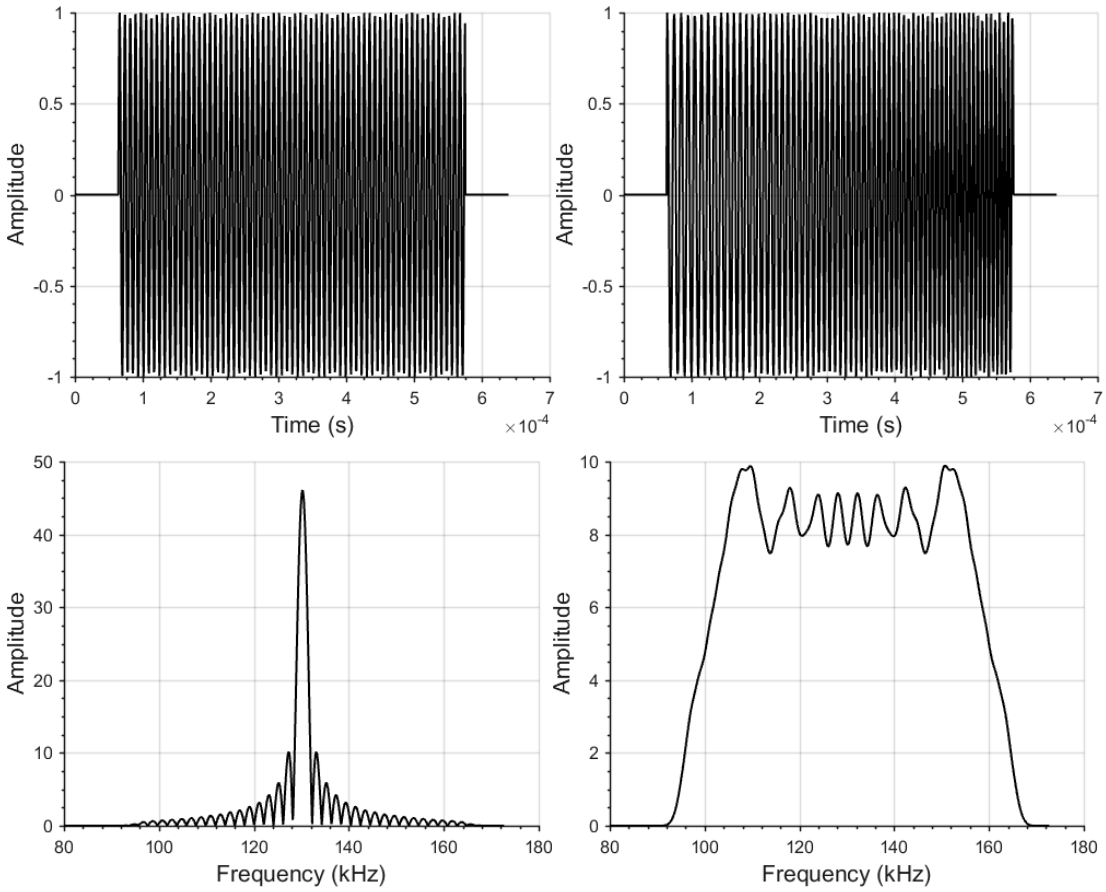

Figure 2.2: Simulated single frequency narrowband (left) and linear frequency modulated transmit pulses (right) in the time domain (top) and their power spectra in the frequency domain (bottom). The frequency of the narrowband wave is 127 kHz, and the frequency range of the LFM wave is from 95 kHz to 160 kHz.

The power spectrum in the frequency domain is the Fourier transform of the time-domain autocorrelation function.

2.1.1.2 Pulse compression

Pulse compression (PC) (Chu, & Stanton, 1998; Turin, 1960) is a post-processing technique applied to increase the spatial resolution and the signal to noise ratio even at low transmit power. This is obtained by correlating the received signal with an appropriate match filter; which is a replica of the frequency-modulated transmitted pulse

in this case. Pulse compression can be achieved either in the time domain by cross-correlating the received signal with a replica of the transmit burst, or in the frequency domain by multiplying the Fourier transform of the received signal by the complex conjugate of the Fourier transform of the transmit signal and then inverse Fourier transforming the result. Unlike a narrowband signal, the range resolution of a pulse compressed signal is not dependent on the time duration but is inversely proportional to the frequency bandwidth (Burdic, 1991). Figure 2.3 shows an echo backscattered from a target before and after pulse compression.

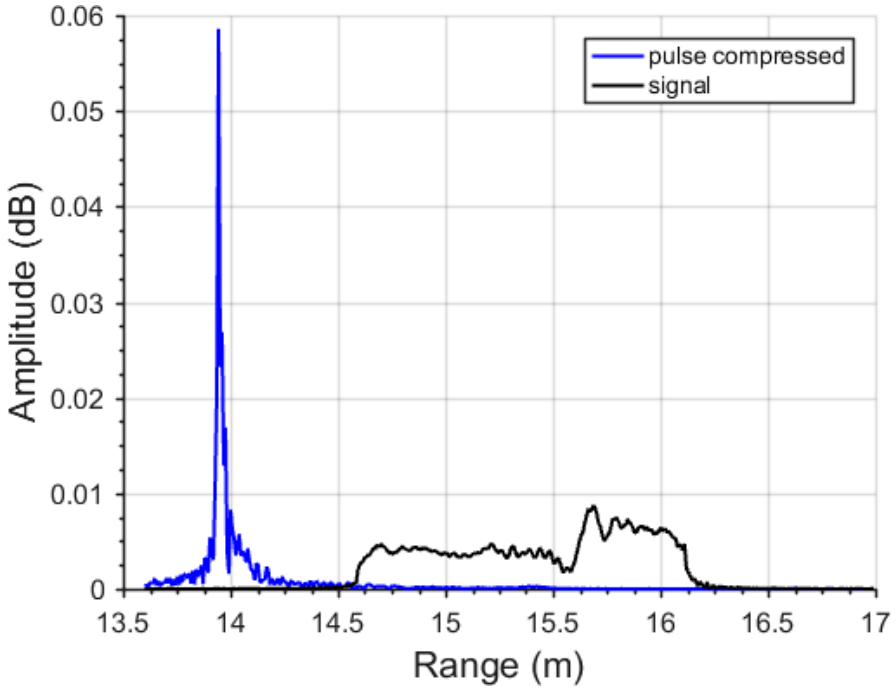

Figure 2.3: A signal backscattered from a sphere target before (black line) and after (blue line) pulse compression plotted with the range. The target here is a tungsten carbide (6% cobalt binder) sphere of diameter 38.1 mm at range 15 m. The frequency bandwidth of the echosounder is 95 kHz to 160 kHz, and the pulse length of 0.512 ms.

On the downside, a compressed pulse contains responses at other times and ranges known as side lobes. The side lobes can interfere with the signal analysis. One of the methods to limit the side lobe is by windowing or gating the received signal (Stanton, & Chu, 2008). The choice of window length and window type could affect the frequency spectrum.

2.1.1.3 Beamwidth and beam pattern

When an acoustic waveform is transmitted, the amplitude of the signal is maximum (usually at the centre on-axis) and decreases sideways off-axis. The beamwidth, θ_{-3dB}

(°) is defined as the angular separation between opposite points off-axis at which the transmit signal amplitude is 3 dB lower than at the on-axis centre of the beam (Urick, 1983). As a result of the acoustic reciprocity principle (Urick, 1983), the receive sensitivity will also be 3 dB lower at these points than at the beam centre, so backscattered signals from a target will appear 6 dB lower than from the same target at the beam centre. θ_{-3dB} of a transducer is proportional to the ratio of the acoustic wavelength to the transducer diameter. So the θ_{-3dB} of a broadband echosounder varies with frequency. For lower frequencies, the energy is spread over a larger area compared to the high-frequency component, where it is concentrated. The beam pattern, $B(f,\theta)$ is the ratio of the transmitted acoustic intensity at an angle and frequency to its maximum value at the same frequency. An example of the beam pattern of a broadband circular transducer (Simrad ES70-18CD) at three different frequencies of 55 kHz, 70 kHz and 90 kHz is shown in Figure 2.4. The beamwidth at the nominal central frequency 70 kHz is 18°.

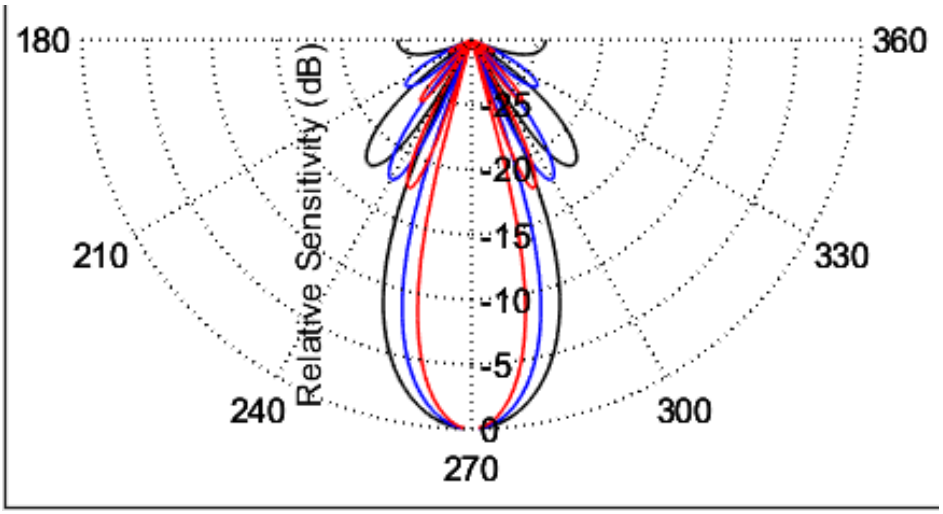

Figure 2.4: The beam pattern of a broadband circular transducer (Simrad ES70-18CD) at three different frequencies 55 kHz (black), 70 kHz (blue) and 90 kHz (red). The beamwidth at the nominal central frequency 70 kHz is 18°.

2.1.1.4 Target strength estimate

In the far-field, the backscattered energy received from a signal target by the transceiver can be characterised as the target strength, TS (dB *re* 1m^2). Established as an index in fisheries acoustics (Midttun, 1984), TS is the logarithmic expression of the backscattering amplitude (Medwin, & Clay, 1998). As elaborated in Foote (1991c) TS of single targets (fish, zooplankton or micronekton) can be estimated in either (1) in-situ or (2) ex-situ environment.

In ex-situ methods, organisms are removed from their natural environment and retained in a controlled condition (tethered (Midttun, 1984; Nakken, & Olsen, 1977) or caged (Foote et al., 1986)). While ex-situ measurements have generated valid results comparable to outputs of numerical models (Foote, 1983), the effects of confinement on the functioning and physiological condition of the organism remain mostly undetermined.

In-situ TS measurements are undertaken in the natural environment of the organisms and include direct and indirect methods. Direct in-situ measurements require single resolved targets. The common practice was the use of dual-beam (Ehrenberg, 1974) or split-beam echosounder (Ehrenberg, & Torkelson, 1996; Foote et al., 1986). Since its development in the early 1980s, several researchers have used the split beam method for determination of the TS (Bodholt, & Solli, 1992; Didrikas, & Hansson, 2004). Usually, single or a combination of split-beam echosounder (multi-frequency) are used to measure the target strength. Use of multi-frequency echosounders provides a spectrum of discrete frequencies to map the TS (Conti et al., 2005; Holliday et al., 1989). Combining echosounder with a camera can improve accuracy, as it can verify the target position and the ensonified species. Several types of research have reported the use of single and stereo vision cameras with the echosounders (Han et al., 2010; Kloser et al., 2016; Lundgren, & Nielsen, 2008; Sawada et al., 2009; Takahashi et al., 2004).

$TS(f)$ measurements are dependent on the organism's orientation (Lee et al., 2012; McGehee et al., 1998; Warren et al., 2002), anatomical and morphological structure (McCartney, & Stubbs, 1971; McClatchie, Alsop, & Coombs, 1996), material properties (Chu et al., 1993) and their physiological condition (Ona, 1990b). Invasive and non-invasive techniques are used to determine these properties. Recent years have seen an increase in the use of advanced methods such as soft x-rays (Sawada et al., 1999), and MRI scans (Peña, & Foote, 2008) to determine the physical and morphological properties up to mm resolution.

Since the 2000s, there has been an increase in the use of broadband (single beam and split beam) echosounders for remote sensing. The wide frequency bandwidth enables the extraction of the frequency spectrum of the $TS(f)$ (Bassett et al., 2017; Demer, & Conti, 2003; Verma et al., 2017). Also, the signal pulse compression increases the ability to resolve single targets (Chu, & Stanton, 1998), and the high signal to noise ratio allows enhanced detection of backscattered echoes from a single target. It is thus hypothesised that the broadband echosounder would enhance the capability of acoustic techniques to

obtain in-situ single target $TS(f)$ measurements for classification of marine organisms. Undertaking reliable $TS(f)$ in –situ measurement with broadband echosounder relies on the calibration and characterisation of the instrument, and accurate beam pattern compensation.

2.1.1.5 Equivalent angle

The equivalent beam angle ψ, (sr) is defined as the solid angle at the apex of the conical beam that produces the same energy as that of the actual transducer (Urick, 1983). The equivalent angle is used to derive the density of scatterers and estimate biomass estimating the fish density, biomass and abundance estimates and hence requires accurate measurement made after mounting the transducer. It is not required for estimates of target strength of individual targets.

2.1.2 Research challenges

Broadband echo sounding technology is being integrated into ecosystem acoustics for their identification, classification and detection of marine organisms. Many research studies imply that broadband echosounders could serve as an improved non-invasive remote sensing tool as compared to narrowband echosounders. The last two decades have witnessed several research studies directed to develop signal processing methodologies, calibration procedures and conduct in-situ surveys with the new tool.

Some of the research areas and challenges are:

1. Phase as an acoustic identifier.
2. Calibration for phase and amplitude measurements.
3. Characterisation of transducer
4. Inclusion of phase in numerical acoustic scattering models

2.1.2.1 Phase as an acoustic identifier

Target-induced phase distortion in the backscattered signal contains further clues to a target's morphological and material characteristics, which can prove beneficial in remote acoustic identification. However, conventional acoustic analyses are typically limited to the use of the magnitude of the backscattered signal, ignoring the phase part (Medwin, & Clay, 1998).

It is speculated that using the target phase as an additional acoustic descriptor may assist in the characterisation of acoustically detectable marine organisms (Atkins et al., 2007; Barr, & Coombs, 2005; Braithwaite, 1973). However, limited literature has been published on the application of phase for detection and identification of marine biota. Phase suffers from uncertainties owning to the range accumulation effect, low signal to noise ratio, and frequency resolution which hinders obtaining appropriate quantitative estimates. Several methods have been developed to reduce the sources of ambiguities such as the phase gradient or rate of change of phase (Barr, & Coombs, 2005; Yen et al., 1990), gross phase shifts (Bolus et al., 1982) and phase differences (Yen et al., 1990). These methods have limitations owning to their usage and derivation. For reliable interpretation, it is important that suitable techniques are established to visualise the frequency-dependent phase.

2.1.2.2 Calibration for phase and amplitude measurements

Calibration of an instrument is essential for performing quantitative analysis. The standard target calibration experiment has been proposed to calibrate a broadband echosounder (Demer et al., 2015). The method involves using a standard sphere target of a known response and comparing the frequency response of the on-axis sensitivity with the theoretical response (Foote, & MacLennan, 1984). Calibration of broadband echosounders draws considerable research interest due to its inherent complexities such as the frequency dependence of transducer beam patterns and environmental parameters (Lavery et al., 2010), resonance effects of calibration spheres (Stanton, & Chu, 2008), and anomalies in the phase angles (Islas-Cital et al., 2011a).

For an in situ application, a system must be calibrated during the survey to account for the surrounding environmental variables (Demer, & Renfree, 2008) and even any changes in the instrument's sensitivity (Jech, Chu, et al., 2003). Also, the changes in the transducers mounts from the laboratory setup to open ocean can increase the risk of beam pattern deviation and hence, the system's response (Simmonds, 1984). A broadband echosounder requires a calibration technique developed specifically to cover the entire frequency bandwidth and account for the frequency dependence of the transducer's beam pattern.

The constructive and destructive interference of the scattered signals from the different interfaces of the calibration spheres leads to sharp fluctuations at specific frequencies, which introduces uncertainties in calibration at these frequency regions (MacLennan,

1981). While a pragmatic approach of partial wave analysis can resolve the frequency dependence (Stanton, & Chu, 2008), a logistically complicated but robust approach using multiple calibration spheres (Foote, 2000; Foote, 2007a; Lavery et al., 2017) of different sizes are also useful to mitigate resonance effects.

Successful real-world implementation of the target phase requires that broadband echosounders are calibrated for phase measurements (Barr, & Coombs, 2005). Islas-Cital et al. (2011a) conducted calibration with broadband sonar. These experiments on custom made sonar system generated good agreement between the theoretical and experimental phase values. Given the commercial availability of Simrad EK80 echosounder, a method similar to that used for amplitude calibration, that accounts for the transducer directivity and effect of amplitude ramping would prove beneficial for scientific studies.

2.1.2.3 Characterisation of transducer

A split-beam broadband transducer is an arrangement of several individual piezo-ceramic elements (Wilson, 1988) to obtain a desired acoustic field and directivity across the frequency range. It is commonly made up of four quadrants that are simultaneously used for transmission (Ehrenberg, 1983; Stansfield, & Elliott, 2017). This allows finding the target positions by measuring the phase difference between the signals received by opposite quadrants. Most of the transducers come with a set of nominal geometrical (transducer radius) and directional parameters (beamwidth and beam pattern) provided by the manufactures (Bodholt, 2002).

Numerous factors may contribute to a modification in the transducer functioning from the nominal value. Internal factors such as the instrument sensitivity (Islas-Cital et al., 2010), design and electronics (Jech, Foote, et al., 2003), ageing, and hardware malfunctioning (Knudsen, 2009) may modify the transducer performance. External factors such as the mounting arrangement (Knudsen, 2009), nonlinear sound propagation (Tichy et al., 2003) and environmental parameters (temperature, salinity, pressure and depth) (Dalen, & Bodholt, 1991; Demer, & Renfree, 2008; Kloser, 1996) are known to interfere with the transducer output. Independent evaluation of the transducer parameters is needed to obtain accurate verifiable information.

Several studies have measured the effective beamwidth (Degnbol, 1988) and consequently, the equivalent angles (Reynisson, 1998; Simmonds, 1984) for narrowband echosounders at a single frequency. The wide frequency bandwidth of a

broadband echosounder complicates the process, and consequently, the possibility of the parameters having a frequency dependence needs to be assessed. Moreover, it is usually hypothesised that in spite of several elements, the transducer behaves like a circular piston of constant radius. Therefore, it is essential that a characterisation technique is formulated that can derive the effective parameters, verify the fixed transducer radius and probe the frequency dependence of the parameters.

2.1.2.4 Inclusion of phase in numerical acoustic scattering models

Prediction of acoustic backscattering from marine organisms using numerical models backscatter has been in practice in fisheries acoustic research since the late 1950s (Anderson, 1950). Measurements are matched to the backscattering prediction made by approximating the organism as a simple geometric structure such as a sphere (Anderson, 1950; Love, 1978b), cylinder (Stanton, 1989; Stanton et al., 1993) or a prolate spheroid (Furusawa, 1988; Ye, & Hoskinson, 1998) with single or variable material properties. However, numerical acoustic scattering models report the scattering amplitude only (Jech et al., 2015; Stanton et al., 1996).

To establish the target phase as a reliable acoustic index it is important that measurements from live organisms are matched to the predicted output of the appropriate numerical acoustic scattering model. It would be worthwhile to include the phase into these mathematical scattering models and compare the obtained phase spectrum with the model output.

2.2 Experiments and surveys

Three sets of data were used for the thesis. The measurement procedures are outlined in detail in each chapter. The following section provides a brief outline

2.2.1 The calibration experiment

The first set comprises of data collected from a series of experiments conducted from 5th to 13th August 2015 in the estuary of Derwent River in Hobart (Figure 2.5). A scientific broadband echosounder, Simrad EK80, with split-beam transducer (ES120 (WBT 536012), was calibrated across the frequency range 95 – 160 kHz. Two standard target spheres were used, and backscattered echoes recorded with different settings and configurations such as pulse length, range and ramping. Chapter 3, Chapter 4 and Chapter 5 are based on the data collected during this experiment.

Figure 2.5: An illustration of the experiment set up.

2.2.2 The Great Australian Bight region

A multidisciplinary scientific survey was conducted in the Great Australian Bight region on board the *RV Investigator* from 30th November to 22nd December 2015. The voyage was part of the Great Australian Bight Research Program whose overarching goal was to understand the environmental, economic and social structure of the region (GABRP, 2013). The Instrumented Corer Platform (ICP), a custom-designed depth-profiling platform (Figure 2.6) was configured with two broadband echosounders (Simrad EK80) and ancillary sensors (cameras, pressure sensors and CTD) (Sherlock et al., 2014). The whole set up was deployed to depths of 600 – 1000 m at several locations (Figure 2.7).

Figure 2.6: The Instrumented Corer Platform (ICP) ready to be deployed.

High-frequency broadband acoustic recordings were collected from deep mesopelagic habitat to characterise the organisms distributed in the region. The CTD and other ancillary sensors provided the physical environment data such as conductivity, temperature, density, roll and pitch along the depth track. These datasets form the basis for chapter 6. Additional depth stratified net samples were collected from nearby locations using a MID water Opening and Closing (MIDOC) net (Kloser et al., 2011); and optical images of the water column were obtained using optical sensors mounted on the AOS probe. The catch provided a glimpse of the mesopelagic habitat. However, these were not coincident with the acoustic data collection.

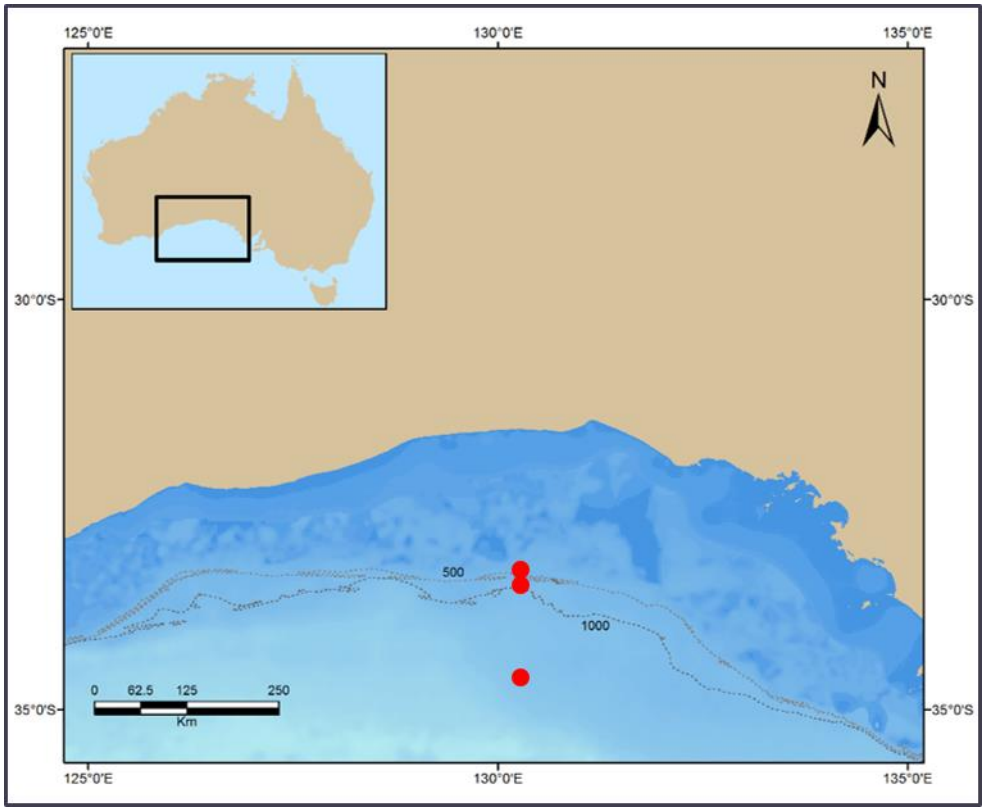

Figure 2.7: A map of the Great Australian Bight region with the red points indicating the locations of data collection.

2.2.3 The Southern Ocean region

Opportunistic acoustic-optics samples were collected as a part of the IMOS field survey within transects of the Southern Ocean. Acoustic-optics samples were recorded from the mesopelagic depth using a depth-profiling platform. The Profiling Langrangian Acoustic Optical System (PLAOS) is a custom-designed platform developed by CSIRO based on previous research (Kloser et al., 2016; Marouchos et al., 2016). The framework consists of a cylindrical steel frame with a rotatable plate at the bottom housing the optical sensors, acoustics transducers, pre-amplifiers, transmitters, CTD and a monitoring frame (Figure 2.8).

Figure 2.8: A Profiling Langrangian Acoustic Optical System ready to be deployed.

PLAOS was configured with two broadband split-beam transducers, one digital video, and two single-lens cameras to provide synchronised still images, video and acoustic recordings from the water column. Ancillary sensors were attached to sense the motion of the whole system and surrounding environmental conditions. Chapter 7 is based on the dataset recorded from this survey.

Chapter 3

Calibration and Compensation of Off-axis Measurements of a Broadband Echosounder using the System Response

A technique is developed for the absolute calibration and directivity compensation of broadband echosounders. The method is based on the use of the frequency response of the system's combined transmit/receive function (the system response) at the on-axis and off-axis positions within the acoustic beam. The technique is applied to calibrate a Simrad EK80 scientific broadband echosounder over a frequency range of 95 kHz to 160 kHz. The performance of the method was studied for both "fast" and "slow" ramp transmit pulses. The experimental investigation supported the calibration and compensation theory. The results were compared to the directivity compensation achieved with the modified Bessel function for the same set of data. The method is explicitly developed to cover the wide bandwidth of a broadband echosounder and does not require estimation of the variation of the transducer's effective beamwidth with frequency.

3.1 Introduction

There has been an increase in the use of broadband echosounders for discrimination (Bassett et al., 2017), classification and characterisation (Jech et al., 2017; Lavery et al., 2007; Lee, & Stanton, 2015; Reeder et al., 2004) of marine organisms. Obtaining accurate acoustic quantitative estimates for input to the prediction of marine ecosystem dynamics (Handegard et al., 2013) and sustainable management of resources (Pikitch et al., 2004) requires accurate calibration of the echosounder. In a dynamic environment, it is important that the calibration accounts for the effects of mounting (Simmonds, 1984), ship motion, environment (Brierley et al., 1998; Demer, & Renfree, 2008) and the instrument sensitivity (Jech, Foote, et al., 2003). A broadband echosounder transmits frequency modulated (FM) waveforms or 'chirp' signals. The FM waveforms can measure the scattering response as a function of frequency from which potentially useful information can be extracted (Holliday, 1972; Stanton, & Chu, 2008; Zakharia et al., 1996). However, calibration of the instrument across the broad bandwidth is complicated by the frequency dependence of the beam pattern (Lavery et al., 2010) and sensitivity to resonance induced peaks and nulls in the backscattered amplitude (Stanton, & Chu, 2008). Thus, a calibration technique specifically developed to cover a wide frequency range is required.

Calibration of a split-beam transducer should account for, the on-axis sensitivity and the directivity compensation for measurements with targets situated away from the beam axis (Demer et al., 2015; MacLennan, & Svellingen, 1986). Usually, the standard calibration method used for the narrowband echosounders is extended to cover the broadband range with careful consideration of the sources of uncertainties (Demer et al., 2015). The on-axis level is derived by comparing the measured and the theoretically modelled response of a standard target aligned at the centre of the acoustic beam (Foote et al., 1987; MacLennan, 1981). For broad bandwidth single and split-beam transducers (Lavery et al., 2017), several approaches have been used to find the on-axis sensitivity, using a single sphere (Stanton, & Chu, 2008) or multiple spheres (Foote, 2007b) in the near field (Chu, & Eastland, 2015) or the far-field (Islas-Cital et al., 2011a).

For a constant-radius broadband transducer, the beam pattern is a function of the frequency. As a result, the higher frequency components of the FM pulse have a narrower angle range than the lower frequency components. The backscattered signals from the off-axis target require appropriate correction for the effect of the transducer

directivity, which is usually achieved with mathematical beam pattern models (Urick, 1983). The beamwidth, θ_{-3dB} (°) at a particular frequency is determined by moving a standard target in all directions and recording the backscattered amplitude (Ona, 1990a). The point with the maximum backscattered amplitude is the on-axis. The responses from different positions are fitted with a best-fit polynomial. The angle between -3dB points on two orthogonal directions through the on-axis quantifies θ_{-3dB}(Simmonds, 1984). This technique provides the beamwidth only at a single frequency that is sufficient for a narrowband system. A broadband system will require the beamwidth to be estimated for each frequency component, which is logistically arduous if carried out one frequency at a time. An alternative would be to use a technique for directivity compensation, which is independent of explicit knowledge of the beamwidth.

For an electroacoustic system, the transfer function defines the output of the system for a given input, summing up all the dynamic processes, including the transmit/receive components and electromechanical properties. The transfer function for an echosounder can be quantified by using the signal received from a known reference target due to a known transmit signal (Hickling, 1962). The transfer function makes up the entire transmit, propagation, scattering, propagation, receive and their combination processes as shown in Figure 3.1.

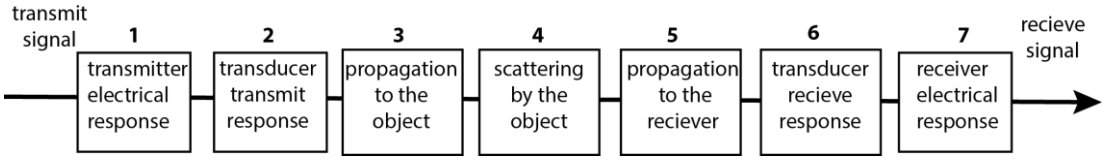

Figure 3.1: A block diagram illustrating all the components involved in the conversion from the transmit signal to the received signal.

The transfer function of the whole process is the sum of three individual transfer functions, the system response, the backscattering response and the response of propagation. The system response is the inclusive response of the transmitter, transducer and the receiver shown as block 1, 2, 6 and 7 in the figure. Once the system response of a system is known, it can easily be used for the calculation of on-axis sensitivity (MacLennan, 1990; Vagle et al., 1996). Given that the system response varies with the frequency and the position of the reference target, it can, in principle, be utilised for directivity compensation, as demonstrated in this study.

This study uses the two-way combined transmit/receive function to calibrate and to

compensate off-axis measurements for the transducer directivity. To include off-axis angles within the acoustic beam, the combined transmit and receive or the system response of the transducer, $H(f)$ is modified to an angle-dependent system response function $H(f,\theta)$. The application is demonstrated through a calibration experiment using standard spheres as targets. Echoes were recorded from two calibration spheres with the broadband transmit pulse set to the 'fast' and 'slow' amplitude ramp. The system transfer function for on-axis and different off-axis positions was derived and utilised to correct target strength measurements. As a verification of the procedure, the results were compared to the theoretical beam pattern models (modified Bessel function and Simrad LOBE algorithm) (Simrad, 2001). The algorithm development was done in the frequency domain, assuming the transducer is circularly symmetric. The terminology used in the chapter is described below in the context of a broadband echosounder.

3.1.1 Off-axis angle

A split-beam echosounder measures the target location at the range, r (m), in the two orthogonal planes as major, α (°) and minor, β (°) angles from the acoustic centre (Raymond Brede, 1990). In spherical coordinates, the location is given by the polar, θ (°) and the azimuthal, φ (°) angles from the acoustic centre (Ehrenberg, 1974). For a circularly symmetric transducer, the polar angle or the off-axis angle is sufficient to describe the target position (shown in Figure 3.2).

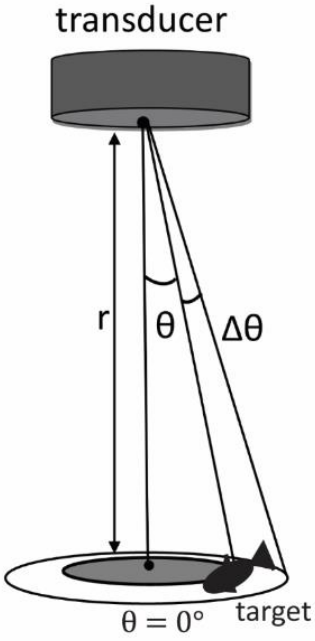

Figure 3.2: Geometric representation of a target's off-axis angle, θ from the acoustic centre. $\Delta\theta$ in the figure is the difference in off-axis angle between two positions.

The off-axis angle, θ is given by Eq. (3.1), where, x_c ($x_c = r\tan\alpha$) and y_c ($y_c = r\tan\beta$). x_c and y_c are the perpendicular distances of a target from the acoustic centre in the x and y directions.

$$\theta = tan^{-1}\left(\frac{\sqrt{{x_c}^2 + {y_c}^2}}{r}\right) \tag{3.1}$$

3.1.2 Transmission Ramping

Time-domain pulse shapes and effective bandwidths can be achieved by multiplying FM waveforms with a Hann window of discrete lengths (Oppenheim, 1999). The Simrad, EK80 software refers to this as ramping (change of amplitude with time) and currently offers two ramp settings for transmission 'fast' and 'slow'. Fast ramping tapers the first and last 10% of a signal leaving a wide, constant amplitude, frequency sweep in the middle. Slow ramping causes half the pulse length to rise and the other half to fall. Autocorrelation of a fast ramp signal yields a broader bandwidth, higher signal to noise ratio (SNR) and higher sidelobes than autocorrelation of a slow-ramp signal. The high side lobes of the fast ramp can overlap when two targets are close to one another, especially if one is much stronger than the other, in which case the side lobes of the

stronger target can completely obscure the weaker target. However, the slow-ramp leads to a smaller bandwidth and hence less information (Demer et al., 2015). The sudden truncation of the fast-ramp signal in the time domain leads to ringing in the frequency domain. This ringing is known as the Gibbs effect and isn't present in the slow-ramp signal (Oppenheim, & Schafer, 2014). In addition to spectral characteristics, ramping also modifies the SNR and the range resolution. This makes the echosounder suitable for a diverse range of applications from the detection of single targets especially when targets are near to each other or near boundaries to the characterisation of dense aggregations at high range (Demer et al., 2017). An optimal calibration approach should involve both signals. A simulation of the fast and slow ramped signals and their power spectra are shown in Figure 3.3. The power spectrum in the frequency domain is the Fourier transform of the time domain autocorrelation function.

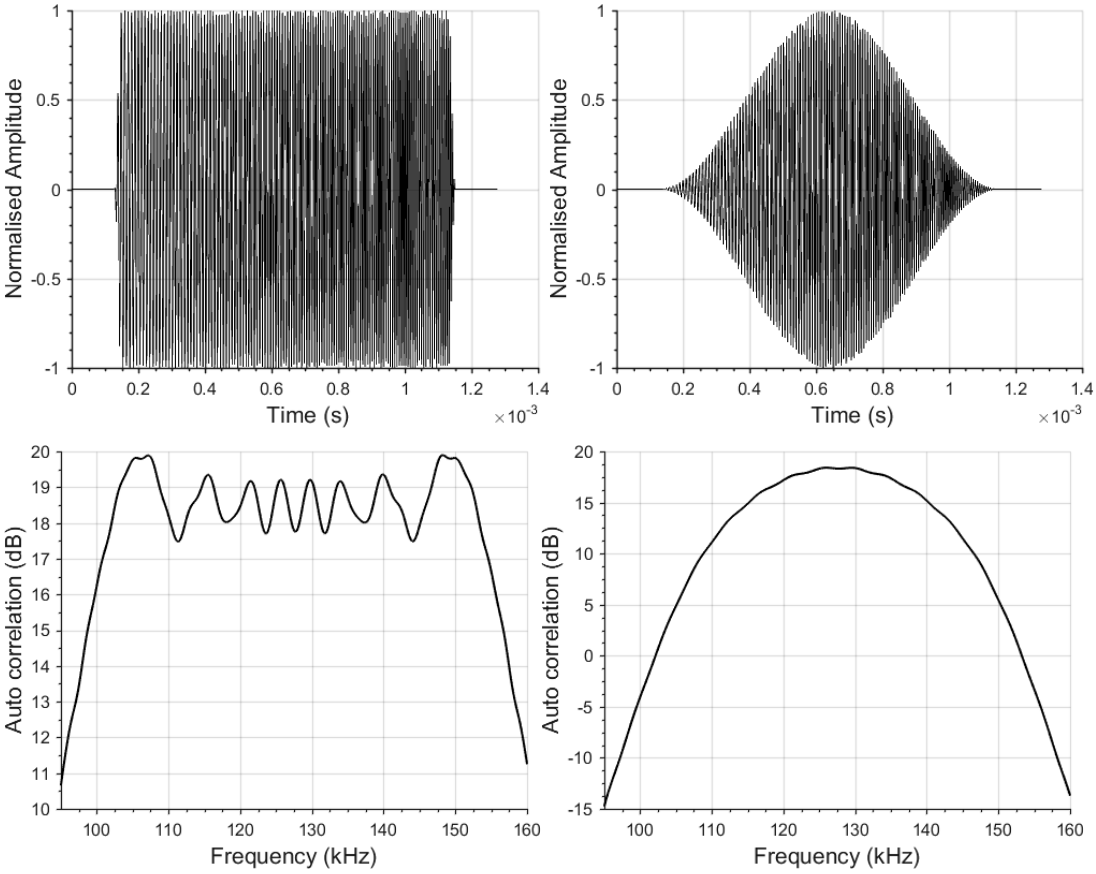

Figure 3.3: Simulated fast ramp (left) and slow-ramp (right) transmit pulses in the time domain (top) and their power spectra in the frequency domain (bottom).

3.1.3 Compensation for the beam pattern

The sound scattered by a target due to an incoming plane wave of unit amplitude and

frequency, f (Hz) is given by the complex backscattering amplitude, $F_{bs}(f)$ (m). The target strength, $TS(f)$ (dB *re* 1m^2) is the logarithmic expression of the modulus of the backscattering amplitude | $F_{bs}(f)$|, given in Eq. (3.2) (Urick, 1983).

$$TS(f) = 10\,log|F_{bs}(f)|^2 \tag{3.2}$$

For a target located at θ within the acoustic beam, $TS(f)$ would require appropriate compensation for the radiation pattern of the transducer. This is achieved by adding a mathematical approximation to the combined transmit and receive beam pattern in the log scale in Eq. (3.3) to the measured target strength $TS_{meas}(f,\theta)$.

$$TS(f) = TS_{meas}(f,\theta) + 10\,log_{10}|B(f,\theta)|^2 \tag{3.3}$$

Where $B(f,\theta)$ is the ratio of the transmitted acoustic intensity at an angle θ and frequency f to its maximum value at the same frequency. For an ideal transducer consisting of a circular piston in an infinite rigid baffle, the one-way beam pattern is given by Eq. (3.4) (Abramowitz, 1965; Urick, 1983).

$$B(f,\theta) = \left(\frac{2J_1(ka\,sin\,\theta)}{(ka\,sin\,\theta)}\right)^2 \tag{3.4}$$

Here J_1 represents the first order cylindrical Bessel function and k (m^{-1}) is the wavenumber. The transducer radius is a $\left(a = \frac{29.5\times\lambda_c}{2\theta_{-3dB}}\right)$ (m) where, λ_c is the wavelength at the centre frequency. The nominal θ_{-3dB} is adjusted to the local sound speed (Bodholt, 2002). Figure 3.4 shows the simulated beam pattern (corresponding to the Simrad ES70-18CD) at frequencies of 50, 70, and 90 kHz. The nominal beamwidth of the transducer is 18° at 70 kHz.

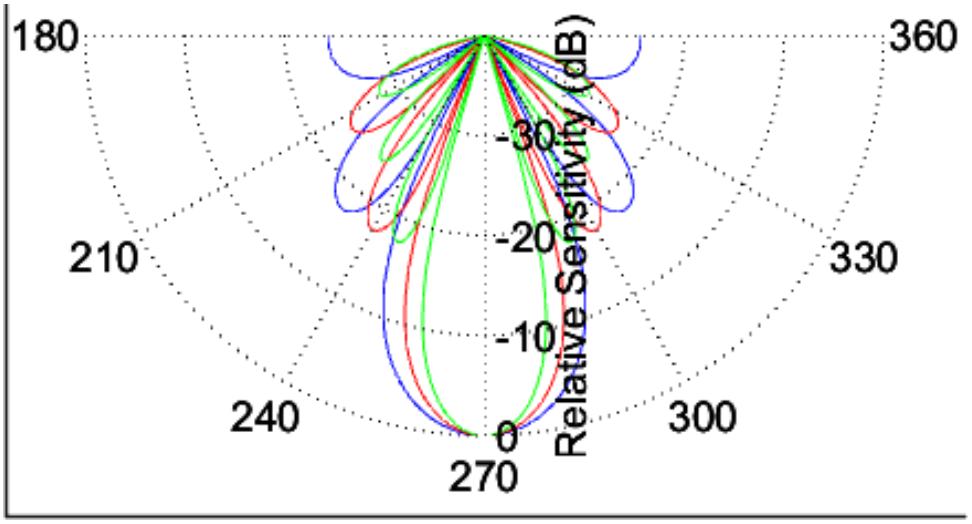

Figure 3.4: An intensity polar plot illustrating the beam pattern of a circular transducer corresponding to the Simrad ES70-18CD at frequencies of 55 kHz (blue), 70 kHz (red) and 90 kHz (green). The beamwidth at the nominal central frequency 70 kHz is 18°.

An alternative beam pattern calculation method is provided by the Simrad LOBE algorithm (Simrad, 2016). The Simrad LOBE algorithm models the two-way beam pattern by a mathematical function $B(\alpha,\beta)^2$, $x = 2(\alpha - \alpha_0)/\alpha_{-3dB}$ and $y = 2(\beta - \beta_0)/\beta_{-3dB}$. Where α_{-3dB} and β_{-3dB} are the major and minor half-beamwidth and α_0, β_0 are the offset angles along the respective axis, Eq. (3.5).

$$10\,log_{10}\,B(\alpha,\beta)^2 = 6.0206(x^2 + y^2 - 0.18x^2y^2) \tag{3.5}$$

3.2 Method and Material

3.2.1 Background theory

A broadband split-beam transducer inputs a transmit signal, $V_T(f)$ which is converted to acoustic waveform by the transmitter. The acoustic signal propagates into the surrounding medium (water) as sound waves. On an encounter with an object in the far-field, the signal is scattered in all directions. The backscattered echo following the propagation through the water reaches the receiver where it is converted to the received electrical signal, $V_R(f)$. This process can be modelled as a linear time-invariant (LTI) system in which the transfer function is given as the ratio of the Fourier transform of the received signal from an off-axis target to the Fourier transform of the transmitted signal. The transfer function of the whole process can be broken down into the product of three individual transfer functions $H(f,\theta)$, $L_{TL}(f)$ and $F_{bs}(f)$ as shown in Figure 3.5.

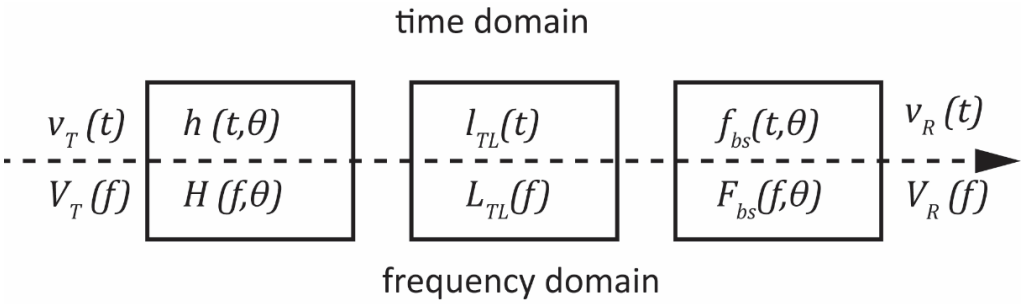

Figure 3.5: A block diagram illustrates the transformation of transmitted voltage to the received voltage as a function of time (top) and frequency (bottom). Symbols in lowercase represent time and uppercase represent the frequency domain. v_T, V_T is the transmitted voltage and v_R, V_R is the received voltage. $h(t,\theta), H(f,\theta)$ is the combined transmit and receive system response of the transceiver. $l_{TL}(t)$, $L_{TL}(f)$ is the transmission function that accounts for the propagation of sound to and from the target. $f_{bs}(t), F_{bs}(f)$ is the backscattering amplitude of an acoustic target.

It is to be noted that $H(f,\theta)$ here includes the directional sensitivity of the transducer at off-axis angle θ. $L_{TL}(f)$ $\left(L_{TL}(f) = \frac{1}{r^2} e^{i\left(\frac{4\pi f}{c_w}\right)r} e^{2\alpha_w(f)r}\right)$ is the transmission function which accounts for the two-way propagation effects including spreading, absorption and propagation delay. $\alpha_w(f)$ is the absorption coefficient, and c_w (m/s) is the sound speed. The received voltage, $V_R(f)$ can be modelled as a product of the transmitted voltage, $V_T(f)$ and all the acoustic components of the transceiver system, as in Eq. (3.6) (Bracewell, 1986).

$$V_R(f) = V_T(f)H(f,\theta)L_{TL}(f)F_{bs}(f) \tag{3.6}$$

Experimentally $H(f,\theta)$ can be determined using a standard target of known theoretical backscattering amplitude $F_{bs,cal}(f)$ and recording the received signal with the target in many positions within the acoustic beam. Thus $F_{bs}(f)$ in Eq. (3.6) can be replaced by $F_{bs,cal}(f)$, and the equation rearranged to solve for $H(f,\theta)$, leading to Eq. (3.7) (Foote, 1982; MacLennan, 1981). The transmitted and received signals are match filtered with a replica of the transmitted pulse giving $CP_T(f)$, $(CP_T(f) = V_T(f)V_T(f)^*)$ and $CP_R(f)$, $(CP_R(f) = V_R(f)V_T(f)^*)$. * indicates the complex conjugate. Alternatively, $CP_T(f)$ and $CP_R(f)$ can be obtained by cross-correlating transmitted and received signals with a replica of the transmitted signal in the time domain and then Fourier transforming (Chu, & Stanton, 1998; Turin, 1960). The pulse compression of a signal reduces the temporal extent and improves the spatial resolution while maintaining the SNR (Ramp, & Wingrove, 1961).

$$H(f,\theta) = \frac{CP_R(f)}{CP_T(f)L_{TL}(f)F_{bs,cal}(f)} \quad (3.7)$$

To derive $TS(f)$ of an unknown acoustic target, $TS_{meas}(f,\theta)$ is obtained by recording backscattered signals from many positions within the acoustic beam and substituting the theoretical beam pattern as shown earlier in Eq. (3.3). Alternatively, $TS(f)$ can be determined using Eq. (3.8). $H(f,\theta)$ incorporates the directional characteristics of the transducer leading to automatic compensation without using mathematical approximations such as the Simrad LOBE algorithm (Eq. (3.5)) or the modified Bessel function for a circular transducer (Eq. (3.4)).

$$TS(f) = 10\,log_{10}\left|\left(\frac{CP_R(f)}{CP_T(f,\theta)L_{TL}(f)H(f,\theta)}\right)\right|^2 \quad (3.8)$$

For a target located at an off-axis angle θ, using $H(f,0)$ in Eq. (3.8) gives the measured target strength, $TS_{meas}(f,\theta)$, Eq. (3.9).

$$TS_{meas}(f,\theta) = 10log\left|\left(\frac{CP_R(f)}{CP_T(f,\theta)L_{TL}(f)H(f,0)}\right)\right|^2 \quad (3.9)$$

3.2.2 Experiment

A series of calibration experiments was performed, at Hobart (Tasmania, 42.88° S, 147.33° E), from the 5th to13th August 2015. The water depth was ~13 m, and the low noise-ambient condition was suitable to conduct calibration. For the experiment, a split-beam broadband transducer (Simrad ES120-7CD) was used. The transducer was positioned facing downward (~1 m beneath the water surface) from a portable platform (Figure 3.6). Two tungsten carbide (6% cobalt binder) spheres of diameter 22 mm (WC22) and 38.1 mm (WC38) were used for calibration (Foote, & MacLennan, 1984). One sphere at a time was suspended between 7 and 10 m directly below the transducer using three monofilament lines. Calculations confirmed that the far-field range was at least three times more than the near-field range ~0.88 m at 120 kHz (Medwin, & Clay, 1998).

Figure 3.6: An illustration of the experiment set up. A downward-facing transducer was positioned on the platform and connected to the Simrad EK80 software via a cable. A calibration sphere was suspended below the transducer, controlled by three monofilament lines attached to fishing reels.

The frequency bandwidth of the echosounder was 95 – 160 kHz with a nominal beamwidth of 7.2° at the centre frequency, 120 kHz. (Simrad, 2016). Backscattered signals were recorded with the sphere on the beam axis ($\theta = 0°$) and moving radially outward in all directions up to 4.0°. Each set of experiments was repeated for both spheres using both fast and slow-ramp transmit signals with all other operational settings remaining the same. The EK80 data acquisition software operated the echosounder. The EK80 software provides a built-in function to calibrate the instrument; however, for the experiment, measurements were recorded outside the calibration mode. The output files were saved in “raw” format. A summary of the nominal transducer parameters and operational settings is given in Table 3.1.

Table 3.1: Broadband transducer specifications and operating parameters.

Parameters	Units	Values
Transducer model		ES120 (WBT 536012)
Transceiver name		WBT 536012
Frequency range	kHz	95 - 160
Centre frequency f_c	kHz	120
Major (α_c) and minor (β_c) axis angles at f_c	°	7.3/7.2
Angle sensitivity		23/23
Offset angle (α_0, β_0)	°	0.03/-0.11
Transmit power	W	200
Pulse length	ms	0.512
Ramp		fast, slow

3.2.3 Acoustic data processing

The backscattered data were match filtered to generate pulse-compressed echograms and derive the 3D coordinates and TS in the time domain (code provided by Andersen, Lars Nonboe from Simrad). Research specific Matlab scripts were developed for further investigations and applications. The average winter temperature and salinity of the estuary (10 °C and 35 p.s.u.) were used to calculate a sound speed of 1491 ms^{-1} at 10 m depth (Mackenzie, 1981). α_{-3dB}, β_{-3dB} and α_w (Francois, & Garrison, 1982) were adjusted to the sound speed. The nominal values of α_{-3dB} and β_{-3dB} were 3.65° and 3.6° making the split-beam transducer circular to 0.1°. α and β measured by the split-beam process were used to estimate the off-axis angle, θ from Eq. (3.1).

Sphere signals were time-gated by an appropriate window function of suitable length. Empirically, a window function should optimise the spectral content, improve the SNR and minimise spectral leakage to other frequencies. Different windows (Rectangular, Hanning and Tukey) and lengths varying from 0.1 to 0.8 m were applied, and the RMS error of the results were compared. Based on the result with the lowest value of RMS error, a Hanning window of 0.4 m length was applied from the peak to both sides of the signal. The model developed by Chu (2011) based on Faran (1951) and MacLennan (1981) was used to calculate the theoretical target strength, $TS_{model}(f)$ of the spheres at the nominal material properties and size.

Measurements using the WC22 sphere were used to compute $H(f, \theta)$ due to this sphere's comparatively flat response across the frequency range. Signals recorded within off-axis angle 0.0°- 4.0° were divided into eight angle bins, each of a width 0.5°.

Due to the open water test site, the possible contamination or interference from other mobile acoustic scatterers within the acoustic sampling volume cannot be ruled out. Therefore as a precaution, poor data points were identified and removed. Assuming a normal distribution of data for each bin only pings within the 95% confidence interval from the mean TS were selected for analysis.

First, the on-axis sensitivity of the broadband system was determined. For the fast-ramp settings, echoes recorded with off-axis angles between 0.00° and 0.01° were used to evaluate the averaged $H(f,0)$, which was then substituted to get the averaged $TS(f)$ (Eq. (3.7) and Eq. (3.8)). The theoretical model of the WC22 sphere was applied for $F_{bs,cal}(f)$. In the case of the slow-ramp setting, the measurement closest to the beam axis was 0.06°, and hence recordings between 0.0° and 0.1° were used to derive the averaged $TS(f)$.

Next, the bin wise averaged $TS(f)$ of the WC38 and WC22 spheres were derived at different positions within the acoustic beam. The averaged $H(f,\theta)$ for all the bins within 0.0°- 4.0° was estimated using signals from WC22 sphere in Eq. (3.7). To compute $TS(f)$ for each ping, the averaged $H(f,\theta)$ was interpolated to the corresponding θ value and substituted in Eq.(3.8). The calculated $TS(f)$ was averaged for each off-axis bin. Due to the non-linear nature of $H(f,\theta)$, the 'spline' interpolation method was selected in Matlab. As a test of accuracy, $TS(f)$ of the spheres were computed using the modified Bessel function in Eq. (3.3) for the set of nominal parameters adjusted to the local sound speed. The residual target strength, $\Delta TS(f)$; $\left(\Delta TS(f) = TS(f) - TS_{model}(f)\right)$ in dB scale, characterised the error of the method. Simrad uses $G(f)$, $(G(f) = 0.5(TS(f) - TS_{model}(f)))$ to express the variation, which is half of the difference between $TS(f)$ and $TS_{model}(f)$ (Andersen, 2001).

3.3 Results

The procedure outlined in Section 3.2 was applied to calibrate the broadband echosounder for both fast and slow-ramp transmit pulses. In total 2595, and 1572 echoes were recorded respectively in the fast-ramp and slow-ramp modes, in the off-axis angle range from 0.0° to 4.0°. This reduced to 2157 and 1486 after the removal of bad data. Selected echoes were binned, as shown in Table 3.2.

Table 3.2: Number of pings in each off-axis angle bin for the fast and slow ramp settings.

Angle bins (°)	Number of pings	
	Fast-ramp	Slow-ramp
0.0 - 0.5	511	89
0.5 - 1.0	405	160
1.0 - 1.5	317	368
1.5 - 2.0	268	145
2.0 - 2.5	387	186
2.5 - 3.0	131	180
3.0 - 3.5	119	321
3.5 - 4.0	19	37

3.3.1 On-axis sensitivity

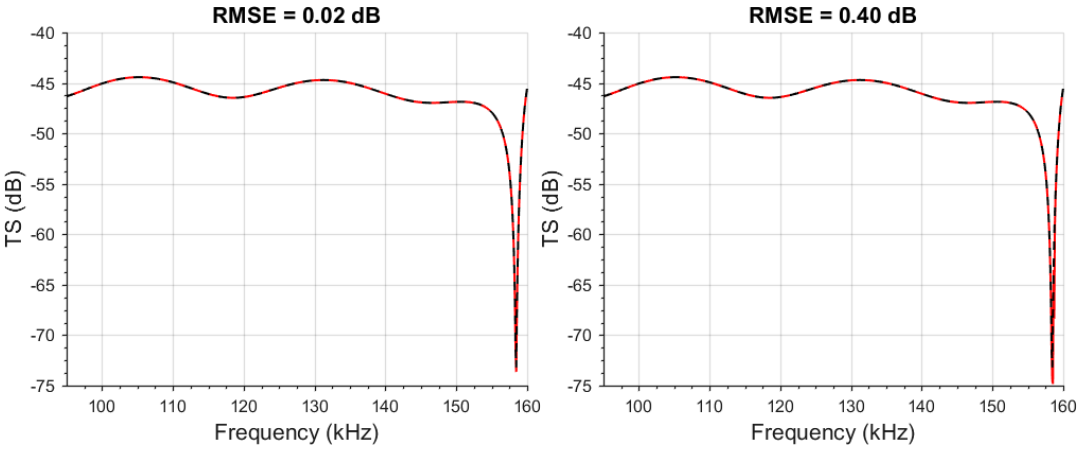

Figure 3.7: Averaged $TS(f)$ drawn in red for the WC22 for angles between 0.0° and 0.01° for the fast-ramp (left) and between 0.0° and 0. 1° for the slow-ramp settings (right). The theoretical prediction is shown in black (--) line.

Figure 3.7 compares the measured and modelled $TS(f)$ on the beam axis. For the fast-ramp, the root mean square of the difference between the theoretical and measured target strength over the entire frequency was 0.02 dB, including the nulls at 158.5 kHz. The RMSE of the slow-ramp was comparatively higher at 0.40 dB, including the nulls. The higher value of RMSE is caused due to the difference at the resonant frequency 158.5 kHz. If we ignore the resonance region, then the curves are almost the same.

3.3.2 Directivity compensation

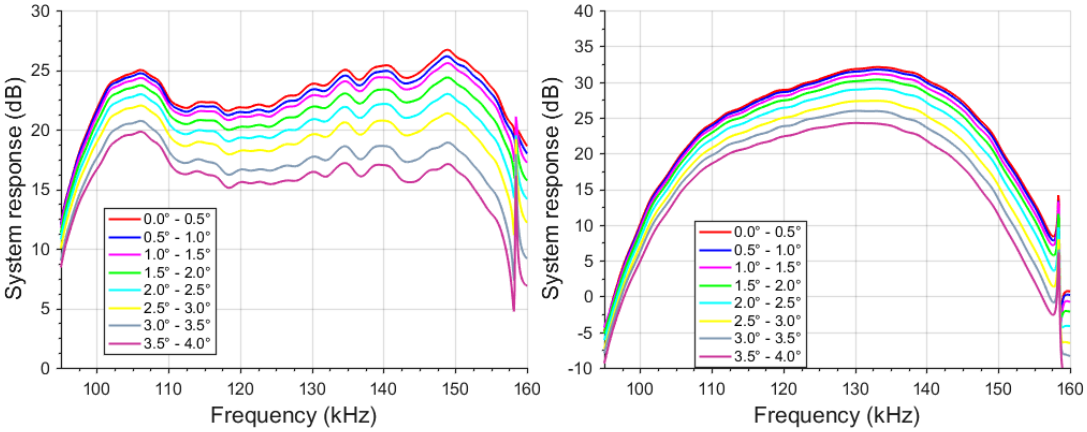

Figure 3.8: The averaged system response in dB $20\,log_{10}|H(f,\theta)|$) plotted against the frequency for different angle bins for the fast (left) and the slow ramp (right). Angle ranges are shown in the legend.

The frequency spectrum of the system response amplitude, $20\log_{10}|(H(f,\theta))|$ averaged for each angle bin is shown in Figure 3.8 for both fast and slow cases. From a maximum amplitude for the bin, $\theta = 0.0° - 0.5°$ the response decreased with increasing bin off-axis angles in both cases. For a given bin, the deviation from the maximum at 0.0° - 0.5° increased non-linearly with the frequency. For example in the fast-ramp case, the difference from the on-axis (0.0° – 0.5°) to the off-axis (3.5° – 4.0°) bin is -3 dB at 95 kHz compared to -12 dB at 160 kHz. This non-linear decrease in the amplitude is a result of the transducer beamwidth becoming narrower at higher frequencies. The shape of the curve is different for fast and slow ramp cases. For the slow-ramp, it has a higher amplitude in the centre which drops significantly at the frequency ends whereas in the fast-ramp case the amplitude is comparatively higher across a larger bandwidth but fluctuates across the band. The reason for the difference is unclear, but it is likely due to the details of the transceiver operation. The presence of distinct sharp spikes at ~158.5 kHz in both cases is due to resonances of the WC22 sphere. The formation of spikes is explained by the peaks and nulls formed by the constructive and destructive interference of the different waves (Hickling, 1962).

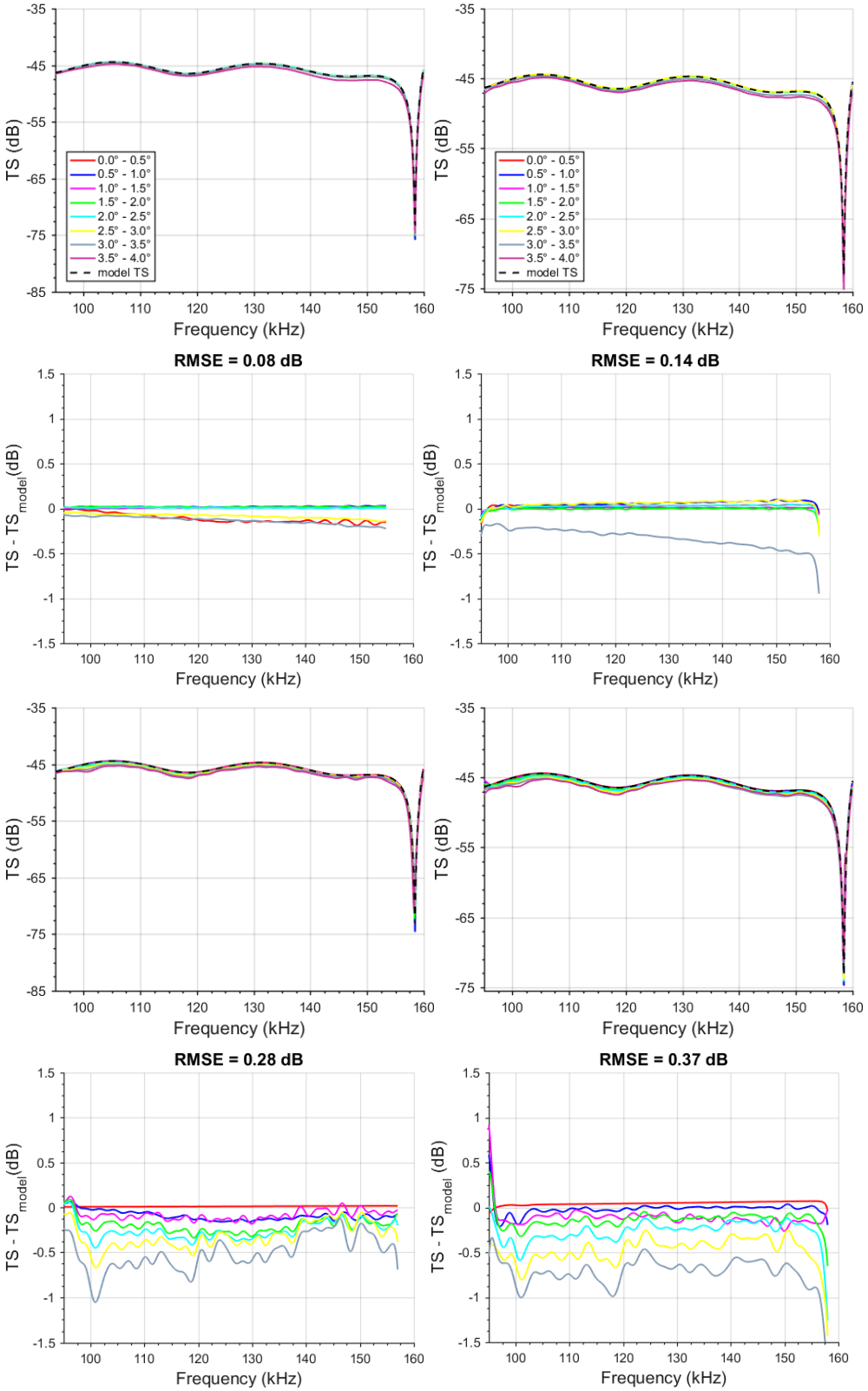

Figure 3.9: $TS(f)$ (top row) and ΔTS, ($\Delta TS(f) = TS(f) - TS_{model}(f)$) (second row) plotted for the WC22 sphere, derived with the system response and $TS(f)$ (third row) and ΔTS (bottom row), derived with the modified Bessel function for the fast (left) and slow ramp (right). The off-axis angles from (0.0° - 3.5°) are shown in legend (top row).

Figure 3.9 compares the averaged $TS(f)$ and $\Delta TS(f)$ obtained for the fast and slow ramp signals using the system response and the modified Bessel function method. The resonant frequency region from 158 - 160 kHz was ignored when calculating $\Delta TS(f)$. The observation confirmed that using $H(f,\theta)$ corresponding to the ping angle compensates for the transducer directivity at all positions within the central beamwidth. The RMSE of $\Delta TS(f)$ with $H(f,\theta)$ was 0.08 dB versus 0.28 dB using $B(f,\theta)$ up to 3.5°. Similarly, for the slow-ramp the compensation with $H(f,\theta)$ yield RMSE of 0.14 dB versus 0.37 dB with $B(f,\theta)$ for angles between 0.0° to 3.5°. For the slow ramp, the compensation was uniform for all bins except for the outermost bin, 3.0° – 3.5° (grey line), which led to a relatively higher RMSE. Also, the low SNR at ends of the frequency band increased the RMSE as compared to the fast-ramp signal. An interesting aspect is that even $H(f,\theta)$ of the farthest off-axis bin (3.5° – 4.0°), which is beyond the nominal half beamwidth (3.6°), completely compensated the signal due to the transducer's directivity.

By using the WC38 sphere as a target, it was demonstrated that $H(f,\theta)$ is a useful metric to calculate $TS(f)$ of other single targets. Acoustic data from a WC38 sphere were recorded with the same operational configurations used for the WC22 sphere measurements (pulse length 512 µs, fast and slow ramp, Hann window, 0.4 m). $TS(f)$ for each ping was derived by substituting $H(f,\theta)$, interpolated to the corresponding off-axis angle value, in Eq. (3.8). The same set of echoes were also compensated with $B(f,\theta)$. For slow-ramp, signals were recorded at off-axis angles up to 3.5°; however, no data were recorded beyond 3.0° for the fast ramp.

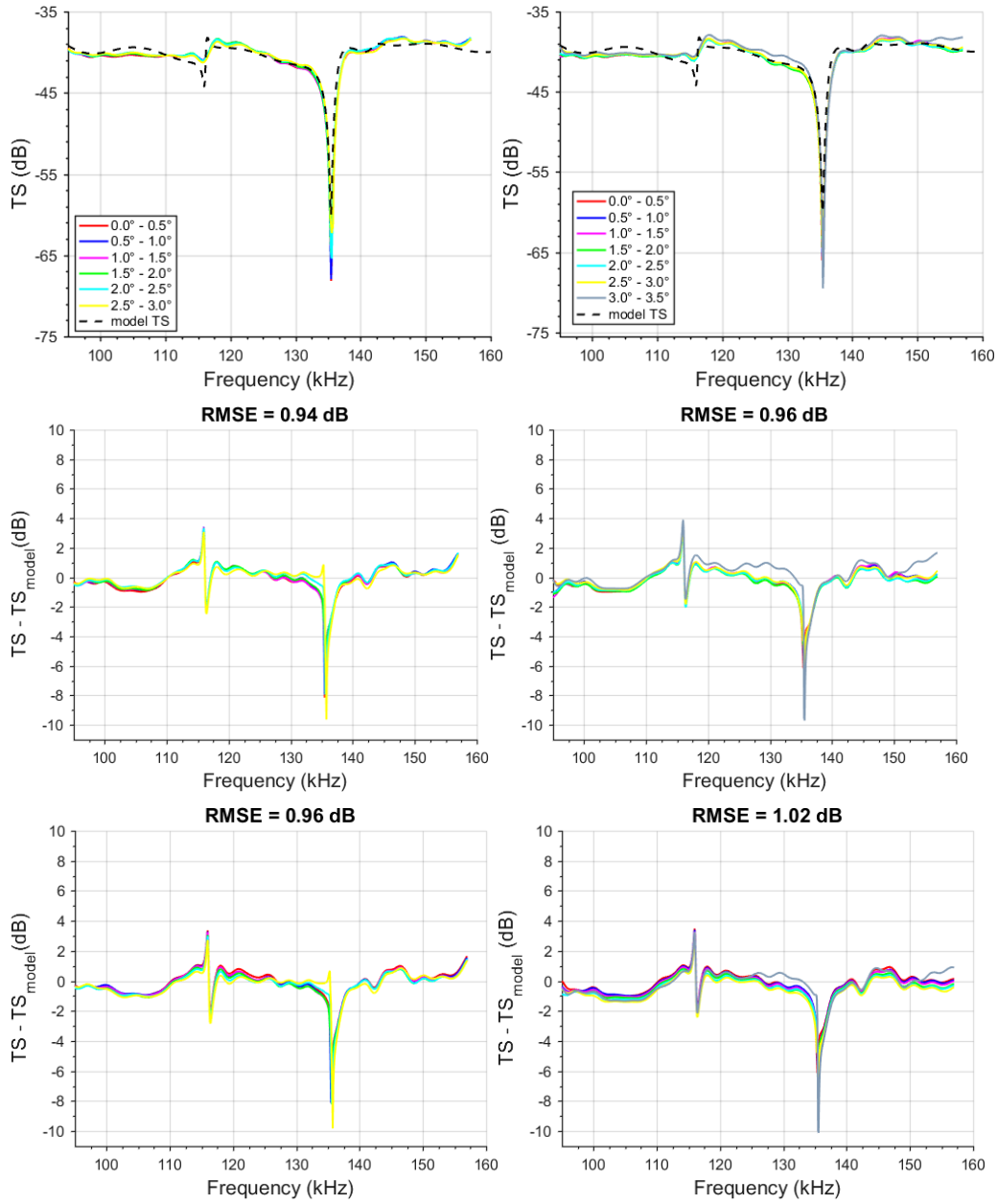

Figure 3.10: Averaged $TS(f)$ for the WC38 sphere (top) and ΔTS ($\Delta TS(f) = TS(f) - TS_{model}(f)$) derived with the system response method (middle) for the fast (left) and slow ramp (right). ΔTS obtained with the Bessel function (bottom) for fast (left) and slow ramp (right).

The averaged $TS(f)$ and $\Delta TS(f)$ for each off-axis bin, obtained using $H(f,\theta)$ and $B(f,\theta)$ for the fast and slow ramp transmitted signals, are plotted against frequency in Figure 3.10. $TS(f)$ responses from both settings were similar in amplitude and behaviour. Using the system response method, the RMSE for fast and slow ramp signals were 0.94 dB and 0.96 dB respectively, compared to 0.96 dB and 1.021 dB for the Bessel function method. The higher RMSE was mainly due to the inclusion of two resonance regions at

116 kHz and 135.5 kHz. Variations were observed between 110 kHz and 120 kHz, and between 130 kHz and 140 kHz, which were consistent for all angles and for both types of transmitting signals. Excluding the regions around the resonances reduced the RMSE from 0.94 dB to 0.96 dB to 0.53 dB and 0.58 dB, for the fast and slow ramp respectively, which is more representative of the ability of the system to characterise smoothly varying scattering responses.

3.4 Discussion

The self-consistency of the method was demonstrated by first calibrating the system using the WC22 sphere and then using it to determine the target strength versus frequency curve of the same sphere. Overall the averaged $TS(f)$ of the WC22 sphere for the on-axis position matched closely to the theoretical value (Figure 3.7) over the frequency bandwidth. There was a comparatively higher residual error in the averaged $TS(f)$ for the slow-ramp, 0.4 dB as compared to 0.02 dB for the fast ramp. This was due to the difference of about 1.65 dB at the bottom of the null. When the resonance region was omitted, the slow-ramp $TS(f)$ agreed with the theoretical value with the error reducing to 0.004 dB. The resonance effect of the standard sphere has been discussed in detail in earlier studies (Chu, & Eastland, 2015; Stanton, & Chu, 2008). One option to reduce the ambiguity is using several calibration spheres of different sizes with resonances at different frequencies and combining the results (Foote, 2007b; Lavery et al., 2017). It should be noted that data were not drawn precisely for the on-axis position instead were averaged values between 0.0° to 0.01° for the fast and 0.0° to 0.1° for the slow-ramp signals. Even after careful manoeuvring, the closest position to the nominal beam axis was 0.016° for fast and 0.065° for the slow-ramp data.

Even though the amplitude ($20\,log_{10}|H(f,\theta)|$) and the variation of the system response curve was different for the fast and slow ramp; the directional sensitivity was consistent (Figure 3.8). When $H(f,\theta)$ was used for directivity compensation for the WC22 sphere, the obtained $TS(f)$ matched closely to the theoretically predicted value confirming the self-consistency of the method. The proposed algorithm compensated the measurements effectively up to 3.5° beyond which deviations begin to appear, indicating the limitation to the half beamwidth (Figure 3.9). The RMS error attained with the system response method (RMSE 0.06 dB and 0.07 dB) was lower than that achieved with the modified Bessel function method (RMSE 0.28 dB and 0.37 dB). In the case of the modified Bessel function method, the deviation increased with the off-axis angle. The

probable cause of this discrepancy was that the effective beamwidth of the transducer was lower than the nominal value causing an under-compensation that increases with the off-axis angles. Compensating with the LOBE algorithm (that users a modified Bessel function) produces a similar result for pings up to 3.5° (not shown in the chapter) (Simrad, 2016). The discrepancy highlights the importance of computing the effective beamwidth for accurate measurements. Using $H(f,\theta)$ had the benefit of taking into account any spatial or temporal change in the acoustic properties of the transducer (Knudsen, 2009) thus making it an appropriate method to calibrate a broadband echosounder.

The analysis in the chapter uses angles (α/β) from the split-beam processing rather than the actual geometric angles. The angle sensitivity of the transducer is critical to enable zero biased measurements. Computing the angle sensitivity was not attempted during the study. Evaluating the angle sensitivity would require an independent measure of the target's actual location (Reynisson, 1998). Measurements performed by the manufacturer confirmed that the acoustic centre corresponds to the on-axis position. Suspending the sphere accurately at the on-axis position would require a special mechanism to carefully manoeuvre the sphere across the three planes (Reynisson, 1998).

The compensated target strength of the WC38 sphere derived with the system response method was uniform for all off-axis angle bins but showed consistent deviation from the theoretical response (Figure 3.10). Other researchers have also reported variability of up to 0.8 dB between the WC22 and WC38 spheres (Hobæk, & Forland, 2013; Lavery et al., 2017). Some potential contributors to explain this observed difference are discussed.

1. Potential error in the $H(f,\theta)$ derived from the WC22 sphere: The $TS_{model}(f)$ used here was computed using the nominal size and material properties of the spheres. The model used; density = 14900 kg/m^3, longitudinal sound speed = 6853 m/s and transversal (shear) sound speed = 4161 m/s. A variation in the effective properties of the experimental sphere from the nominal values could lead to bias, especially at the material resonance (MacLennan, & Dunn, 1984). To achieve a precise result, it is suggested to test the parameters of the calibration sphere. Hobæk, and Forland (2013) recommend an iterative inversion approach to verify the wave speeds. Given the objective of the chapter was to develop a method for the calibration and beam compensation, verification of sphere parameters was not attempted.

2. Contamination from other scattering sources: For no overlap from any nearby targets, the minimum distance for separation from the sphere was (${}^{c\tau}/_{2} = 0.38$ m). Time gating the sphere with a window of length 0.4 m ensured that there were no overlapping side lobes from the seafloor or other nearby targets. The experiment was conducted in an estuary and the possibility of the presence of scatterers of biological or non-biological origin within the window could not be ruled out. However, the presence of biological organisms would have resulted in ping to ping variations which were not visible in the data, which makes this unlikely to be the cause of the observed discrepancies.

3. Interference or reverberations: The WC38 sphere was about 2 m from the seafloor and ~3m from the sidewall. Interference from reflections from these boundaries could contaminate the direct echo from the sphere. Normally in a laboratory tank calibration, the transducer is shielded from the sources of reverberation; which was hard to achieve due to the open environment (Islas-Cital et al., 2010).

4. Bubbles: Presence of bubbles on the sphere surface, water column and suspension lines can be potential contributors to the discrepancy observed. To mitigate bubbles from the sphere surface, they were submerged in soap solution for ten minutes; however, some authors propose a soaking time of up to 4 hours to achieve a consistent result (Hobæk, & Forland, 2013).

Further experimentation is required to identify which of the sources are responsible for the variations observed.

3.4.1 Future Work

A technique to characterise the effective calibration parameters of a broadband echosounder would ensure accurate compensation of measurements. The system response method illustrated in this study can be extended to determine the effective geometrical and directional parameters, as shown in Chapter 4.

A complex broadband scattered signal contains information of the scatterer's morphological and material characteristics embedded in the time-accumulated signal phase. The broadband echosounder is designed to store the received signals as complex waveforms. By retaining the complex waveforms, the complex system response

can be obtained which allows the extraction of the phase spectra of single targets. This target phase (shown in Chapter 5) can be used as a complementary measurement to the amplitude and can be utilised as an additional indicator for remote identification of marine organisms (Barr, & Coombs, 2005).

3.5 Conclusion

The theoretical formulation and experimental verification of the combined system response of a broadband echosounder are presented for calibration and directivity correction. The direction sensitive system response function included the effects of the transceiver settings and the target. The advantage of the method is that it does not require the estimation of the effective beamwidth. Precise calibrations with the WC22 sphere using the fast and slow ramp transmit signals supported the flexibility of the method. The results for the transducer tested provided improved accuracy with RMSE 0.08 dB and 0.14 dB as compared to the standard beam model (Bessel function and LOBE algorithm) with RMSE 0.28 dB and 0.37 dB for the fast and slow ramp settings. For a different target (WC38 sphere) the proposed method generated RMSE of 0.94 dB and 0.96 dB versus RMSE of 0.96 dB and 1.02 dB obtained with the modified Bessel function method for the fast and slow ramp signals.

The technique could be used for laboratory and in situ measurements by choosing an appropriate target. An interesting application would be to obtain compensated target strength measurements of marine organisms' in-situ. This study used the amplitude of the system response and ignored the phase part. By using the system response in the complex form, the broadband echosounder could be calibrated for the phase measurements, as demonstrated in Chapter 5.

Acknowledgement

The authors would like to thank Tim Ryan from CSIRO for his help with the experiment set up and data recordings. Matthew Sherlock from CSIRO is acknowledged for the design and construction of the instrumentation platform. Special thanks to Lars Nonboe Anderson from SIMRAD for providing Matlab scripts to read raw data files. This study was undertaken as a part of the Great Australian Bight Research Program, a collaboration between BP, CSIRO, the South Australian Research and Development Institute (SARDI), the University of Adelaide, and Flinders University.

Chapter 4

A Measurement Model Approach to Characterise a Broadband Split-beam Transducer.

Acoustic measurements made by an echosounder depend on the geometrical (ratio of the radius to the segment distance) and directional (beamwidth and beam pattern) parameters (GDP) of the transducer. At an in-situ condition, the 'effective' values of these parameters may differ from the manufacturer quoted 'nominal' values. This paper describes an inversion (measurement-model) approach to characterise a broadband split-beam transducer. The theoretical modelled beam pattern of a circular transducer, a modified Bessel function, was parametrised to the ratio of the transducer radius to the segment distance. This ratio is referred to as the geometrical parameter (GP) in this study. In a standard calibration sphere set-up, the experimental beam pattern was measured using the on-axis system response. The difference between the measured and modelled beam pattern was minimised in the least-squares sense by allowing the GP to vary within a specified range. Numerical optimisation was carried out by using the Levenberg–Marquardt algorithm to compute the optimum GP. The accuracy and precision of the approach were tested through simulations of target strength. For the combined system (Simrad EK80 and transducer nominal frequency range 95 – 160 kHz), variations of 3 - 4% was observed in the GDP from the manufacturer values for the transducer alone. Once verified, this method could be used to have a simple independent calibration of a systems GP in the field. This particular measurement-model approach is explicitly developed for a wide frequency bandwidth and useful in that it is independent of the local sound speed profile.

4.1 Introduction

There is an increased research interest in the use of broadband echosounders for the high resolution, spectral characterisation and classification of marine organisms (Jech et al., 2017; Reeder et al., 2004; Stanton et al., 2012; Zakharia et al., 1996). A broadband echosounder quantifies the frequency spectra of target strength, $TS(f)$ (dB *re* 1m^2) and / or volume backscattering strength, $S_v(f)$ (dB) from the backscattered sound. These variables are a direct or indirect function of the transducer's beamwidth, θ_{-3dB} (°) and beam pattern, $B(f,\theta)$ (dB) which are functions of the effective radius of the transducer's active area. In particular, $TS(f)$ varies with the target position and requires compensation for the beam parameters. The nominal value of the transducer directional parameters (θ_{-3dB} and $B(f,\theta)$) are estimated by the manufacturer using a controlled laboratory setup (Bodholt, 2002). Large deviations from the manufacturer beam pattern estimate can lead to ~15 - 20% errors in estimated biomass and independent checks of the beam pattern parameters are required (Haris et al., 2017). Also, when transducers are used in the field with a specific echosounder, these parameters may vary from their nominal values due to system response delays and mounting issues (Simmonds, 1984). In such a situation, effective or measured values, rather than the nominal values, are used to describe the behaviour of the transducer. Determination of the transducer's effective geometric and directional parameters (GDP) is also termed as characterisation (Lerch et al., 1996).

At a constant frequency, several studies had earlier quantified the variation of the θ_{-3dB} from its nominal values (Ona, & Vestnes, 1985; Reynisson, 1998). The directivity of a transducer was usually evaluated by mapping the beam at several positions and fitting it with a mathematical function (bicubic spine or a modified Bessel function) (Degnbol, 1988; Kieser, & Ona, 1988; MacLennan, & Svellingen, 1986; Ona, 1990a). At a survey location, it is often challenging to repeat the experiments due to the complicated setup and a lengthy procedure. Consequently, the use of the nominal values adjusted to the local sound speed is an accepted practise during a survey (Demer et al., 2015). A major challenge to find effective values in a broadband echosounder involves consistent prediction over the bandwidth of the system. The methods mentioned above provide effective values only for a fixed frequency and are thus sufficient only for narrowband systems operating at a specific frequency. Extrapolating θ_{-3dB} computed at one frequency to the entire bandwidth can bias the measurements. What is needed for a broadband echosounder is a characterisation or a measurement technique that covers

a range of frequencies.

A transducer consists of several individual piezo-ceramic elements (Wilson, 1988). $B(f,\theta)$ of a circularly symmetric transducer is usually modelled in terms of the modified Bessel function (Urick, 1983). The model assumes the transducer behaves like a rigid piston with a fixed radius of $a\left(a=\frac{29.5\times\lambda_c}{2\theta_{-3dB}}\right)$ at the nominal centre frequency, f_c (Hz) and wavelength λ_c (m^{-1}). Any frequency dependence of a is usually ignored. Past works indicate that this is an adequate approximation for many purposes (Kieser, & Ona, 1988; Medwin, & Clay, 1998). However, in the case of a broadband echosounder, the assumption of a constant radius over the wide frequency bandwidth needs to be verified.

$B(f,\theta)$ of a transducer depends on the speed of sound in the immersion medium (Urick, 1983). Ecosystem acoustics is witnessing a paradigm shift in survey methods to explore the deep-water ecosystems with echosounders mounted on profiling platforms (Kloser et al., 2016; Verma et al., 2017). A downward moving echosounder can experience a change in the sound speed from the value at the water surface which can bias $B(f,\theta)$ if not adjusted appropriately (Haris et al., 2017). Knudsen (2009) proposed using a sound-speed probe for automatic compensation. Moreover, in the absence of an accurate sound speed profile, many research studies use an approximate value of sound speed. Theoretically, the compensation for the beam pattern could be made independent of the local sound speed with an appropriate selection of parameters in the modified Bessel function. This would enable reliable estimates even in the absence of accurate knowledge or considerable change in the sound speed.

The two-way transmit-receive function or the system response of an echosounder system includes the transmitter electrical response, transducer transmit and receive response and the receiver electrical response. Earlier studies in ultrasonics, have demonstrated the use of an on-axis transceiver or system response for the characterisation of spherical transducers (Lerch et al., 1996). In active acoustics, the system response was used to characterise the directional properties of a monostatic echosounder in an in-situ location (Vagle et al., 1996). As an advantage, the system response incorporates the entire process at a given time, including the effects of hardware impairment, ageing or the system mounting. The on-axis system response can be to measure the beam pattern of a broadband echosounder, as shown in this chapter.

The theoretical development, set up and processing is presented in section 4.2, followed

by the result in section 4.3. Finally, the results and limitations of the method are discussed in section 4.4, followed by a conclusion in 4.5.

4.2 Method

4.2.1 Parametrised beam pattern model or Modified Bessel function parametrised to the Geometrical Parameter (GP)

An electroacoustic transducer converts electric signals to acoustic waves at the transmitter end and vice versa at the receiver end (Simmonds, & MacLennan, 2005; Stansfield, & Elliott, 2017). Figure 4.1 shows a schematic view of a split-beam transducer cross-section made up of four quadrants.

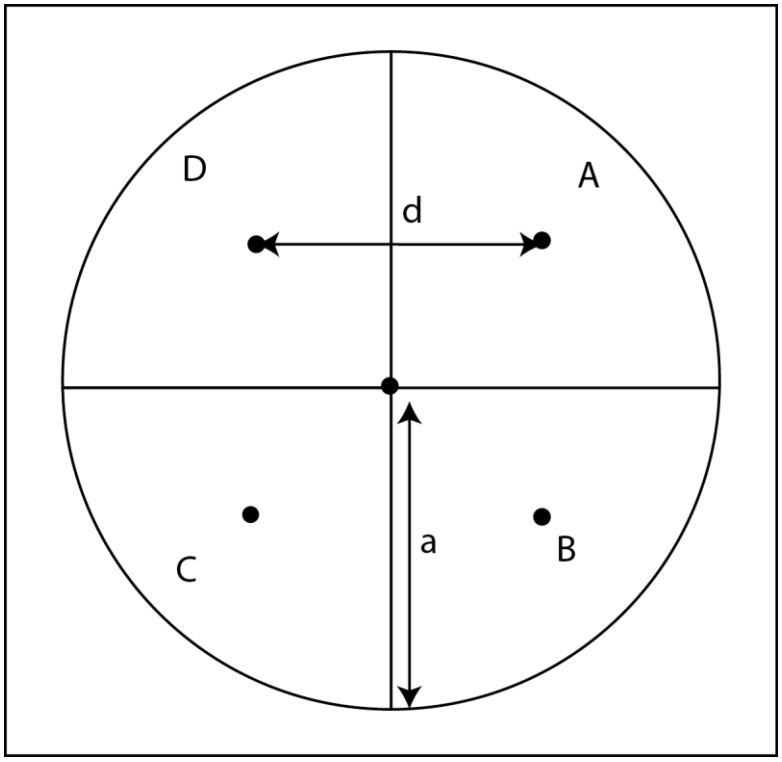

Figure 4.1: A schematic representation of the cross-section of a circular split-beam transducer with four quadrants. The radius of the active area is a, and the separation between the centres of two halves is d.

Here, a is the radius of the transducer's active area and, d is the separation between the two halves, known as the segment distance. The one-way beam pattern of a circular transducer is approximated by Eq. (4.1) (Urick, 1983). $B_{model}(f, \theta)$ is the ratio of the

transducer response at a given off-axis angle to the maximum value in the direction of the beam axis.

$$B_{model}(f,\theta) = \left(\frac{2J_1(x)}{(x)}\right)^2 \quad (4.1)$$

where x is given by Eq. (4.2).

$$x = ka\sin\theta \quad (4.2)$$

J_1 is the first order cylindrical Bessel function at wavenumber, k $(k = 2\pi f/c_w)$ (m^{-1}), at the sound speed, c_w (m/s^{-1}). A split-beam transducer measures the phase difference, ϕ (º), between signals arriving at a pair of transducer segments Eq. (4.3) (Bodholt, 2002; Burdic, 1991).

$$\phi = kd\,sin\theta \quad (4.3)$$

Assuming the phase is measured at the nominal centre frequency, f_c gives $\sin\theta = c_w\phi/2\pi f_c d$ or x as Eq. (4.4).

$$x = \frac{fa}{f_c d}\phi \quad (4.4)$$

The angular sensitivity, Λ (dimensionless) of a transducer is the ratio of the phase angle to the geometric angle and is given by, $\Lambda = \phi/\theta$ (Ona, 1999). The manufacturer provides the nominal value of the angular sensitivity, Λ' and the measurement of beamwidth, θ'_{-3dB} at the sound speed, c'_w at which the calibration was carried out. At an in-situ site, Λ $\left(\Lambda = \Lambda' {}^{c'_w}/_{c_w}\right)$ and θ_{-3dB} $\left(\theta_{-3dB} = \theta'_{-3dB}\,{}^{c'_w}/_{c_w}\right)$ are adjusted to the local sound speed c_w. At the full beamwidth position, $x_{-3dB} = k'a\sin\theta'_{-3dB} = 1.614$ (Kieser, & Ona, 1988), where $k' = 2\pi f_c/c'_w$. For small angles, $\sin\theta \cong \theta$ and the angular sensitivity is approximated as $\Lambda' = k'd$. This gives

$$\xi = \frac{a}{d} = \frac{1.614}{\Lambda'\,sin(\theta'_{-3dB})} \quad (4.5)$$

ξ $(\xi = a/d)$ in Eq. (4.5) is the ratio of the transducer radius to the segment distance. In this study, ξ is referred to as the geometrical parameter or GP of a split-beam broadband

transducer. If the one-way beam pattern, $B_{model}(f,\theta)$ in Eq. (4.1) is parameterised by ξ in Eq. (4.6) then as $B_{model}(f,\theta;\xi)$ is independent of c_w.

$$B_{model}(f,\theta;\xi) = \left(\frac{2J_1(x)}{(x)}\right)^2 \tag{4.6}$$

where

$$x = \frac{f}{f_c}\xi\phi = \frac{f}{f_c}\frac{1.614}{\Lambda' sin(\theta'_{-3dB})}\phi \tag{4.7}$$

Eq. (4.7) is obtained by substituting Eq. (4.5) in Eq. (4.4). It is important that θ'_{-3dB} and Λ' in Eq. (4.7) are evaluated at the same sound speed even if it is not the same as the field sound speed. At $c'_w = c_w$, θ will be the exact geometric angle. An assumption has been made in the study that the phase angle and the beamwidth were determined at the same frequency.

4.2.2 Measured beam pattern

The system response, $H(f)$ is the combined transmit and receive function of the echosounder system at frequency f. In Chapter 3, $H(f)$ was extended to $H(f,\theta)$ to include the directional sensitivity of the transducer at different positions within the acoustic beam. The on-axis response, $H(f,0)$ can be derived by deconvolving the recorded echoes from a standard calibration sphere located on the beam axis ($\theta = 0°$) and substituting the theoretical backscattering amplitude, $F_{cal}(f)$, Eq. (4.8) (Stanton, & Chu, 2008).

$$H(f,0) = \frac{CP_R(f,0)}{CP_T(f)L_{TL}(f)F_{cal}(f)} \tag{4.8}$$

$CP_T(f)$ and $CP_R(f,0)$ are the auto spectrum of the transmit signal and the cross-spectrum of the received and the transmitted signals at the on-axis position (Chu, & Stanton, 1998; Turin, 1960). $L_{TL}(f)$, is the two-way transmission loss due to the propagating medium (seawater). Mathematical development of the method is outlined in section 3.2.1. Once $H(f,0)$ of a system is known, the uncompensated backscattering amplitude, $F_{bs.t}(f,\theta)$ of any acoustic target can be derived as shown in Eq. (4.9)

$$F_{bs,t}(f,\theta) = \frac{CP_R(f,\theta)}{CP_T(f)L_{TL}(f)H(f,0)} \tag{4.9}$$

It is to be noted that $F_{bs.t}(f,\theta)$ is not corrected for the transducer directivity due to the use of $H(f,0)$ instead of $H(f,\theta)$. The difference between the uncompensated measured target strength when the target is off-axis, $TS_{meas}(f,\theta)$, ($TS_{meas} = 10\log\left|F_{bs,t}(f,\theta)\right|^2$ and when the target is on-axis, $TS_{meas}(f,0)$ gives the experimental beam pattern $B_{meas}(f,\theta)$, Eq. (4.10).

$$10log_{10}|B_{meas}(f,\theta)|^2 = TS_{meas}(f,\theta) - TS_{meas}(f,0) \tag{4.10}$$

4.2.3 Inversion algorithm

An inversion problem was formulated by adopting a measurement-model approach. The objective was to estimate the GP that resulted in a modelled beam pattern that matched the measured beam pattern as closely as possible. The cost function, Q, of the inversion algorithm was the sum of the square of the difference between the measured and modelled beam patterns as shown in Eq. (4.11). The function was weighted by the sum of the averaged standard deviation, $\overline{\sigma_m}$ of the signals in each frequency bin. L and H were the lower and the upper limit of the frequency range.

$$Q = \sum_{m=L}^{H}\left(\frac{B_{meas}(f_m,\theta) - B_{model}(f_m,\theta;\xi)}{\overline{\sigma_m}}\right)^2 \tag{4.11}$$

The inversion was a nonlinear least square minimisation problem. The standard Levenberg-Marquardt (LM) method was therefore selected for the parameter estimation. A detailed description of the Levenberg-Marquardt method can be found in Chapter 11 of Press et al. (1988). $B_{model}(f_m,\theta;\xi)$ explicitly depends on ξ which was the property to be fitted. Using a priori information ξ was varied within a confined search space until a minimum Q value was found. To verify the hypothesis of a fixed piston, two different optimisations, both using the LM model were carried out. In the first optimisation, ξ was assumed independent of the frequency and inverted for the single parameter ξ_{e1}. Whereas in the second optimisation, ξ was assumed a linear function of frequency, $\xi_{e2}(f)$ and inverted for ξ_0 and ξ_1 . ξ_0 was a frequency-independent offset and ξ_1 was the coefficient of the term that varies linearly with frequency, as shown in Eq. (4.12).

$$\xi_{e2}(f) = \xi_0 + \frac{\xi_1}{10^7}(f - f_c) \quad (4.12)$$

A scale factor of 10^7 was included so that ξ_0 and ξ_1 were of similar magnitude, which aided the convergence of the cost function minimisation. It was determined by several trials based on the relative importance of each term (Dosso et al., 1993). Once ξ_{e1} and $\xi_{e2}(f)$ were obtained, the corresponding beamwidth,$(\theta_{-3dBe1}\ \ \theta_{-3dBe2})$ and the beam pattern,$(B(f,\theta)_{e1}\ \ B(f,\theta)_{e2})$ could be predicted. The $TS(f)$ compensated for the directivity were simulated using ξ_{e1} and $\xi_{e2}(f)$ in Eq. (4.13).

$$TS(f) = TS_{meas}(f,\theta) + 10\log_{10}|B(f,\theta;\xi)|^2 \quad (4.13)$$

The residual target strength, $\Delta TS(f)$ in dB scale calculated by Eq. (4.14) was used to assess the performance of the algorithm.

$$\Delta TS(f) = TS(f) - TS_{model}(f) \quad (4.14)$$

4.2.4 Setup

A series of experiments were conducted in the Port of Hobart, which is situated near the mouth of the Derwent River, Tasmania, Australia, (42.88° S, 147.33° E) from the 7th to 13th August 2015. The water depth was approximately 13 - 14 m. A Simrad EK80, echosounder was configured with a split-beam transducer (ES120-7CD) covering the frequency range, 95 – 160 kHz. The nominal beamwidth was 7.2° at the nominal centre frequency, 120 kHz. Facing vertically downward, the transducer was positioned ~1 m under the water surface using a pole. The whole system was connected to a temporary platform attached to the dock. A standard tungsten carbide sphere with 6% cobalt binder of diameter 22 mm (WC22) was used as a reference target (Foote et al., 1987; Foote, 1982). The sphere was suspended ~7 - 8 m below the transducer using three monofilament lines. The range confirmed to the far-field at f_c was $D^2/\lambda = 0.88$ (m). D ($D = 2a$) is the diameter of the active area of the transducer (Foote, 1991b).

The sphere was centred on the beam axis ($\theta = 0°$) and systematically moved to different positions within the main lobe. Acoustic backscatter measurements were recorded for both fast and slow ramp transmit pulses, with all other settings kept the same (Table 4.1). Data were recorded outside the calibration settings and stored as complex samples with a ".raw" extension. Refer to section 3.2 for a detailed description of the experimental

setup and procedure.

Table 4.1: Operational configuration of the broadband echosounder.

Parameters	Units	Values
Transducer model		ES120 (WBT 536012)
Transceiver name		WBT 536012
Frequency range	kHz	95 - 160
Centre Frequency fc	kHz	120
Beamwidth at fc (θ_{-3dB})	°	7.28
Angle sensitivity		23/23
Offset angle (α_0, β_0)	°	0.03/-0.11
Transmit power	W	200
Pulse length	ms	0.512
Amplitude ramping		fast, slow

4.2.5 Data processing

The ".raw" files were processed to generate the compensated and uncompensated target strength values in the temporal domain along with the 3D coordinates (range, major and minor axis angle) and time (Matlab codes provided by Andersen, Lars Nonboe from Simrad). Specific codes were developed for further analysis in the frequency domain. The nominal values were used in the study. The calibration sheet confirmed a circular symmetry to 0.1°, (7.3°/7.2°). Using the local variables, (temperature ~10°C and salinity ~35 p.s.u), the sound speed, 1492 m/s (Mackenzie, 1981) and the absorption coefficient (Francois, & Garrison, 1982) were estimated.

To time gate signals from the sphere, a 0.4 m Hanning window was applied from the peak to both sides of the signal. Recorded echoes from 0° and 3.5° off-axis angles were divided into bins of angle width 0.5°. To check for anomalies or random errors due to reverberation and contamination from other sources, bad data points were identified. For each bin, outliers beyond two standard deviations (95% confidence interval for a Gaussian probability) from the mean TS were rejected. $TS_{model}(f)$ of the WC22 sphere was derived using a Matlab script (Chu, 2011) based on the theoretical backscattering model (Faran, 1951; MacLennan, 1981).

The averaged $H(f, \theta)$ of the bin 0° - 0.5° was estimated (section 4.2.2) and extrapolated to derive $H(f, 0)$, using the nearest neighbour method. $TS_{meas}(f, \theta)$ was computed using $H(f, 0)$ as shown in Eq. (4.9). Numerical optimisation of the cost function (section 4.2.3) provided an estimate of, ξ_{e1} and $\xi_{e2}(f)$. The prior value of GP ξ_n was 1.105. Wide and

reasonable boundaries were assigned to ξ to allow for an appropriate inversion result. To avoid uncertainties in the regions close to the null at 157 kHz, and the low SNR ratio from 95 to 100 kHz, samples below 100 kHz and above 155 kHz were excluded from the analysis. Due to the memory limitations of the computer, 150 pings from each off-axis bin were randomly selected, and every 10th frequency point of each ping was input to the minimisation model. To investigate the convergence of the model, the direction parameters ($\theta_{-3dB,}\, B(f,\theta)$) and $TS(f)$ spectrum were generated using ξ_{e1} and $\xi_{e2}(f)$. The Root Mean Square Error (RMSE) of ΔTS, Eq. (4.15) gave the errors estimate.

$$RMSE = \left[n^{-1} \sum_{i=1}^{n} |\Delta TS|^2 \right]^{\frac{1}{2}} \tag{4.15}$$

4.3 Results

The use of the parameterised beam pattern, $B(f,\theta;\xi)$ for beam compensation, as proposed in section 4.2.1, was evaluated. As $B_{model}(f,\theta;\xi)$ is a parametrised form of $B(f,\theta)$, it is anticipated that the compensated $TS(f)$ derived with it should match to the one obtained with $B(f,\theta)$.

Recorded echoes from the sphere (WC22) were processed to generate compensated $TS(f)$, in Eq. (4.13) using $B_{model}(f,\theta)$ Eq. (4.1) and $B_{model}(f,\theta;\xi)$ Eq. (1-6). Signals from both fast and slow ramped transmission were processed.

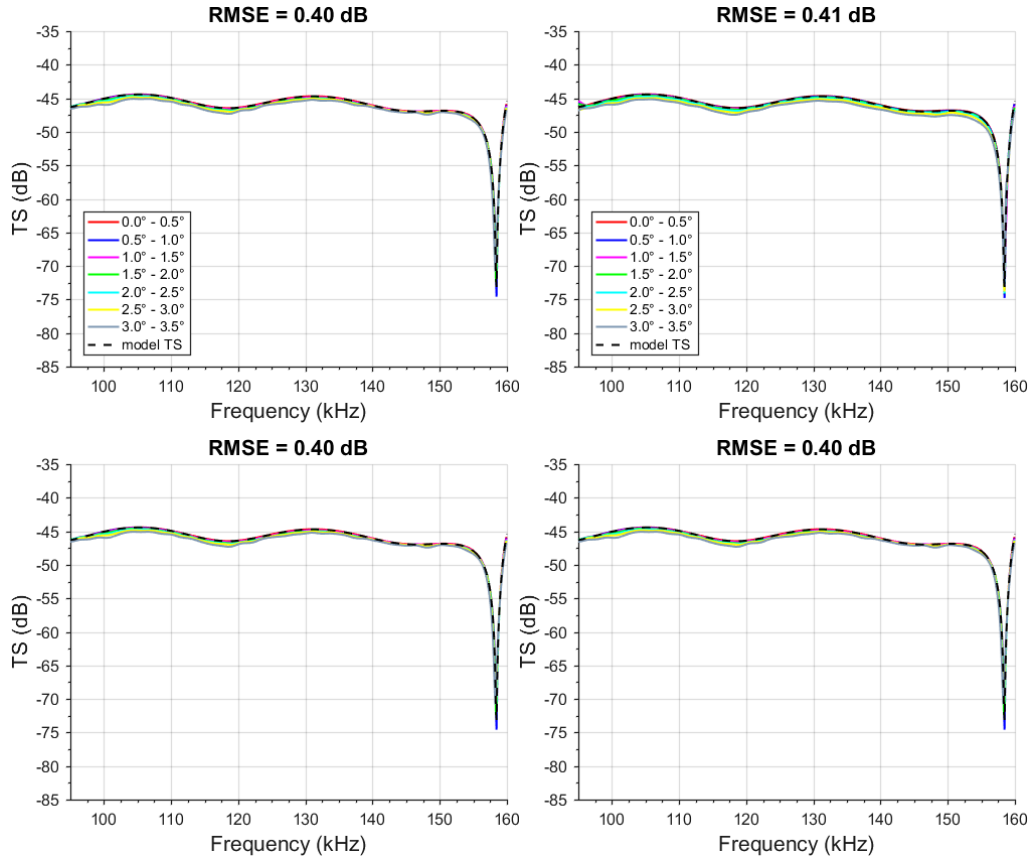

Figure 4.2: Frequency spectrum of bin-wise averaged compensated $TS(f)$ of the WC22 sphere, derived using the parametrised beam pattern, $B(f,\theta;\xi)$ (top) and the modified Bessel function, $B(f,\theta)$ (bottom) for the fast (left), and slow ramp (right) transmitted waveforms. A black (--) line shows the theoretically predicted value. Off-axis angles are shown in the legend.

Figure 4.2 compares the averaged $TS(f)$ of each off-axis bin derived with both the models. As the proposed beam pattern model is a parametrised version of the modified Bessel function, it would be expected that they both yield the same value of $TS(f)$. As anticipated, the compensated $TS(f)$ from both models matched closely, ~0.4 dB, validating the parametrisation of the beam pattern as a function of GP. Compensation with $B_{model}(f,\theta;\xi)$ produced similar results with RMS errors of 0.40 and 0.41 dB respectively for the fast and slow ramp. The RMSE of the residual target strength $\Delta TS(f)$ was 0.40 dB for all sets, inclusive of the nulls at 157 kHz. The nulls were due to the constructive and destructive interference of the waves from the different interfaces of the sphere (Marston et al., 1990; Williams, & Marston, 1986).

4.3.1 Effective parameters

The optimisation provided two outputs for GP a constant, ξ_{e1} and the frequency-

dependent $\xi_{e2}(f)$. The beamwidth, ($\theta_{-3dBe1}\,\theta_{-3dBe2}$), and the one-way beam pattern, (($B(f,\theta)_{e1}$, $B(f,\theta)_{e2}$) corresponding to $\xi_{e1}$and $\xi_{e2}(f)$, were generated as shown inFigure 4.3..

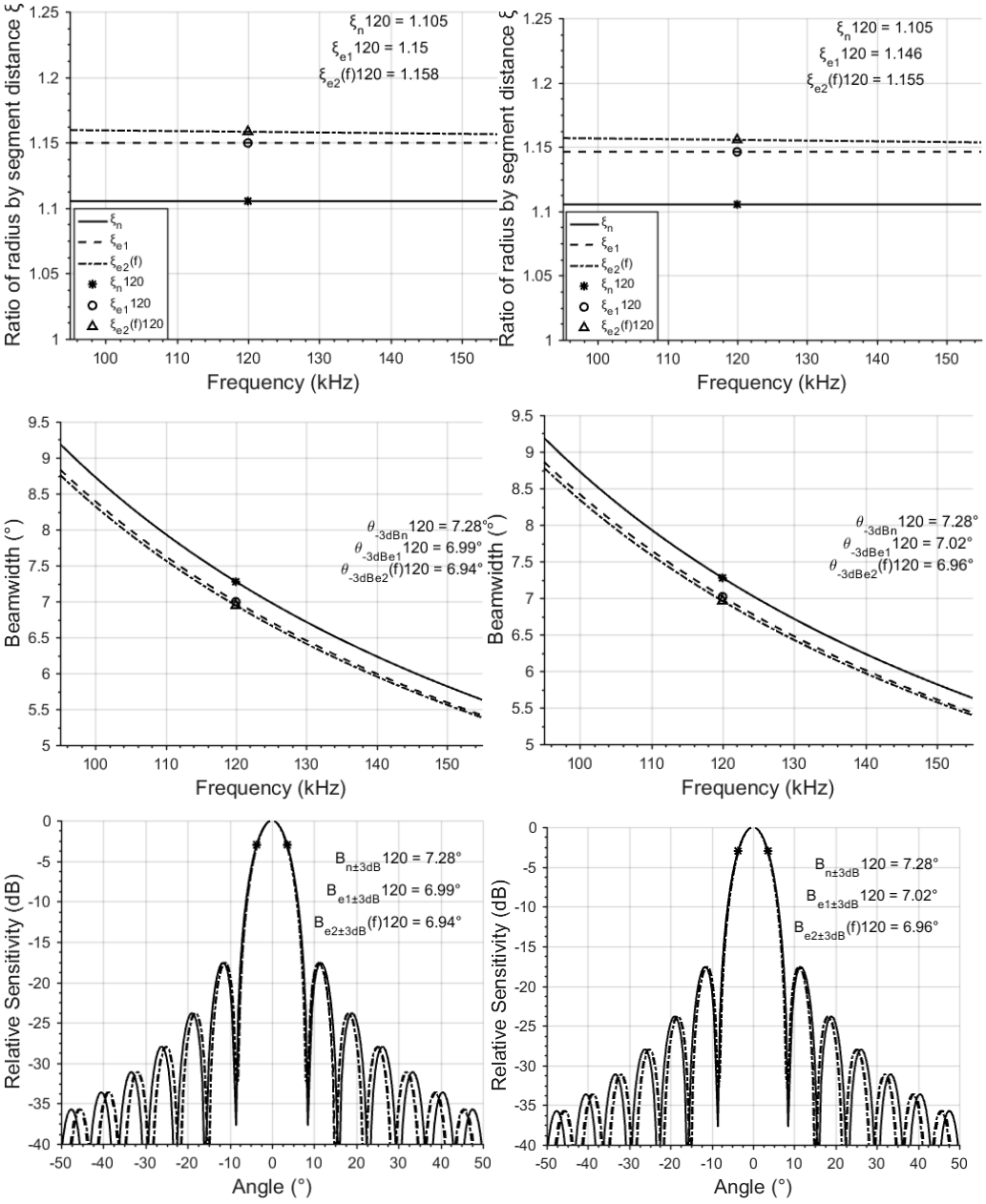

Figure 4.3: The nominal and the inferred GP, ξ_n $\xi_{e1}$and $\xi_e(f)$ plotted against frequency for fast (top left) and slow (top right) ramp signals. The beamwidth (middle) and one-way beam pattern (bottom) derived using $\xi_n, \xi_{e1}\ and\ \xi_{e2}(f)$ for fast (left) and slow (right) ramp signal plotted versus frequency. A *, o and ^ on each curve is the value at, f_c (120 kHz) also shown in the legend.

Overall, the effective GDP was comparable for the fast and slow ramp signals with some minor deviations. For the fast and slow ramps, the derived GP ξ_{e1} was 1.150 and 1.146 rather than the nominal value of 1.105. $\xi_{e2}(f)$ was weakly dependent on the frequency,

leading to an almost constant flat response with frequency. At the centre frequency $\xi_{e2}(f)$ was higher (1.158 and 1.155) than ξ_{e1} (1.150 and 1.146) for both fast and slow ramp. The derived beamwidth and the one-way beam pattern were lower than the respective nominal value. In all cases, the deviation was lower in the slow ramp (<~0.5%) than that for the fast ramp. The results of the LM based inversion are summarised in Table 4.2.

Table 4.2: Transducer nominal and derived parameters at the centre frequency.

Transducer parameters ES120 (WBT 536012)	**Symbols**	**Fast ramp**	**Slow ramp**
The nominal GP, ξ_n	ξ_n	1.105	1.105
Frequency independent GP, ξ_{e1}	ξ_{e1}	1.150	1.146
Frequency-dependent GP, $\xi_{e2}(f)$	ξ_0	1.158	1.155
	ξ_1	-5.253	-5.552
Nominal beamwidth at the centre frequency	$\theta_{-3dBn}(°)$	7.28	7.28
Effective beamwidth at the centre frequency derived with ξ_{e1}	$\theta_{-3dBe1}(°)$	6.99	7.02
Effective beamwidth at the centre frequency derived with $\xi_{e2}(f)$	$\theta_{-3dBe2}(°)$	6.94	6.96

4.3.2 Compensated target strength

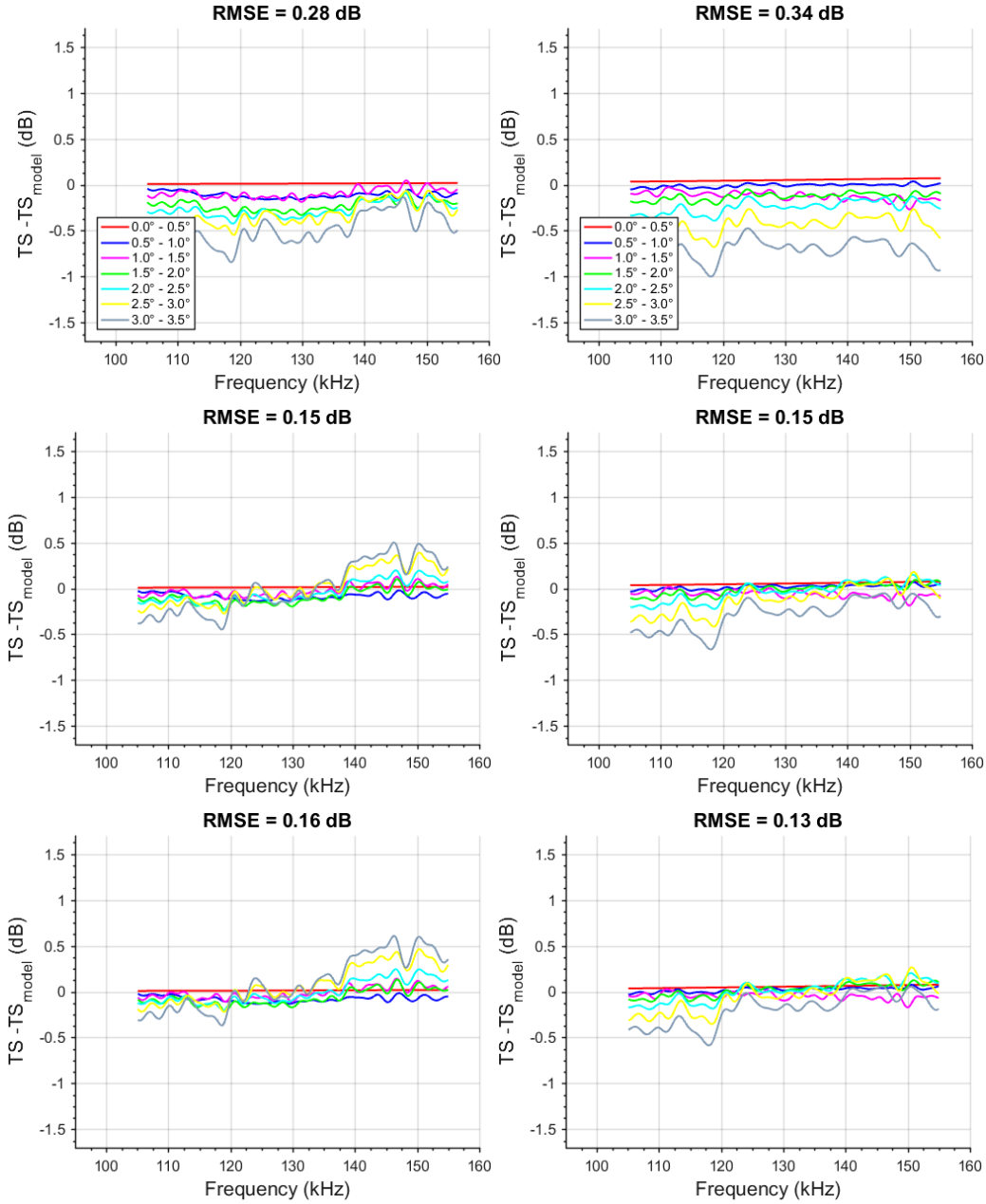

Figure 4.4: The frequency response of the averaged residual target strength ($\Delta TS = TS(f) - TS_{model}(f)$ for each off-axis bin with ξ_n, (top) ξ_{e1} , (middle) and $\xi_{e2}(f)$ (bottom) for the fast (left) and slow (right) ramp.

The implications of the effective parameters for the $TS(f)$ measurements were investigated. $TS(f)$ for each signal was calculated by substituting, ξ_n, ξ_{e1} and $\xi_{e2}(f)$ in Eq. (4.13) and the averaged $\Delta TS(f)$ for each off-axis bin is drawn in Figure 4.4. Using ξ_{e1} improved the performance from RMS error from 0.28 to 0.15 dB and from 0.34 to 0.15 dB for the fast and slow ramping respectively. The plot revealed that including

frequency dependence through $\xi_{e2}(f)$had little effect on the RMSE, with a slight increase from 0.15 dB to 0.16 dB in the case of the fast ramp and a slight decrease from 0.15 dB to 0.13 dB in the case of the slow ramp. The minimisation algorithm led to uneven compensation across the frequency bandwidth. In the case of the fast ramp, compensation in the lower frequency range (<130 kHz) led to overcompensation at higher frequencies (>130 kHz). It was the reverse in the case of the slow ramp where compensation at the higher frequencies (>122 kHz) lead to under-compensation at lower frequencies (<122 kHz).

In a different approach, x $(x = ka\,sin\,\theta)$ from 0 to 2 was divided into bins with a width of 0.1, and corresponding ΔTS values for each signal were binned. To visualise the extent of the distribution, the 5th, 25th, 50th, 75th and the 95th percentiles of each bin were drawn (Figure 4.5).

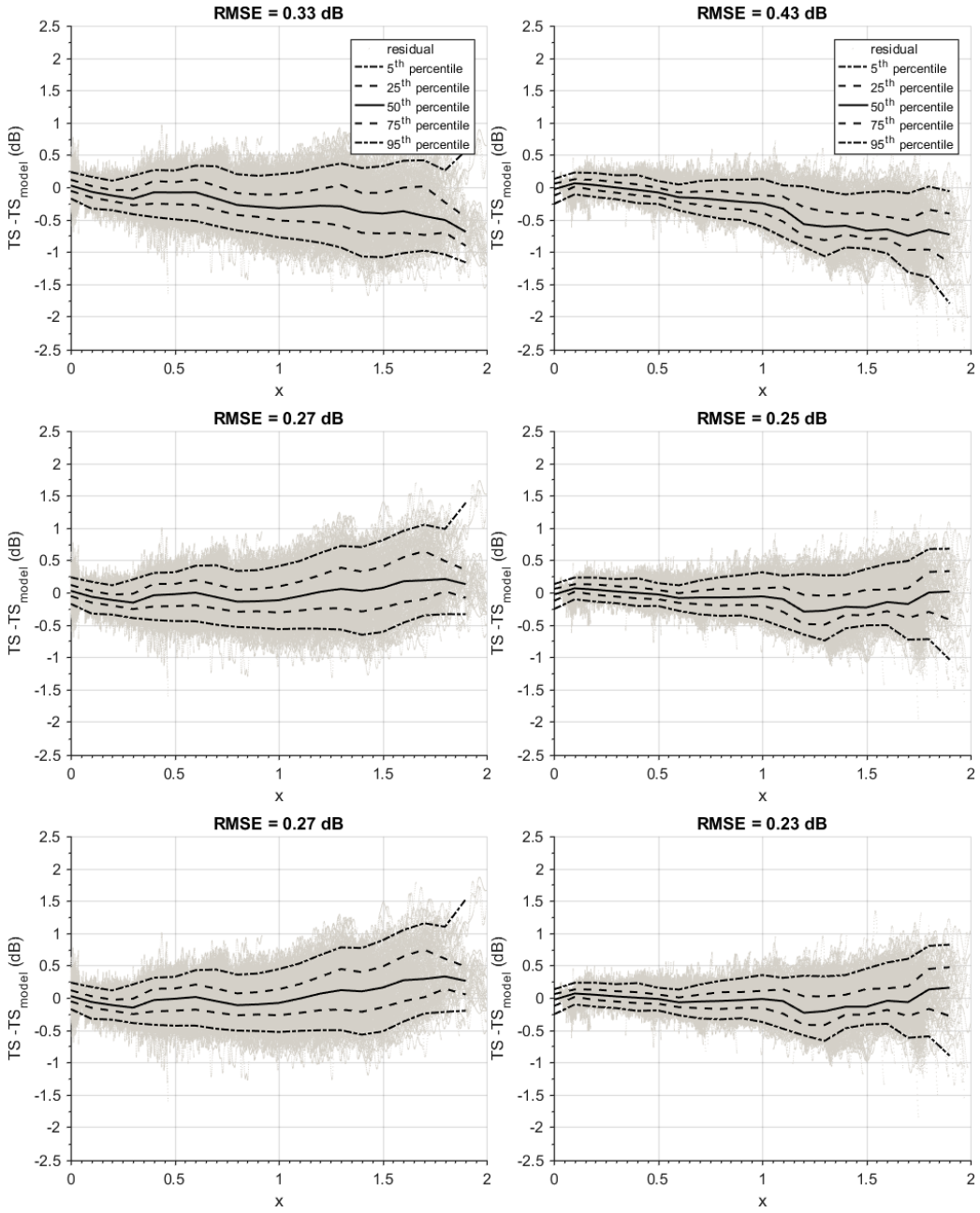

Figure 4.5: Scatter plot of the residual target strength against x ($x = ka\sin\theta$) for ξ_n, (top) ξ_{e1} (middle) and $\xi_{e2}(f)$, (bottom) for fast (left) and slow (right) ramp. The 95th, 75th, 50th, 25th and 5th percentiles of each bin are drawn, also shown in the legend.

Using x enabled visualisation of the combined influence of all frequencies and angles. The value of x varied from 0.0 - 1.15 at 90 kHz, 0.0 – 1.54 at the centre frequency 120 kHz and 0 – 2.06 at 160 kHz. The $\Delta TS(f)$ distribution calculated from the slow ramp was skewed toward the negative side, whereas the fast ramp data had a normal distribution. Using ξ_{e1} improved RMSE from 0.43 dB to 0.25 dB in the slow ramp, as compared to 0.33 dB to 0.27 dB in the fast ramp. No significant improvement was observed using the

frequency-dependent function $\xi_{e2}(f)$, which resulted in RMS errors of 0.27 dB and 0.23 dB respectively for the fast and the slow ramp.

4.4 Discussion

In this chapter, a broadband specific technique was developed to characterise the transducer's geometrical and directional parameters across the entire frequency bandwidth. As a part of the process, the modified Bessel function was parametrised to the GP, and the assumption of a constant GP piston and the frequency dependence of both geometrical and directional parameters were also tested.

4.4.1 Parametrised beam pattern model performance

The parametrisation of the beam pattern in terms of the GP through, $B(f,\theta,\xi)$ removed the dependence on the sound speed. This was unlike the modified Bessel function, which requires the beamwidth fitted to the sound speed to avoid any bias in the output. The validity of $B(f,\theta,\xi)$ was backed by compensating $TS(f)$ of the WC22, standard calibration sphere for two different transmission pulses (fast and slow ramp) and comparing it to the output achieved with the modified Bessel function. An advantage of the new beam pattern parameterisation is that estimates can be made even using the nominal beamwidth. This result could be significant in the deep ocean surveys, where the use of $B(f,\theta;\xi)$ would ensure accurate beam compensation despite variable oceanographic conditions or modification if any in the beam parameters due to the transducer mounting.

4.4.2 Implications of transducer characterisation

The GP of the Simrad EK80 ES120 (WBT 536012) was found to be constant across the frequency range 95 – 160 kHz. This result was obtained by fitting two relationships for the GP, one constant and the other as a linear function of frequency. No noticeable improvement was found using the frequency-dependent GP. However, a set of measurements achieved with only one transducer is not enough to generalise the notion and therefore, verification with other transducers of different sizes and frequency bandwidths is recommended.

The inversion algorithm demonstrated that; for the broadband split-beam transducer used in the experiment, the GP was 3.5 – 4 %, higher and the beamwidth was 3 – 4% lower than the nominal values provided by the manufacturer. For this specific transducer,

working with the nominal beamwidth could lead to a variation in the $TS(f)$ by ~0.12 dB when modified Bessel function is used for beam compensation. Given the importance of $TS(f)$ of single targets in the echo-integration and echo counting, this variation could impact the translation of $TS(f)$ into meaningful ecological attributes such as mesopelagic animal abundance (Benoit-Bird, & Au, 2001) or fish abundance (MacLennan, 1990). For example, $TS(f)$ of several myctophids and deep water fishes are linked to the physical and morphological characteristics of the fish (Kloser et al., 2011) . Nevertheless, using the system response function method, elaborated in Chapter 3, or the parametrised beam model for beam pattern compensation would ensure that $TS(f)$ is precise even if the effective beamwidth differed from the nominal value.

For the transducer used in these experiments, the effective GP and beamwidth for the fast ramp showed larger differences from the nominal values than the slow ramp (Figure 4.3). This was probably due to a higher level of fluctuations that gave data a noisier appearance. These fluctuations in the frequency domain were caused by the sudden truncation of the signal in the time domain (10% slope for the fast ramp) (Oppenheim, & Schafer, 2014). Further investigations would prove beneficial to confirm the observation.

The improvement in the residual ($\Delta TS = TS(f) - TS_{model}(f)$) obtained by using the measured, rather than nominal GP, was quantified in terms of its distribution with off-axis angle and frequency (Figure 4.4). With the effective GP, a consistent decline in $\Delta TS(f)$ was achieved up to 2.5°, beyond which compensation at one end leads to overcompensation or under-compensation at the other. This was seen for both types of amplitude ramping. One possible explanation could be an increasing departure of the true beam pattern from the theoretical beam pattern at angles beyond 2.5°.

From the statistical distribution of $\Delta TS(f)$ with x (Figure 4.5), it can be seen that the spread of $\Delta TS(f)$ with the nominal GP, increases with x. The increase in the width is due to the increase in the uncertainty as the sphere moves further out in the beam pattern. In both cases, moving from nominal to fitted GP does not make any difference to the width of the distribution but reduces the variation with x. Using the effective GP, the mean $\Delta TS(f)$ gets closer to the 0 dB and depends less on x. The standard deviation increases with the increasing value of x but is essentially independent of the method used to measure the GP. However, the improvement in the 95% confidence interval of the $\Delta TS(f)$ distribution to less than ∓ 1 dB suggested that the effective GP describes the system better than the nominal value.

The volume backscattering remains an important index in the echo-integration method for fisheries stock assessments and biomass estimates (Simmonds, 1984). The volume backscattering depends on the actual geometric beamwidth. The analysis presented here was based on the electric angles determined by the split-beam processing and not the actual geometric angles (Bodholt, 2002). Estimation of the geometrical beamwidth would be needed to estimate the effective angle sensitivity, which requires independent measurements of the target's geometric position (Reynisson, 1998), and was not attempted. Independent measurements would require setting up a mechanism that could control the movement of the target This limits the application of the transducer characterisation method described here only to $TS(f)$ measurements and not to the volume backscattering. Both beamwidth and equivalent angle were characterised in Lavery et al. (2010), though the paper does not state whether geometric angles or split-beam electric angles were used.

The proposed characterisation technique is explicitly developed for a broadband echosounder to cover a wide range of frequencies. For turning this experiment to an in-situ operational method, some of the issues that need to be addressed are: (1) an independent experiment to confirm if the material properties of the spheres used in the experiment match to the theoretical values, and (2) extension of the method to characterise an elliptical or rectangular transducer by including the angles along the two planes.

4.5 Conclusion

The characterisation of a broadband split-beam transducer is presented which uses the parametrised beam pattern and on-axis system response in conjunction with the Levenberg-Marquardt (LM) inversion algorithm. Both effective GP and beamwidth differed by 3 - 4% from the respective nominal values. The improvement in the residual target strength distribution supported the use of effective GP and beamwidth. Results indicated that characterisation of the transducer's parameters is crucial to enhance the accuracy of $TS(f)$ measurements primarily when used for classification of marine organisms based on size. This result is significant as nominal parameters are often used in fisheries acoustics. Allowing the GP to vary with frequency did not result in a reduction in RMS residuals, which supports the assumption that a constant GP piston is a good model for the Simrad EK80, ES120, at least when angles are measured in terms of split-beam electrical angles.

Acknowledgement

The authors would like to thank CSIRO, Hobart for providing the infrastructure and the instrument for research. Special thanks to Tim Ryan for the invaluable support in setting up the experiment and the technical guidance during data recording. We appreciate the help from Matthew Sherlock from CSIRO, who designed the platform to deploy the transducer. We want to express our gratitude to Lars Nonboe Anderson from Simrad who provided Matlab scripts to read ".raw" broadband files. This study was undertaken as a part of the Great Australian Bight Research Program, a collaboration between BP, CSIRO, the South Australian Research and Development Institute (SARDI), the University of Adelaide, and Flinders University.

Chapter 5

A Technique for Target Phase Extraction and Calibration of a Broadband Echosounder.

There is a growing interest in the application of broadband echosounders to improve remote sensing of marine organisms. The phase of the backscattered signal contains information about the scatterer's material properties and geometry. There is, therefore, the potential to improve classification methods by measuring both the phase and amplitude of the target's scattering function. A technique is developed to perform a calibration of both the amplitude and phase responses of a Simrad EK80 broadband echosounder. This calibrated response is then used to determine the phase of an unknown target's scattering function. The backscattered signals are retained in complex form and used to obtain the system response with real and imaginary parts. The consistency of the system response phase for different positions within the main lobe indicated insensitivity to the transducer directivity. Three different variables: absolute, differential and residual phase were experimentally measured for two standard spheres (a 22 mm and a 38.1 mm diameter, tungsten carbide sphere with 6% cobalt binder) for fast and slow amplitude ramped transmit signals. When compared to their respective theoretical values; the absolute phase showed offsets and inversions, whereas the differential and residual phase were consistent and free from offsets. Inclusion of phase when comparing measured data to numerical acoustic scattering models has the potential to reduce uncertainties in remote sensing applications and may help to classify targets with similar amplitude responses.

5.1 Introduction

Classifying scatterers using the frequency response of backscattered signals has drawn considerable interest in fisheries acoustics (Au, & Benoit-Bird, 2003; Lee et al., 2012; Stanton, & Chu, 2010). The current sensing techniques typically exploit the signal amplitude, the target strength, $TS(f)$ (dB *re* 1m^2) or the volume backscattering strength, $S_v(f)$, overlooking the presence of additional phase information (Medwin, & Clay, 1998). In situ amplitude measurements are routinely affected by marine diversity (Lavery et al., 2007), organism's behaviour modification (Henderson, & Horne, 2007; Kloser et al., 1997) and interspecies variability within an acoustic sampled volume (Kieser, & Ona, 1988; Stanton et al., 2012). A broadband echosounder receives the backscattered signals from a target with real and imaginary components. The signal includes the target induced phase shift, which if extracted, could serve as an additional descriptor to characterise the scatterer (Atkins et al., 2007; Barr, & Coombs, 2005). However, before phase shift is recognised as a reliable acoustic index, it is important to develop a technique for the calibration of the instrument.

Phase can be a useful parameter in signal processing (Oppenheim, & Lim, 1981). The propagation of a signal through a non-dispersive medium leads to a time-based deviation in the phase that is capable of delivering source information (Mitri et al., 2008). Earlier, the phase has been exploited for image reconstruction and segmentation (Skarbnik et al., 2010) and even speech processing (Shi et al., 2006). In ultrasound imaging, researchers have emphasised the calibration of phase for accurate determination of the sensitivity of the hydrophone (Hayman, & Robinson, 2013; Koch, 2003; Luker, & Van Buren, 1981).

In fisheries acoustics, the first work on phase dates back to the early 1970s when species discrimination was proposed based on hard and soft echoes, (Tucker, & Barnickle, 1969) and was also supported by experimental measurements (Braithwaite, 1973). Later, researchers recommended its feasibility as a classifier for biological species (Chestnut et al., 1979; Giryn, 1982). However, there were no immediate follow-ups due to the computational limitations and the lack of instruments capable of measuring complex waveforms. In the early 2000s, Barr, and Coombs (2005) exploited the rate of change of target phase to classify fishes from planktons with similar target strength. The need for calibration of echosounders for phase measurements was also pointed out. Sonar systems were calibrated for the phase by extending the standard calibration approach

for dual-frequency continuous waves (CW) (Islas-Cital et al., 2011b) and linear frequency modulated (LFM) transmission pulses (Islas-Cital et al., 2011a). Substantial agreement between the measurements and the theoretical prediction implied the feasibility of the method. The work was performed in controlled conditions, and the sphere limited to the on-axis position without addressing the effect of the transducer directivity.

For exploitation in fisheries, several technical aspects need to be addressed to uncover a scatterer's information from the phase (Horne, 2000; Nakken, & Olsen, 1977). Defined as the arctangent of the ratio of the imaginary to real parts of the Fourier Transform of a signal, the phase remains wrapped within 360° (2π radians) (Tribolet, 1977) which masks the actual response. Unmodeled propagation delays lead to a range dependent linear phase accumulation, posing challenges in delivering quantifiable phase information (Lyon, 1984). Additional sources of uncertainties such as the low signal to noise ratio (SNR), frequency resolution and dispersion effects, control the measurement accuracy. The presence of additive noise and interference from other acoustic sources can further degrade the analysis (Matsumoto, 1990). Thus, incorporation of phase for target characterisation requires advanced techniques to process complex signals, computation tools to work in the frequency domain, and quantifiable variables to negate the propagation delay effects.

To provide meaningful phase measurement, instrument calibration across the frequency bandwidth is of utmost importance. For a split-beam transducer, this would involve addressing two main aspects (1) the on-axis sensitivity and (2) correction of off-axis measurements for the transducer directivity. Phase calibration can be attained by extending the standard sphere calibration approach (Demer et al., 2015; Stanton, & Chu, 2008). The Simrad EK80, broadband echosounder comes with two choices for shaping the transmit pulse (fast and slow ramping) achieved by applying Hann windows of different lengths to the transmit signal in the time domain (Oppenheim, 1999). The calibration of an echosounder on both settings would ensure optimum phase measurement in different circumstances.

This study investigates the use of the complex system response for extraction and calibration of phase measurements. Three variables, absolute, differential and residual phase, are presented for visualisation of target-induced distortion. The paper is organised as follows. The terminology is introduced in section 5.2, followed by the description of the theoretical development, experimental setup and the processing

technique. In section 5.3, measurements from two standard calibration spheres are presented. The uncertainties and possible application to target classification are discussed in section 5.4, followed by a conclusion in 5.5.

5.2 Methods

Some key terminology associated with analysis is described below. Note that all the variables are discussed in the frequency domain.

5.2.1.1 Absolute phase

The frequency, f (Hz) spectrum of the non-linear back scatterer phase, $W\varphi_{bs}(f)$, (°) is wrapped within modulo 360° for every circular rotation which gives it a sawtooth shape (Lyon, 1983). Several algorithms have been developed to avert the wrapping (Al-Nashi, 1989; Spagnolini, 1995). The Matlab 'unwrap' function adjusts the angle by adding $\pm 360°$, whenever the jump between consecutive elements is higher than the default value $\pm 180°$. Unwrapping of the signal reveals the actual phase, $\varphi_{bs}(f)$ (°) information Eq. (5.1).

$$\varphi_{bs}(f) = unwrap(W\varphi_{bs}(f)) \tag{5.1}$$

Extra care should be taken while using 'unwrap' to avoid sudden jumps due to low-frequency resolution, discontinuities and additive noise (Nadeborn et al., 1996). The location of zeros can introduce uncertainties during unwrapping (Quatieri, & Oppenheim, 1981; Tribolet, 1977). In addition, the propagation of a signal through a non-dispersive medium leads to a distance-dependent, linear accumulation in the phase (Lyon, 1983, 1984) removal of which is crucial to reveal the modification caused by the scatterer.

5.2.1.2 Differential phase.

One approach is to visualise the differential (gradient) of the phase with respect to frequency, $DP(f)$ (°/Hz) which magnifies the target induced properties (Yen et al., 1990). Calculating the differential converts the linear ramp in $\varphi_{bs}(f)$ to an offset in $DP(f)$ (Eq. (5.2)). The $DP(f)$ was also applied by Mitri et al. (2008) and referred to as the rate of change of phase or RCP.

$$DP(f) = \frac{d\varphi_{bs}}{df} \tag{5.2}$$

5.2.1.3 Residual phase

Although $DP(f)$ removes the range accumulation, sudden jumps can make clear interpretation difficult. The changes due to the range errors are linear functions of frequency, which if removed, would enable visualisation of the target induced phase shift. This can be achieved by estimating the linear least-squares fit and then removing it. For this purpose, we use the residual phase, $RP(f)$ (°) which is obtained by subtracting the product of the frequency and the median of the differential phase from the absolute phase (Eq. (5.3)).

$$RP(f) = \varphi_{bs}(f) - (f \times median(DP(f)) \quad (5.3)$$

The median is used to minimise the effect of substantial changes in the differential phase due to the target response. The proposed method to calculate the residual phase improves on the linear least-squares fit. A linear fit would distort the residual phase as the target-induced phase is non zero whereas the median is a more robust estimator. This procedure can lead to a frequency-independent offset between the residual phase and the actual phase that can be removed by subtracting the mean of the residual phase. An example of $W\varphi_{bs}(f)$, $\varphi_{bs}(f)$, $DP(f)$ and $RP(f)$ spectra for a tungsten carbide (6% cobalt binder) sphere of 22 mm diameter are shown in Figure 5.1.

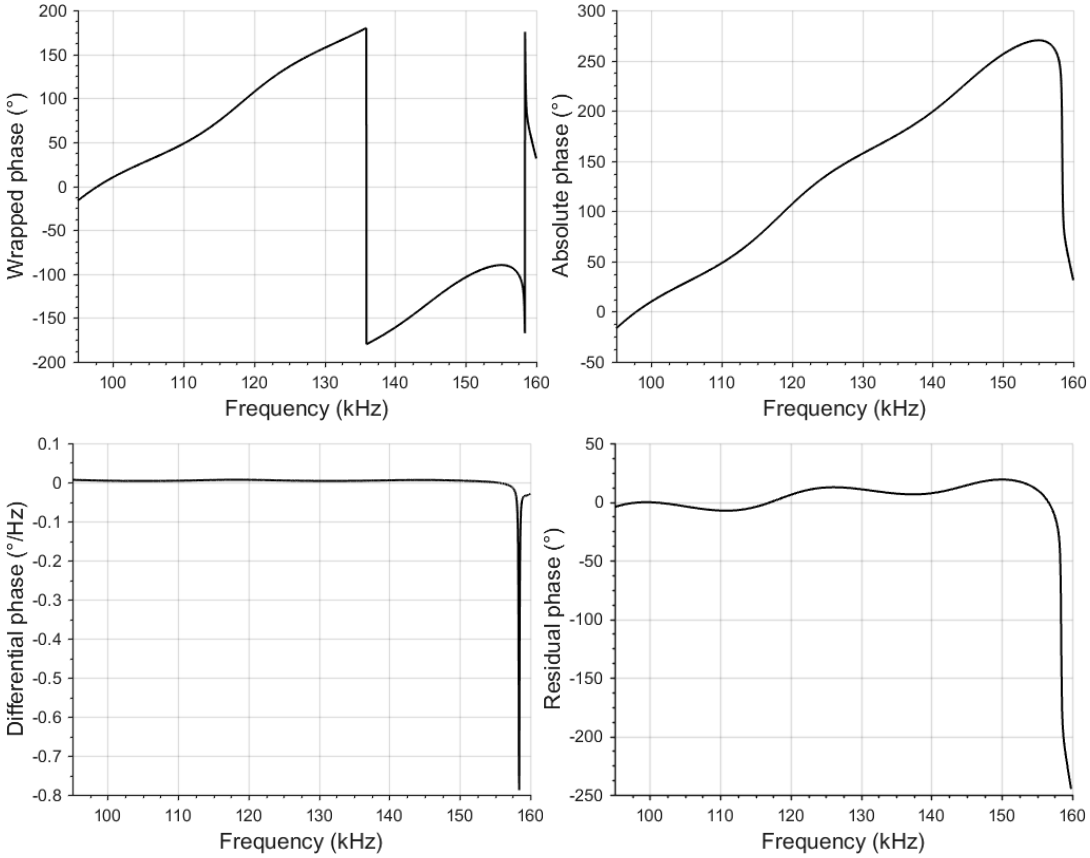

Figure 5.1: The frequency spectrum of the wrapped (top left), absolute (top right), differential (bottom left) and residual phase (bottom right) for a tungsten carbide (6% cobalt binder) sphere of 22 mm diameter.

5.2.2 Theoretical development

The theoretical development of a procedure to calibrate a broadband echosounder for both its phase and amplitude response is described. Note that the background treatment discussed in this section is relatively brief; for a more in-depth description refer to Chapter 3.

A transmitter transmits frequency modulated (FM) waveforms that undergo modifications due to scattering by a single target in the far-field. The receiver receives the backscattered sound. An echosounder can be modelled as a linear time-invariant (LTI) system (Foote, 1983). The received voltage, $V_R(f,\theta)$, can be expressed as a product of the transmitted voltage, $V_T(f,\theta)$, and the transfer function of the three individual components, $L_{TL}(f)$, $H(f,\theta)$ and $F_{bs}(f)$ (He, 1999) as shown in Eq. (5.4). $V_R(f,\theta)$, $V_T(f,\theta)$ and $H(f,\theta)$ are functions of both frequency and off-axis angle, θ (°).

$$V_R(f,\theta) = V_T(f,\theta)H(f,\theta)L_{TL}(f)F_{bs}(f) \tag{5.4}$$

In the equation, $L_{TL}(f)$ ($L_{TL}(f) = \frac{1}{r^2} e^{i\left(\frac{4\pi f}{c_w}\right)r} e^{2\alpha_w(f)r}$) is the two-way transmission loss function, which includes the effect of signal propagation and wave spreading. Here r (m) is the range, c_w (m/s) is the sound speed in water and $\alpha_w(f)$ (dB/m) is the absorption coefficient. The system response $H(f,\theta)$ sums up the responses of all components of an echosounder, including the transmitter and receiver electrical responses and the transducer transmit and receive responses at a given frequency and off-axis angle. Incorporating θ compensates for the effect of transducer directional sensitivity. Mathematically $H(f,\theta)$ is a complex function, ($H(f,\theta) = A(f,\theta)e^{i\varphi(f,\theta)}$) with an amplitude, $A(f,\theta)$, and a phase, $\varphi(f,\theta)$(Heyser, 1969; Islas-Cital et al., 2011b). For a target on the beam axis, ($\theta = 0°$) with no directional dependence, $F_{bs}(f)$ is the backscattered amplitude. The target strength is the modulus of the backscattered amplitude in the logarithmic scale given by Eq. (5.5) (Urick, 1983).

$$TS(f) = 10\, log_{10}|F_{bs}|^2 \tag{5.5}$$

Experimentally, $H(f,\theta)$ can be approximated by recording backscattered signals from a standard target of a known backscattering amplitude $F_{bs,cal}(f)$ positioned at different positions within the main lobe of the transducer's beam pattern (Eq. (5.6)). The pulse compressed received, $CP_R(f,\theta)$ and transmitted signals, $CP_T(f,\theta)$ are computed by multiplying each with the complex conjugate of the replica of the transmitted signal (Chu, & Stanton, 1998; Turin, 1960).

$$H(f,\theta) = \frac{CP_R(f,\theta)}{CP_T(f,\theta)L_{TL}(f)F_{bs,cal}(f)} \tag{5.6}$$

Once $H(f,\theta)$ is determined, $F_{bs}(f)$ of an unknown target can be derived via Eq. (5.7).

$$F_{bs}(f) = \frac{CP_R(f,\theta)}{CP_T(f,\theta)L_{TL}(f)H(f,\theta)} \tag{5.7}$$

The objective of using $H(f,\theta)$ is to compensate the transducers directivity. The angle or the arctangent function of $F_{bs}(f)$, yields $W\varphi_{bs}(f)$ which can be unwrapped to give $\varphi_{bs}(f)$ (Eq. (5.8)). The complex exponential term in the transmission function removes the phase ramp in Eq. (5.6) if the transmit/receive delay is known exactly. In practice, the transmit/receive delay has to be estimated from the data and estimation uncertainties lead to some residual phase ramp.

$$\varphi_{bs}(f) = unwrap(angle(F_{bs}(f)) \quad (5.8)$$

5.2.3 Experimental setup

A series of standard calibration experiments was conducted in the estuary of the Derwent River in Hobart, Tasmania, from 10th to 13th August 2015. The water was approximately 13 m deep. A Simrad EK80 split-beam broadband echosounder (ES120-7CD) with frequency bandwidth 95 – 160 kHz was used. The nominal beamwidth at its centre frequency of 120 kHz was 7.2°. The transducer was mounted facing vertically downward under the water surface (~1 m) using a pole connected to an onshore platform.

For the first trial, a 22 mm diameter, tungsten carbide sphere with 6% cobalt binder (WC22) was suspended in the far-field region of the transducer, (~7 - 8 m) using three monofilament lines. Backscattered sounds were recorded by moving the sphere from on-axis to many off-axis positions within the acoustic beam. Next, a 38.1 mm diameter (WC38) sphere made of the same material, was used (Foote, & MacLennan, 1984) and recordings were obtained by repeating the process. Two sets of recordings were obtained for each sphere. The first set was with a fast ramp transmit pulse and the second set was with a slow ramp transmit pulse. The pulse length was 0.512 μs in both cases.

5.2.4 Signal processing

The initial processing read "*.raw" files to derive backscattered energy and the 3D coordinates and plot pulse-compressed echograms using Matlab code provided by Lars Nonboe Anderson from Simrad, Kongsberg Maritime. Specific Matlab programs were then developed by the authors to compute the complex system response and the spectra of phase variables.

A WC22 sphere was used to compute the system response, $H(f,\theta)$ for the frequency range 95 – 160 kHz, although not ideal (Demer et al., 2015),. The frequency response is flat between95 – 160 kHz, except for - nulls at 158.5 kHz due to resonance. The nulls are caused by constructive and destructive interference of the backscattered signals from the different interfaces of the sphere (Marston et al., 1990; Überall, 1973; Williams, & Marston, 1986). To time gate the sphere signal, a Hann window of length 0.7 m was applied from the peak to both sides of the pulse-compressed waveform. Recordings from 0° - 4° off-axis angles were partitioned into bins of angle width 0.5°. Due to the sensitivity, pings lying outside two standard deviations from the mean TS values (95% confidence

error for a Gaussian distribution) for each bin were removed. The bin wise averaged $H(f,\theta)$ was obtained by substituting the $F_{bs,cal}(f)$ in Eq. (5.6). A free to download Matlab based code developed by Chu (2011)was used to compute the $F_{bs,cal}(f)$ based on Faran (1951) and Foote, and MacLennan (1984). It was assumed that the material properties and the size of the experimental spheres matched to their modelled values.

To derive the $F_{bs}(f)$ of the spheres, recordings from each were divided into off-axis bins of width 0.5° from 0.0° – 3.5° and pings from each bin outside the 95% confidence interval were removed. The averaged $H(f,\theta)$ was interpolated to the off-angle of the ping, and the resulting values used in Eq. (5.7) to obtain $F_{bs}(f)$. The $\varphi_{bs}(f)$, $DP(f)$ and $RP(f)$ for each ping were determined using Eq. (5.8), Eq. (5.2) and Eq. (5.3) and averaged for each angle bin.

5.3 Results

To derive the frequency response of the phase and demonstrate the effect of transducer directivity the system response at the on-axis and off-axis positions were obtained for both the fast and the slow ramp transmission. The self-consistency of the method is depicted through the phase variables plotted for the WC22 sphere at both the ramps. Once verified the application of the method to extract the phase of other targets is shown via the WC38 sphere.

5.3.1 System response (on-axis and off-axis)

Figure 5.2 and Figure 5.3 shows the frequency response of the amplitude and the absolute, differential and residual phase of $H(f,0)$ for the fast ramp and slow ramp transmitted waveforms. It is to be noted that the $H(f,0)$ response shown here was not measured at a constant range and angle, but was determined by averaging 511 (fast) and 89 (slow) pings between 0° and 0.5°.

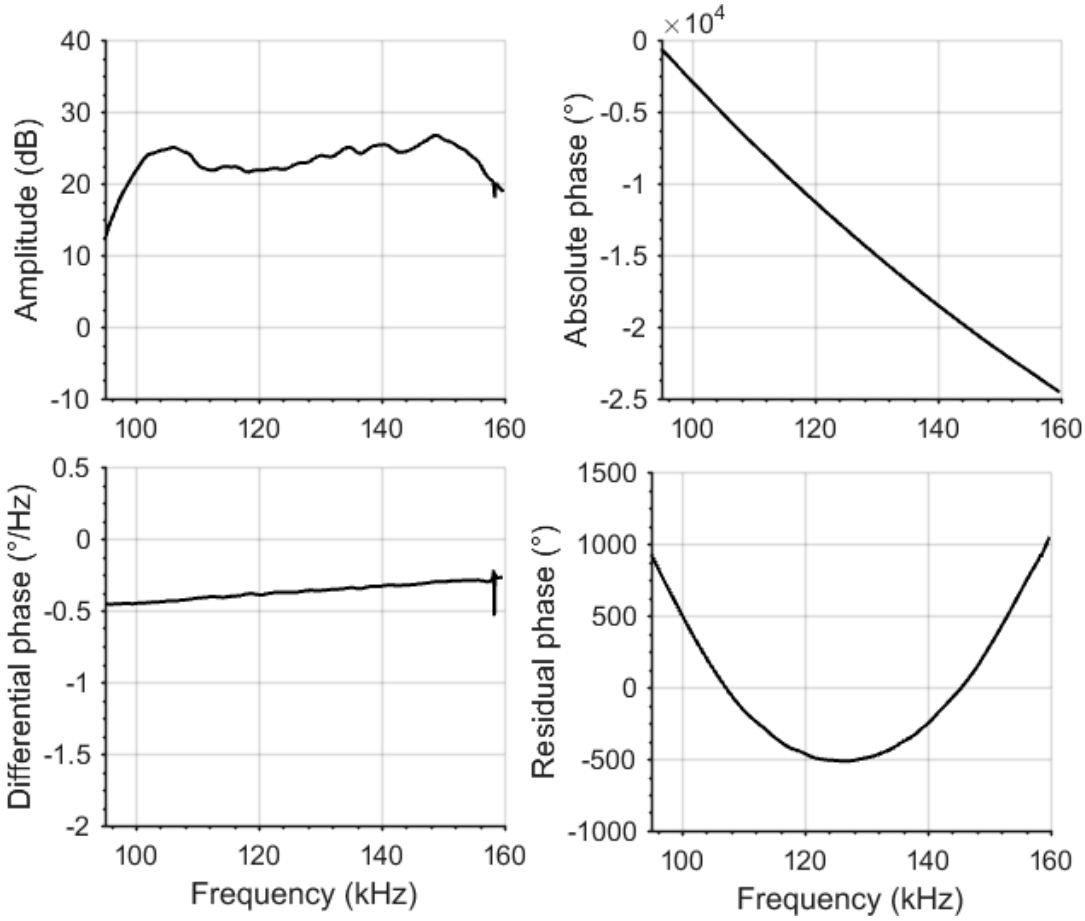

Figure 5.2: The amplitude and the absolute, differential and residual phases of the system response of the echosounder for the fast ramp transmitted waveforms.

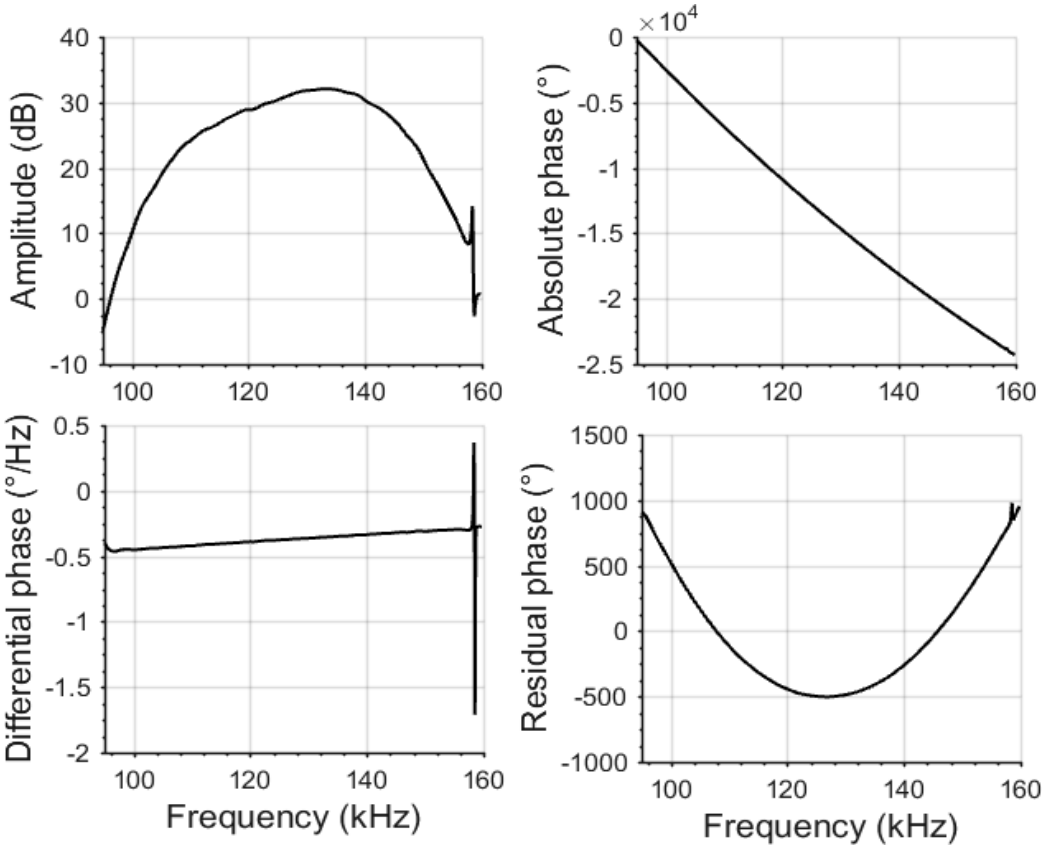

Figure 5.3: The amplitude and the absolute, differential and residual phases of the system response of the echosounder for the slow ramp transmitted waveforms.

For the fast-ramp, the amplitude, ($20\log_{10}|H(f,0)|$) had a broader peak than that for the slow-ramp. Moreover, it was smoother for the slow ramp versus oscillating for the fast ramp. $\varphi(f,0)$ (f), appeared the same for both cases, decreasing nonlinearly with frequency. Because of the high slope (-0.385 °/Hz), the actual response of the transceiver could not be visualised. Computing the differential phase removed accumulation with increasing range. $DP(f)$ for both ramps was consistent and exhibited the characteristic resonance at the 158.5 kHz. The null is an artefact of the calibration process due to the use of the WC22 sphere and is not part of the true system response. The overall structure remained masked due to the null. The linear slope (-2.7x10^{-6}.°/Hz^2) observed in $DP(f)$ was likely due to the delay caused by the time difference between the original and assumed travel time of the signal. The nulls were higher for the fast and lower for the slow ramp signals. The $RP(f)$ computed for $H(f,0)$ for both the ramps was quadratic in nature with the lowest point at 127 kHz. No significant difference was noticed between the results obtained using the two different transmit signals.

$H(f,\theta)$ averaged for each off-axis bin 0.5° from 0° to 4° was computed as outlined in

section5.2.4. The half beamwidth extended up to 3.5°, the bin 3.5° - 4.0° was included to examine the response beyond. Figure 5.4 shows the bin wise frequency response of the $\varphi(f)$, $DP(f)$ and $RP(f)$ derived for $H(f,\theta)$.

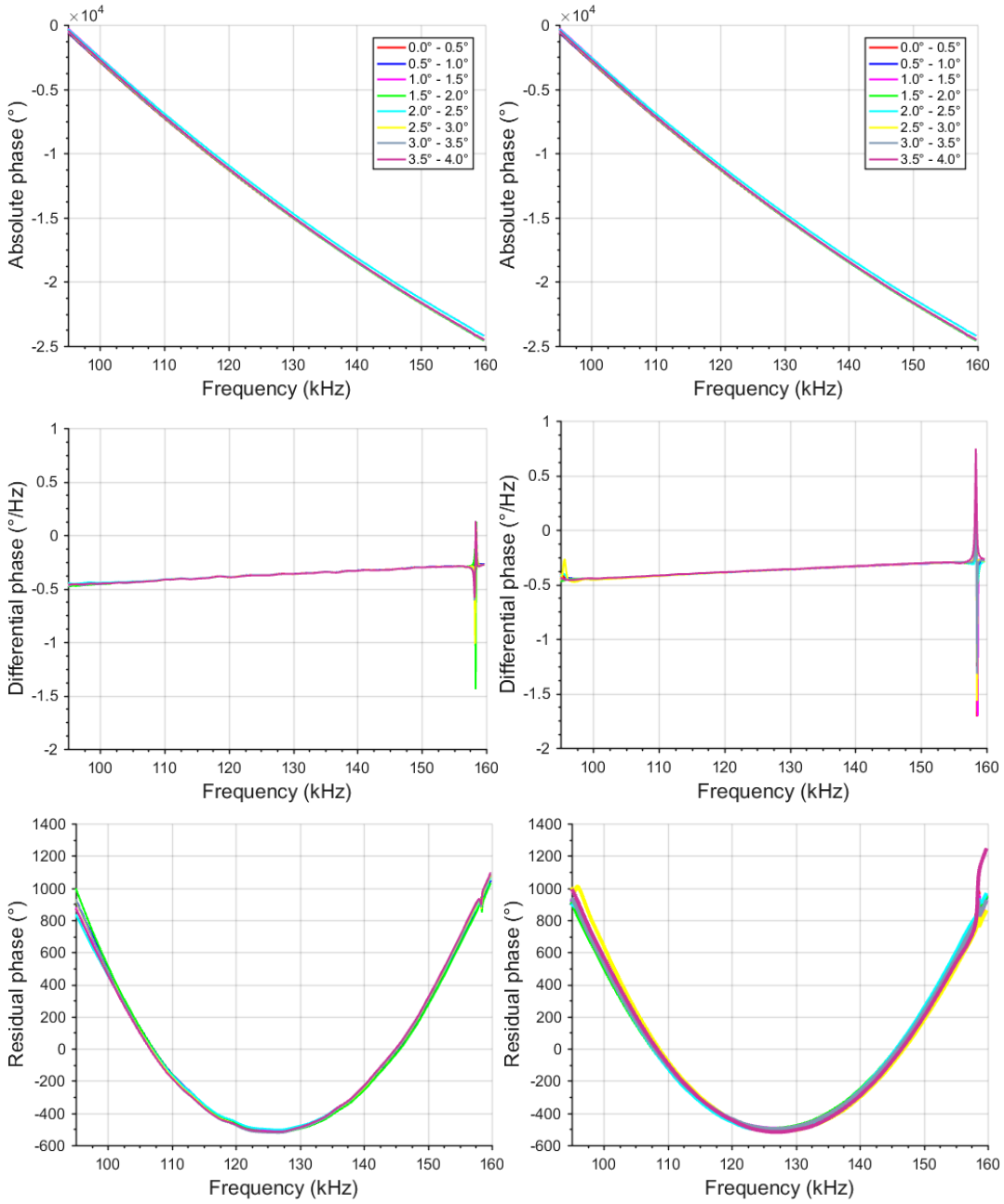

Figure 5.4: The absolute (top), differential (middle) and the residual phase (bottom) of the system response drawn for the fast (left) and slow (right) ramp transmitted waveforms. Sharp nulls at 158.5 kHz are due to the resonance effect of backscattered signals.

$\varphi_{bs}(f)$, $DP(f)$ and $RP(f)$ derived for all the off-axis bins were equal to the on-axis value ($angle(H(f,\theta)) = angle(H(f,0))$) except at the nulls where the peaks were different for

each bin. There was no influence of the transducer directivity on the phase measurements within the main beam. It could be concluded that the system phase response will be the same at different off-axis angles and can be derived by either substituting $H(f,0)$ or $H(f,\theta)$ in Eq.(5.6).

5.3.2 The frequency response of phase

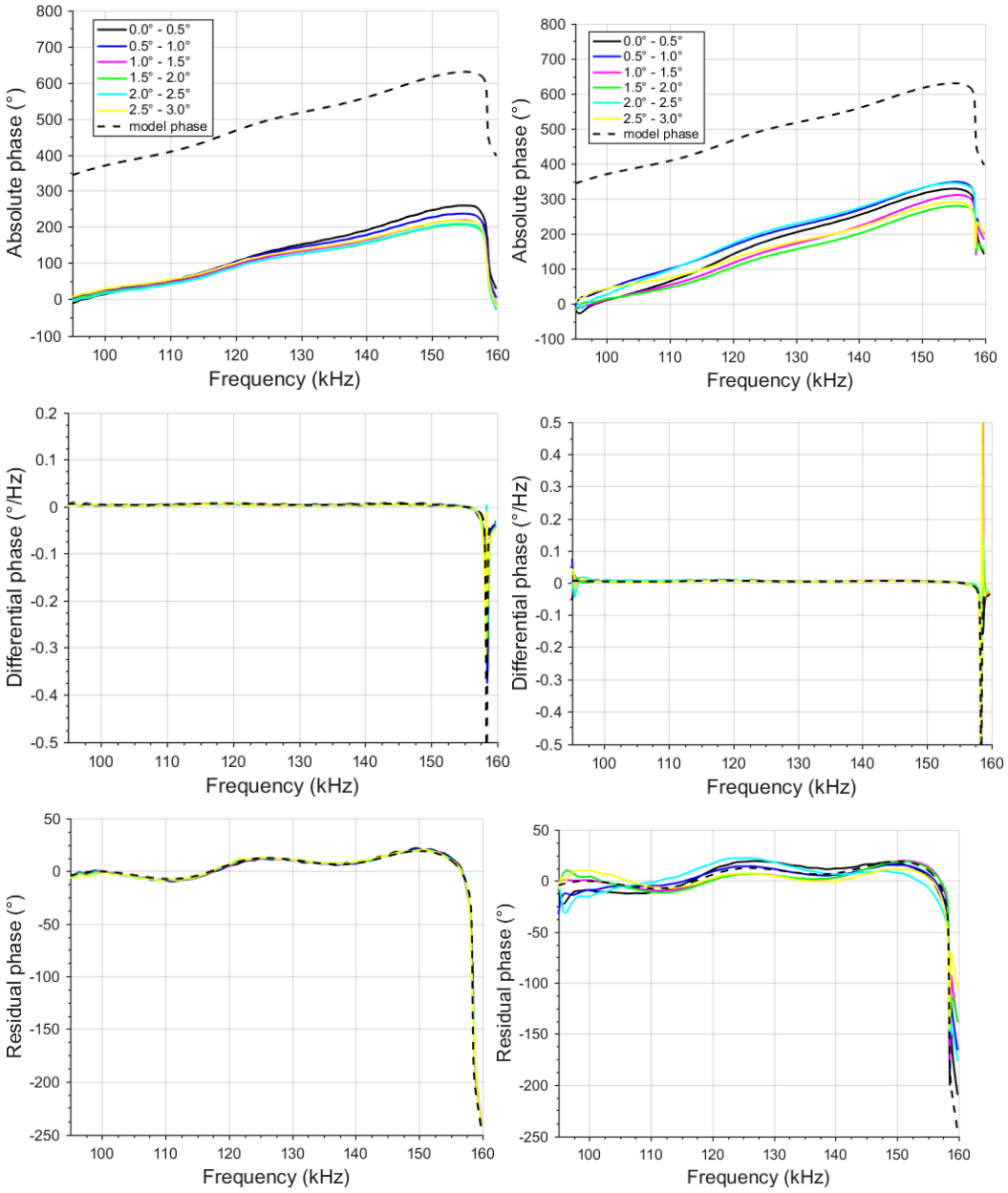

Figure 5.5: Bin wise averaged absolute (top), differential (middle) and residual phase (bottom) drawn to the frequency for the WC22 sphere for the fast (left) and slow (right) ramp waveforms. The off-axis angle varied from 0° and 3.0° as shown in the legend. A black dashed line shows the respective theoretical value in all plots.

Figure 5.5 illustrates the bin-wise averaged $\varphi_{bs}(f)$, $DP(f)$ and the $RP(f)$ computed for the WC22 sphere at the on-axis (red line) and off-axis positions for the fast and slow ramp. These were computed using $H(f,0)$ in Eq.(5.7) irrespective of the angle of the target.

The theoretically modelled value of each variable is drawn (black dashed line) for comparison. An offset of 360° occurred between the measured $\varphi_{bs}(f)$ and the theoretical value, for all angle bins and both the transmit pulse amplitude ramps. Taking the gradient of $\varphi_{bs}(f)$ removed the offsets, however; the high resonant spikes at 158.5 kHz dominated the $DP(f)$ curves and appeared to have different amplitudes in the measured and the modelled response. The $RP(f)$ provided a magnified depiction of the target phase, highlighting the variation over the entire frequency bandwidth. $RP(f)$ was more consistent for the fast ramp as compared to the slow, but both were in good agreement to the modelled value. The transmit pulse ramping and off-axis angle had a negligible effect on all three phase variables.

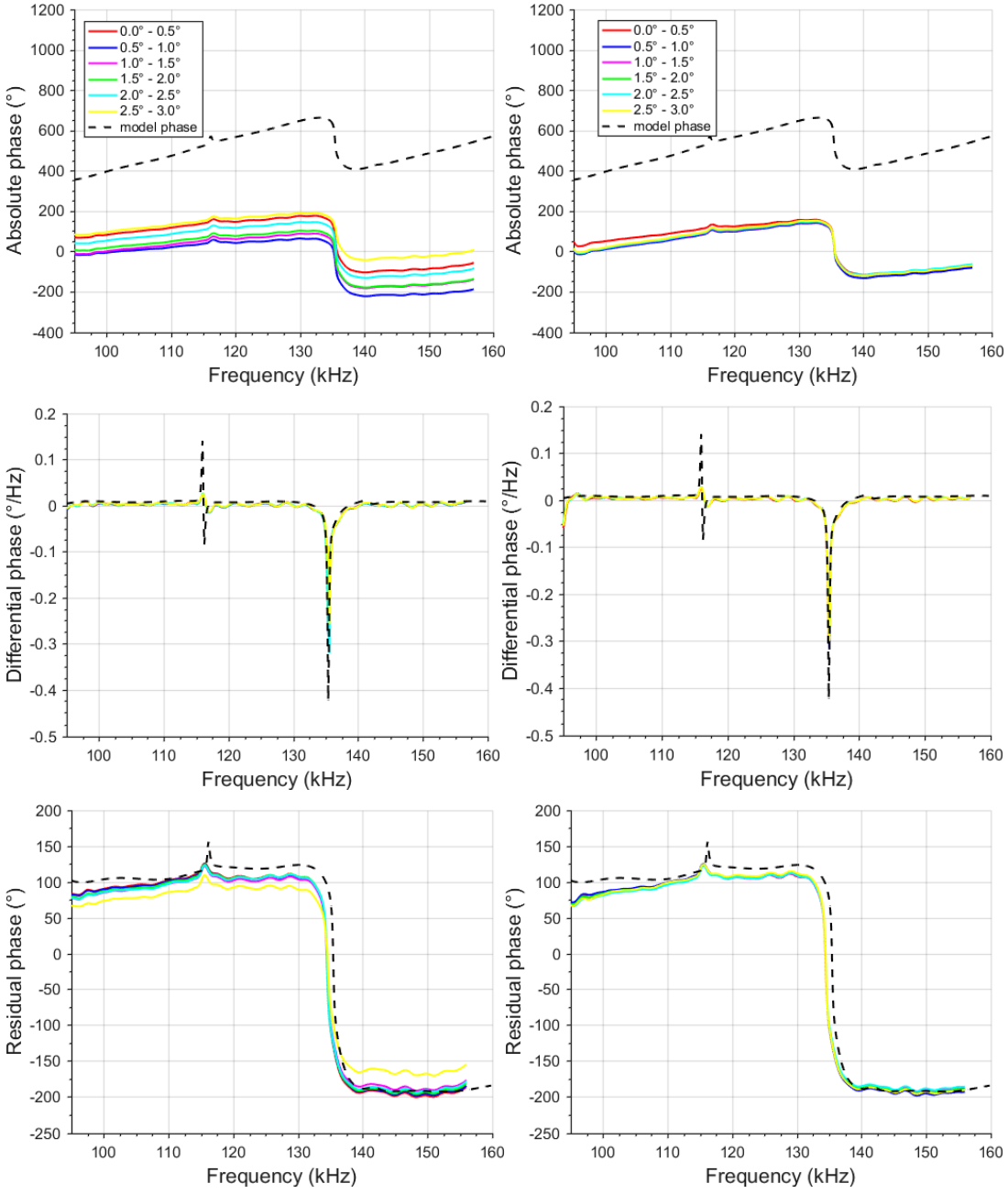

Figure 5.6: Bin wise averaged absolute (top), differential (middle) and residual phase (bottom) spectra for WC38 sphere, derived for the (left) fast and (right) slow ramp transmit signals. The off-axis angle varied from 0° to 3.0°, as shown in the legend. The black dashed line shows the respective theoretical response.

The frequency response of averaged $\varphi_{bs}(f)$, $DP(f)$ and $RP(f)$ for the WC38 sphere are shown in Figure 5.6. The frequency bandwidth was limited to 158.5 kHz to remove the artefact at 158.5 kHz due to the use of WC22 sphere as the reference target to compute $H(f,\theta)$. An offset of 360 ° and range-induced ramps appeared between $\varphi_{bs}(f)$ and $\varphi_{bs(model)}(f)$ in all bins for both transmission settings. Taking the gradient, removed

the offset resulting in the convergence of measured $DP(f)$ to the theoretical value. Nevertheless, the rapid phase change at the resonance leads to high amplitudes masking the response at other frequency regions. The $RP(f)$ clearly showed variations over the entire frequency range, even in the presence of two resonance peaks. The curves agreed with the theoretical values for all bins, although there was a small offset. Though $DP(f)$ removed the ramping it suffered from the resonance effects, which lead to high peaks as seen in the horizontal zoomed graph, in Figure 5.7.

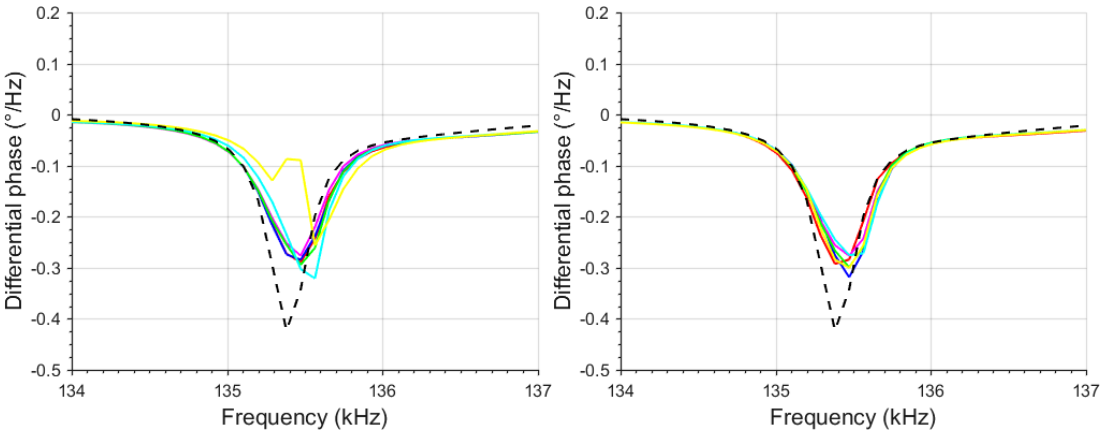

Figure 5.7: Horizontal zoomed plot of the differential phase of WC38 for the fast (left) and slow (right) ramp. A black dashed line plots the theoretical modelled value.

On the other hand, $RP(f)$ was consistent in delivering the actual phase change of the target between slowly changing (100 to 130 kHz) and rapid changing phase (130 and 140 kHz).

5.4 Discussion

5.4.1 Phase calibration

For the echosounder used in these tests (Simrad EK80, ES120-7CD), the transmit amplitude ramping (slow and fast) had almost no impact on the phase components of the system response function. This was unlike the amplitude component, where the ramping controls the magnitude, shape and the effective bandwidth. Further investigations with other transducers would be advisable to confirm this result.

In the study, the phase calibration was found to be independent of the transducer directivity. The frequency spectrum of $\varphi_{bs}(f)$, $DP(f)$ and $RP(f)$ were consistent for all the off-axis bin angles confirming their insensitivity to the sphere's position within the

acoustic beam. The result is in accordance with the theoretical radiation pattern of a plane circular transducer, the phase component of which is zero within the main lobe in the far-field region (Kinsler et al., 1999).

This insensitivity is significant because it implies that for phase measurements, an echosounder only needs to be calibrated on-axis, or at any other convenient off-axis angle within the main beam. The process of applying the calibration to the data is greatly simplified as the same calibration can be used for all target off-axis angles. This is completely different from the amplitude measurements, which require calibration of directivity compensation for each off-axis angle (Degnbol, 1988; MacLennan, & Svellingen, 1986). Further, it makes the phase independent of the beamwidth of the transducer and thus measurements would be unaffected even if there is a deviation in the effective beamwidth from the manufacturer provided value (Simmonds, 1984). Given this is the first set of results for one transducer type, the finding that the phase is independent of the position of the target cannot be assumed valid for all transducers, so would need further verification.

5.4.2 Phase variables

The study shows how different phase methods could be used to detect scatterer's information by using three variables ($\varphi_{bs}(f)$, $DP(f)$ and $RP(f)$). Indirect methods such as derivative of absolute phase (Mitri et al., 2008), gross phase shifts (Bolus et al., 1982) and phase difference (Atkins et al., 2007) have been proposed before. Murty, and Yegnanarayana (2006) computed linear prediction (LP) residual of speech signals to extract information about the excitation source. In fisheries, Barr, and Coombs (2005) used target strength as a function of the rate of phase change plots to demonstrate the phase which was validated through the resemblance of the modelled and measured work.

The measured $\varphi_{bs}(f)$ was qualitatively similar to the theoretically modelled value, but it was distorted by the presence of offsets and ramps. The ramps formed due to the range accumulation in the $\varphi_{bs}(f)$ masked the target features, making it difficult to use for target classification. Offsets by 360° have previously been reported for the dual-frequency transmission for the 84 mm and 40 mm spheres (Islas-Cital et al., 2011b). Inversion by 180° was found in $\varphi_{bs}(f)$ at resonant frequencies of the spheres with a processing window length of 0.4 m, as used for the amplitude calibration (Chapter 3). This was probably due to incomplete unwrapping caused by frequency-domain smoothing as a

result of the limited length of the windowed received signal (Cook et al., 2017; Flax et al., 1978). This inversion was averted by increasing the window length to 0.7 m, which reduced the effective smoothing of the scattering function with the frequency.

Differentiating the $\varphi_{bs}(f)$ with respect to frequency removed the range accumulation, but the sudden change in the phase due to the mechanical resonance of the spheres led to a high fluctuation in $DP(f)$ concealing the secondary structures at other frequencies.

The newly proposed variable, $RP(f)$ which was evaluated by subtracting the product of the frequency and the median of $DP(f)$ gave consistent results. Regardless of the presence of the noise, offsets and high resonant peaks, the spectra of $RP(f)$ showed the target's contribution across the entire frequency bandwidth. Minor variations were clearly visible, even in the immediate vicinity of the large phase changes that occur at resonances.

The phase calibration can be implemented using the standard calibration set up recommended for the broadband echosounder (Demer et al., 2015). Extraction and processing of phase variable would require retaining the recorded data in complex form.

5.4.3 Phase as a target classifier

Measurements from the test target, the WC38 sphere (Figure 5.6) supported the extraction of the phase of an unknown target and possible application towards remote characterisation. These results indicate that phase can play a role as a potential classifier in fisheries acoustic complementing $TS(f)$ from the target classification perspective. The selection of appropriate variables for interpretation of target phase could be important. Two key acoustic groups that inhabit the world's ocean are fluid-like and gas-bearing organisms (Stanton et al., 1996). The boundary condition of the gas bubbles forms a sharp hard and soft contrast surface resulting in a sudden fluctuation in the backscattered echo (Anderson, 1950; Love, 1978a), while the fluid-filled interface leads to slowly varying peaks and nulls (Stanton et al., 1996; Stanton, Chu, et al., 1998). Depending on the variation, a suitable phase index needs to be selected. While $RP(f)$ could be useful in case of high fluctuations to highlight minor changes, the $DP(f)$ can prove beneficial in regions with significant structures and a slowly varying phase. This would allow the target phase to be used as a supporting identifier towards remote classification. However, this would need further verification from surveys conducted in the open ocean.

The long processing window length of 0.7 m was possible during the experiment as the target sphere was the strongest scatterer in the water column. In the open ocean, it may be hard to achieve only one target within a window length of 0.7 m due to the presence of multiple organisms of similar strength in the water column. Similarly, in low signal to noise ratio environments noise spikes in $DP(f)$ can occur, which could interfere with the analysis, especially in case of a weak target with low echo strength. Extracting the phase of multiple targets within the window would be challenging with the current technique.

5.4.4 Future applications

As showed here, extracting phase can be easily integrated into the process of $TS(f)$ determination. With the equipment used here, the phase has an advantage of not requiring directivity compensation, as the system response is independent of the angle within the main lobe. The commercial availability of the broadband echosounder could play a significant role in the further development of this indicator. The computational and technological advancement has made working in complex domain easier and faster. Before the target phase is integrated into fisheries acoustics, it is important that the technique be tested with different transducers and a diverse range of parameters. Some other possible steps that could be undertaken are as follows:

1) Evaluate the impact of different pulse lengths, ranges and powers on the phase measurements.

2) Most existing numerical acoustic scattering codes work in the complex domain and therefore inherently calculate target phase. However, they need to be modified so that they could predict both amplitude and phase for comparison to the obtained measurements.

5.5 Conclusions

The chapter presented a complex transfer function-based approach to calibrate the commercially available Simrad EK80 broadband echosounder and extract the scatterer induced phase modification. Experimental implementation of the technique was demonstrated at two transmission settings, fast and slow ramp using two standard spheres. Two standard phase measures, absolute phase, $\varphi_{bs}(f)$ and differential phase, $DP(f)$ were compared with a new measure, residual phase, $RP(f)$ developed in this chapter. All the three variables if processed correctly (unwrapping, window length)

preserve the target information. $RP(f)$ was easier to interpret than $DP(f)$ and $\varphi_{bs}(f)$, as it was precise and consistent across the entire frequency bandwidth, irrespective of whether the phase varied rapidly or gradually.

Phase measurements were found to be independent of the transducer directivity pattern and the ramping of the transmitted signals. It was confirmed that phase conserves a scatter's information and could be integrated into acoustic remote sensing. No earlier publications known to the candidate have addressed phase extraction and calibration of broadband echosounders, particularly for different amplitude slope parameters and off-axis angles. In the next chapter, the developed method will be applied to open ocean conditions and possible application of phase towards in-situ target identification and classification.

Acknowledgements

The authors would like to thank Tim Ryan from CSIRO for invaluable support in setting up the experiment. Special thanks to Matt Sherlock from CSIRO for developing a customised platform to conduct the trials. The authors would like to extend sincere thanks to Lars Nonboe Anderson from Simrad for providing a set of Matlab codes for reading raw data. This study was undertaken as a part of the Great Australian Bight Research Program, a collaboration between BP, CSIRO, the South Australian Research and Development Institute (SARDI), the University of Adelaide, and Flinders University.

Chapter 6

Potential use of broadband acoustic methods for micronekton classification.

Broadband acoustic methods are an emerging technology with potential use in identification and classification of marine organisms. The application of broadband methods to scientific surveys of mesopelagic micronekton (animals of 2 - 20 cm length found at depths of 200 m to 1000 m) is described. The principles of the broadband system are briefly outlined with particular emphasis on its use for micronekton detection and identification employing the TS-frequency curve of single targets. The use of acoustic scattering models to determine characteristics of the marine organism such as size and material properties are also discussed.

As an example of the application of this technique, broadband echosounders mounted on a depth-profiling platform were used to collect high-frequency (55 - 160 kHz, some gaps in between) acoustic data from mesopelagic depths (up to 600 - 1000 m) of the Great Australian Bight region. Some example results from narrowband and broadband echosounders are compared. The resulting frequency-dependent target strength curves of selected targets enabled classification into different acoustic groups, demonstrating the significant advantage provided by the broadband system.

There is still a large gap between the obtainable acoustic classification and the ultimate aim of species-level classification, and to this end some limitations of broadband echosounder systems in identifying targets are discussed along with the use of video and still cameras to assist in the interpretation of acoustic data.

The text of this chapter is a reprint of the material as is appears in Verma, A**.**, Kloser, R. J., & Duncan, A. J, “Potential use of broadband acoustic methods for micronekton

classification". *Acoustics Australia, 45*(2), 353-361 (2017). The thesis author was the primary researcher and first author. The other authors listed in the publication supervised the research.

6.1 Introduction

Characterization and biomass estimates of micronekton (2 – 20 cm length animals including crustaceans, fish, squid and gelatinous organisms) inhabiting the mesopelagic region (200 m -1000 m), are primary inputs to ecosystem models to understand ecosystem function and make reliable forecasts for management (Benoit-Bird, & Au, 2001; Brodeur et al., 2005; Davison et al., 2015; Jason Phillips et al., 2009; Kloser et al., 2016; Lehodey et al., 2015; Lehodey et al., 2010; Robison et al., 1998; Scoulding et al., 2015). Sampling mesopelagic species is often challenging and logistically arduous, due to their depth, movement, and behaviour (diel vertical migration) (Béhagle et al., 2014; Brodeur et al., 2005; Davison et al., 2015; Jason Phillips et al., 2009; Lehodey et al., 2015; Lehodey et al., 2010). Echosounders are widely adopted for remote monitoring and quantification of the micronekton biomass (Kloser et al., 2009; MacLennan, & Holliday, 1996; Smith et al., 2013). Compared to other sampling methods, such as nets and optics, active acoustic methods discussed here are less intrusive and can sample at large temporal and spatial scales which can be post-processed afterwards (Gunderson, 1993; Horne, 2000; Koslow, 2009; Medwin, & Clay, 1998; Simmonds, & MacLennan, 2005).

Echosounders transmit acoustic signals and receive the acoustic signals backscattered by the targets. Acoustic signals backscattered by targets can be converted into useful qualitative and quantitative biological information (Horne, 2000; Simmonds, & MacLennan, 2005). The complex interaction of transmitted acoustic signals, environmental parameters and animal properties including shape, size, orientation, behaviour, and even the physiological state can affect the backscattered acoustic signal (Foote et al., 1987; Kloser et al., 2002; Misund, 1997; Stanton, Wiebe, et al., 1998). The Target Strength (TS, dB *re* 1m^2) is the lograthmic expression of the backscattering cross-section (σ_{bs}, m^2) of a target. TS represent the echo strength of a single point target and is often used to classify acoustic targets or groups of targets into biological units of species groups, numbers, size and biomass (Greenlaw, 1977; Holliday, 1972; Maclennan et al., 2002; Pieper et al., 1990; Zakharia et al., 1996). The TS can have a non-linear dependence on the transmitted signal frequency, animal size and composition (gas and fluid-filled) due to the complex diversity and depth distribution of species at mesopelagic depths. Hence TS measurements obtained at a single frequency, or a few discrete frequencies, may not allow the identification of the species present and therefore may not allow determinations of size and biomass. The broadband acoustic method

potentially offers considerable advancement over single frequency systems by providing a wider frequency bandwidth that is finely sampled in frequency (Chu, & Stanton, 1998; Demer et al., 2015; Horne, 2000; Jech et al., 2015; Kloser et al., 2011; Lavery et al., 2010; Stanton et al., 2012; Verma et al., 2016). Broadband acoustic data can be processed to provide the frequency dependence of the TS, allowing identification of targets based on the shape and amplitude of the curve (Demer, & Conti, 2005; Stanton et al., 1996; Stanton, Chu, et al., 1998; Stanton et al., 2000).

The sampling volume is the measure of the physical volume of water that contributes to the acoustic backscattered signal received by the transducer at a particular instant. The sampling volume is a function of equivalent beam angle, range, sound speed and pulse duration of the signal (Foote, 1991a; Medwin, & Clay, 1998). To measure the TS of an individual animal, it is necessary that it be the only target within the sampling volume of the acoustic system defined by the pulse resolution, the angular beamwidth and the range (Simmonds, & MacLennan, 2005).

$$Vol = \frac{c\tau}{2} \times \pi(r \times \theta(\omega))^2 \qquad (6.1)$$

Where ω (Hz) the angular frequency ($2\pi f$), c is is the sound speed (ms^{-1}), τ is the pulse duration (s), and r is the range (m) from the echosounder. $\frac{c\tau}{2}$ in Eq. (6.1) is the pulse length of the signal (m).

For a circular transducer, the frequency-dependent beamwidth $\theta(\omega)$ radians, is defined as the angle between the -3 dB differences in intensity on both sides of the beam of the transducer (Foote, 1991a; Lee, & Stanton, 2015). In case of a narrowband transducer, the range of frequencies emitted is very small, and the beamwidth is constant. Due to variation in the beamwidth with frequency, the sampling volume of a broadband transducer is different for different transmitted frequencies. To extract useful information and maximize the SNR output, broadband scattered signals are pulse compressed by applying a proper matched filter (Chu, & Stanton, 1998; Turin, 1960).

The pulse duration of a matched filtered signal is given by Eq. (6.2).

$$\tau \approx \frac{1}{W} \qquad (6.2)$$

where W is the bandwidth of the signal (Burdic, 1991).

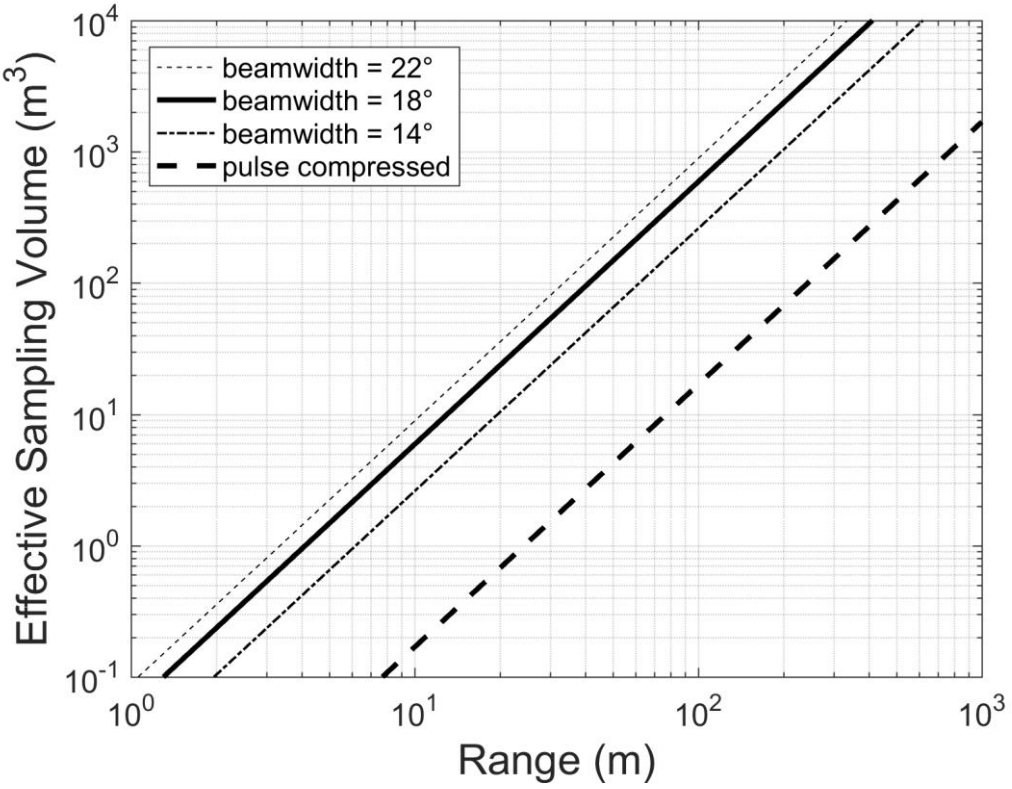

Figure 6.1: The plot of sampling volume versus range for transducer beamwidths of 14°, 18° and 22° without pulse compressions and a beamwidth of 18° with pulse compression. The bold black curve is the sampling volume of the narrowband transducer with fixed beamwidth (18°). The frequency bandwidth is 55 kHz to 90 kHz. The uncompressed pulse duration is 1 ms, and the compressed pulse length is 0.0214 m. The bold dashed line is obtained by applying pulse compression to the broadband signal.

Pulse resolution for pulse compressed signals may be longer for off-axis targets due to change with the frequency spectrum of the transmit signal with off-axis angle that results from the frequency dependent transducer beampattern. Matched filtering of broadband signals combines all frequencies, which introduces considerable complexity when considering the pulse length for off-axis targets, so a full discussion of this effect is beyond the scope of this paper. For this paper, the sampling volume after pulse compression has been approximated by using the beamwidth at the central frequency and the pulse resolution for on-axis targets. Unlike narrowband where sampling volume is controlled by pulse duration, the sampling volume of a broadband system is controlled by the bandwidth and the wider the bandwidth the better is the spatial resolution after matched filtering.

The variability in sampling volume with range, for different beamwidths of a circular

transducer (SIMRAD 70 kHz, bandwidth 55 – 90 kHz) and a pulse duration of 1 ms is drawn in Figure 6.1 (log scale). The curves in the figure illustrate the change in the sampling volume of a broadband system at different beamwidths including the pulse compressed and narrowband beamwidth values. The beamwidth was 18° at the center frequency, 14° at the highest frequency and 22° at the lowest frequency for a broadband sonar system. For the narrowband echosounder and pulse-compressed broadband signals the nominal center frequency beamwidth (18°) is considered. Pulse compression of signals reduced the pulse length from 0.75 m to 0.03 m. The sampling volume increases quadratically with the product of range and beamwidth. Pulse compression of a signal significantly reduces the sampling volume, hence improving the likelihood of being able to isolate a single target and therefore carry out TS measurements (Chu, & Stanton, 1998).

Single target detection using a ship mounted system is challenging due to large sampling volume at a higher range from the sonar system. Lowered platforms are often used to allow sampling targets at shorter range, and hence smaller sampling volume and absorption loss, leading to better single target detection. Recent deployments of lowered combined acoustic and optical platforms have shown positive results in estimating the density and size distribution of the deep scattering layer (Kloser, 1996; Kloser et al., 2016; Kloser et al., 2009). An extension of that work is to upgrade the single frequency echosounders used in a profiling system with broadband echosounders.

The Great Australian Bight Research Program (GABRP), is a joint initiative of industries and research institutions to map a part of the deep water habitat of the region. One of its objectives is to monitor, identify, classify and quantify the mesopelagic habitat of the Great Australian Bight (GAB) region consisting primarily of mesopelagic crustaceans, squids, fishes, and gelatinous organisms (e.g. siphonophores) (Anthony et al., 1994; GABRP, 2013). The micronekton distribution and abundance in the GAB are believed to influence the local ecological features impacting the population dynamics of apex predators in the region (Rogers et al., 2013). As a part of the GABRP, a customized depth profiling platform fitted with two broadband transducers was used to sample the mesopelagic zone at depths to 1000 m. This paper highlights some results from the initial trials of the broadband system demonstrating its capabilities and discusses its future application. The potential use of the broadband acoustic system to identify and classify targets is exhibited through characteristic TS-frequency curves of some selected targets. The obtained TS-frequency spectra are compared with the output of relevant

acoustic scattering models to anticipate the acoustic features of the targets.

6.2 Material and Methods

As a part of the GABRP, mesopelagic regions in the Great Australian Bight were acoustically sampled from 29 November to 22 December 2015 on the *RV Investigator* operated by the Marine National Facility [51]. The broadband acoustic system (SIMRAD EK80) consisted of two split-beam circular transducers; SIMRAD 70 kHz (T_L), and SIMRAD 120 kHz (T_H), fitted to a custom designed depth profiling platform, the Instrumented Corer Platform (ICP) (Sherlock et al., 2014; Simrad, 2016). The ICP was deployed to maximum depths of 600 m to 1000 m at selected locations, and broadband acoustic data were recorded. Transducer T_L and T_H transmitted waveforms consisting of linear frequency sweeps across frequency ranges of 55 – 90 kHz and 95 – 160 kHz, with beamwidths of 18° and 7°at nominal center frequencies of 70 kHz and 123.2 kHz respectively. The uncompressed pulse duration of T_L and T_H were 0.512 ms and 0.256 ms. Multifrequency acoustic datasets were collected at six distinct frequencies (18, 38, 70 and 120 and 200 and 330 kHz) using a SIMRAD EK60 fitted on the lowered vessel keel for the whole survey period.

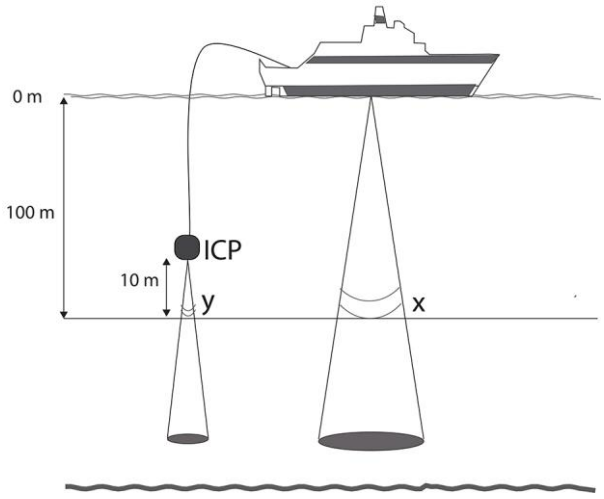

Figure 6.2: An illustration of the acoustic ensonified volume by a vessel mounted echosounder, and a broadband sonar system mounted on a depth-profiling platform (ICP). x (m^3) represent the sampling volume of the narrowband sonar at 100 m whereas y (m^3) is the sampling volume of the broadband sonar at the same depth. Using a lowered depth probe facilitates smaller and constant sampling volume at all depths.

Results from 70 kHz narrowband echosounder have been included to compare with the results from broadband echosounder system. The pulse duration for 70 kHz narrowband

transducer was 2.048 ms, and the beamwidth was 6.6°/6.4° (major axis/minor axis). A graphic representation of the whole setup is shown in Figure 6.2 Using a depth-profiling system (ICP) enabled short-range acoustic images to be obtained from the deeper ocean at a constant sampling volume which is not the case with vessel mounted transducers (Lavery et al., 2010).

The preliminary analysis of acoustic datasets were carried using Matlab codes provided by Simrad and Echoview (Echoview, 2017; Simrad, 2016). Specific Matlab codes were developed to process broadband acoustic data to obtain the range, time, target strength (*TS*) and phase angles (Verma et al., 2016). Pulsed compressed echograms were generated after appropriate compensation for the absorption loss and two way spreading loss ($TVG = 40 \log R$) (Francois, & Garrison, 1982). The TS frequency curve of selected targets were extracted using the system response of respective off-axis position. The obtained curves were further fitted with output of relevant acoustic scattering model (Distorted Wave Born Approximation (DWBA) and resonant scattering) to predict the probable features. Both broadband and narrowband echosounders were calibrated with the standard target calibration method (Demer et al., 2015; Stanton, & Chu, 2008). A 38.1 mm tungsten carbide calibration sphere with 6% cobalt (WC38) was suspended below the transducers for the calibration. The broadband sonar systems were also calibrated for the depth dependent variability and frequency dependent beamwidth sensitivity. Results indicated the consistent performance of the broadband system with depth and off-axis angles for targets within the beamwidth of both transducers.

6.3 Narrowband and broadband acoustic images

High-resolution echograms of the mesopelagic habitat were generated using acoustic data recorded by the vessel mounted narrowband echosounder and the broadband echosounder mounted on the ICP. The echogram in Figure 6.3 (top)is the volume backscattering (S_v, dB *re* 1m^{-1}) of a section of the water column extending from 50 m to 150 m depth recorded by the narrowband echosounder at 70 kHz frequency. Scatterers distributed between 50 – 100 m have high volume backscattering intensity as compared to ones below 100 m. A long pulse length (0.75 m), a large sampling volume of 591.0 m^3 at 100 m range from the vessel and high target density results in low spatial resolution. The area within the red lines in the echogram corresponds to the region mapped by the broadband sonar system. (Note: the regions do not overlap). Although both measurements were taken at the same time there, was a spatial separation of 10 m

between the two recordings.

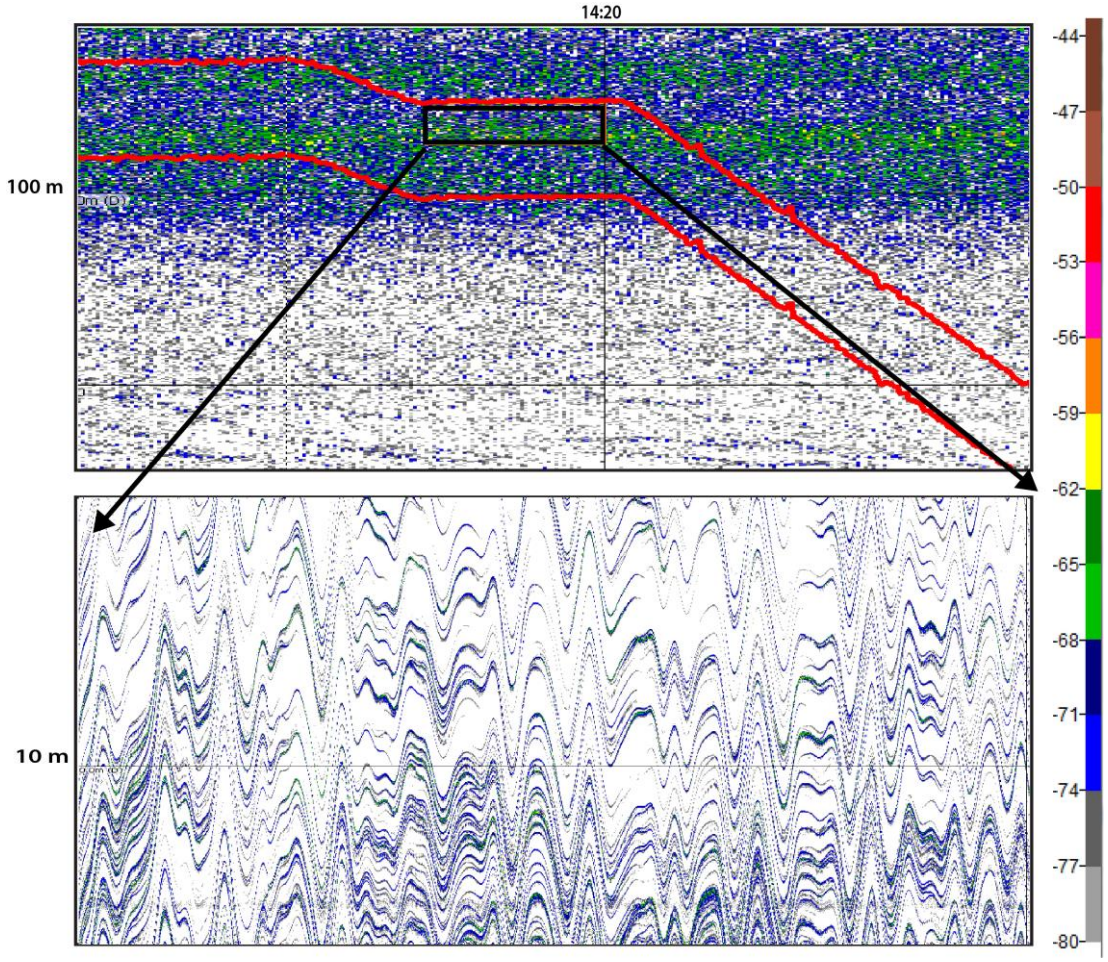

Figure 6.3: Echogram of the volume backscattering measured by 70 kHz narrowband system mounted on the vessel. The area within the red lines corresponds to the region sampled by the broadband sonar system (EK80). b) is the pulse compressed TS obtained from T_L transducer (55 – 90 kHz), corresponding to the region bounded by a black rectangle in the narrowband echogram.

A pulse compressed TS echogram using broadband signals for a section of echogram (black rectangle) is drawn in Figure 6.3 (bottom). In the broadband echogram, individual targets are visible. Using a depth profiling platform had advantages of reduced range and constant sampling volume even at larger depths. (Note: that the apparent synchronous vertical movement of the targets in Figure 6.3 (bottom) is an artefact of the motion of the ICP caused by its taught-cable connection to the ship).Recording just above the biota at a lower range (10 m) in the second echogram and small pulse length (0.03 m) after pulse compression leads to decreased sampling volume of (0.23 m^3) and hence improved possibility of single target detection. Also, the reduced range leads to

less absorption and transmission loss, providing a high signal to noise ratio (SNR) compared to the narrowband system (Stanton, & Chu, 2008).

6.4 Broadband acoustic spectra and target identification

Determining a target's characteristic features and physical nature from echograms or TS measurements at a few distinct frequencies can be a challenge as targets with the same echo intensity could arise from entirely different groups of marine organisms (Benfield et al., 2003). Using frequency-modulated broadband signals enables the extraction of spectral characteristics of the backscattered signal, which can greatly aid in target identification. To illustrate this, the TS frequency curves of two single targets measured at the same depth, ~600 m during an ICP deployment were constructed and subsequently fitted with the predictions of suitable numerical scattering models.

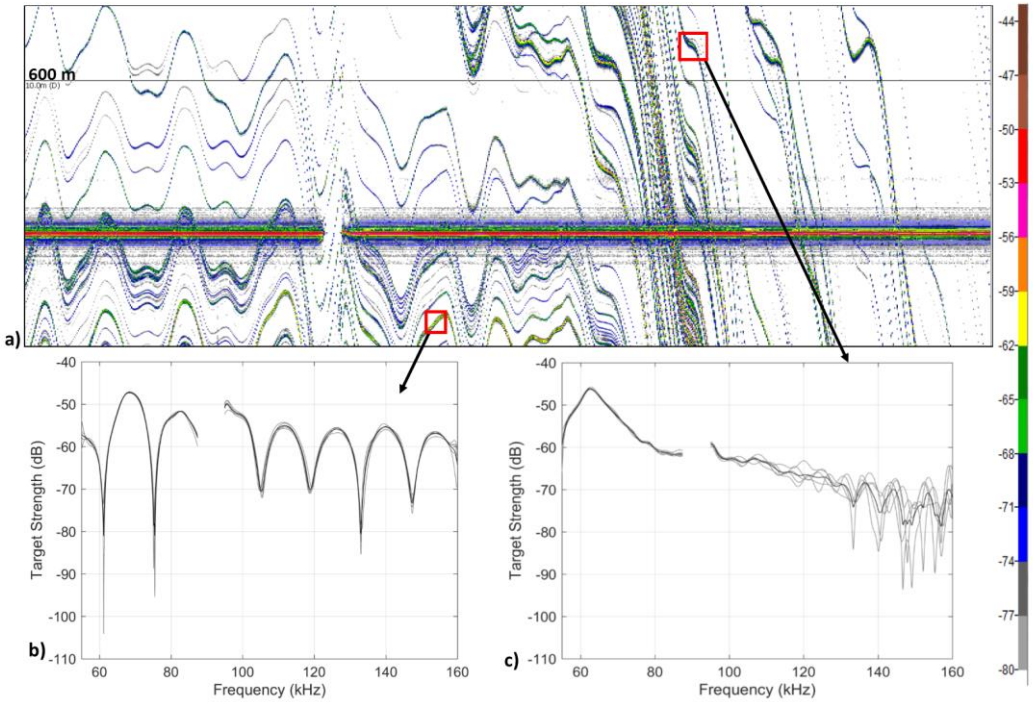

Figure 6.4 Two different targets in a pulse compressed echogram and their acoustic signatures. a) location of two single targets (within red rectangle) identified in the pulse compressed TS echogram measured by the transducer T_L (55 – 90 kHz) at ~600 m depth. The region of high echo level at ~14 m is due to the calibration sphere suspended below the transducers. b) acoustic signature of a scatterer at ~600 m depth and 15 m range with TS oscillating around -55 dB. c) TS versus frequency plot of a target at 8 m range indicates a gas enclosure resonant at 62 kHz. The averaged TS value of all pings are plotted as a black line in both b) and c).

To obtain these results, pulse compressed echograms generated using broadband datasets recorded by both T_L and T_H transducers were visually inspected for targets to confirm the presence of only one target in the volume defined by the transducer's centre-frequency beamwidth, the uncompressed pulse length and the target's range. The target strength versus frequency curves was then obtained by a method described in detail in a recently submitted publication by the authors that conceptually involves dividing the spectrum of the received signal by the spectrum of the signal incident on the target. Figure 6.4 (a) is a pulse compressed echogram generated using the data recorded by transducer T_L across 55 – 90 kHz at ~600 m depth. The region of high echo level (~50 dB) originates from the calibration sphere (WC38) suspended below the transducers. Two single targets enclosed in red rectangles in the echogram were selected, and their TS-frequency curves are drawn in Figure 6.4 (b) and (c).

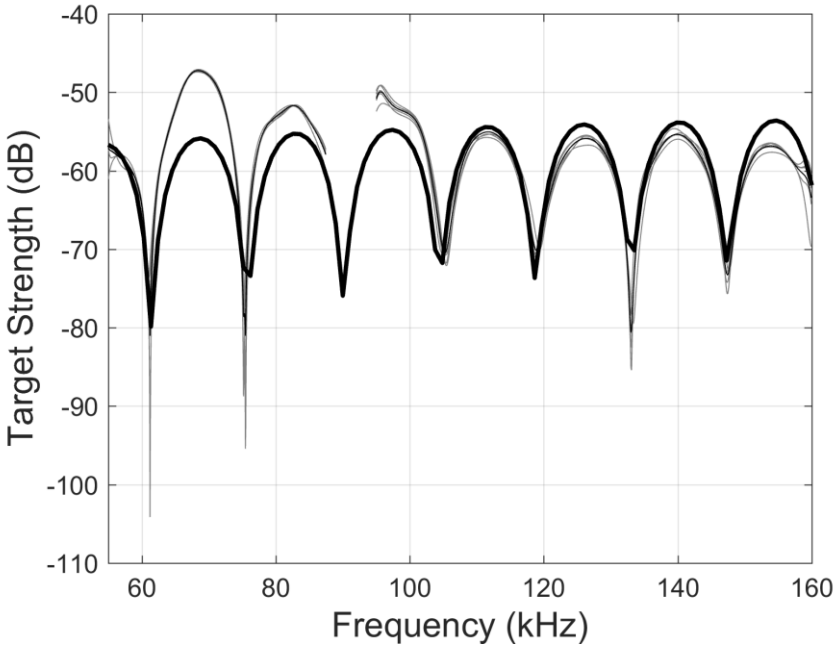

Figure 6.5: TS-frequency spectrum of the first target. The grey lines are the TS value of individual pings, the thin black line is the averaged TS, and the thick black line represents the predicted TS from the DWBA model, based on material properties of a squid (length = 13.1 cm, density ratio = 1.01 and sound speed contrasts = 1.01).

A small gap between 90 – 95 kHz in TS frequency curves is due to the frequency gap between T_L and T_H transducers. The TS-frequency spectra of the first target illustrated in Figure 6.4 (b) highlight high TS amplitude (-55 dB), recurring oscillations with peaks and nulls at a constant frequency interval (10 kHz) across the entire frequency band. In

contrast, the TS-frequency curve of the second target exhibits a single peak,-46.14 dB at 62.7 kHz (Figure 6.4 (c)).

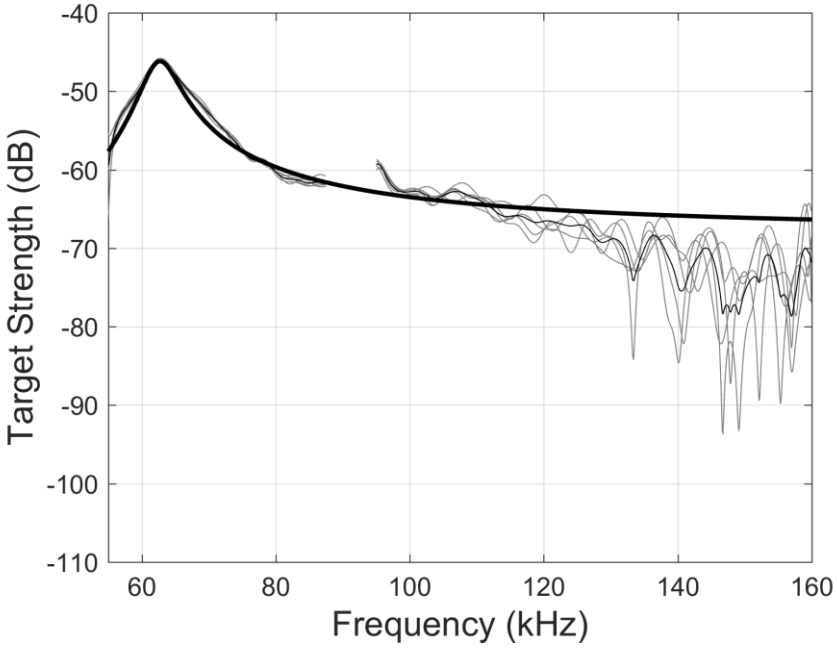

Figure 6.6: Modeled resonant scattering TS curve as a function of frequency of a target at 600 m depth with -46.14 dB TS at the resonant frequency of 62.7 kHz. TS value of individual pings (grey), averaged TS (black) and modeled TS (bold black bold) are shown in the figure.

To obtain insight into the characteristics of the two targets, their TS curves were fitted with the prediction of appropriate numerical models, assuming the targets could be modelled as simple geometrical shapes with fixed material properties. The TS spectrum of the first target is typical of a weakly scattering fluid-filled organism though the TS has a higher amplitude (-55 dB) than most fluid-filled animal (Chu et al., 1993; Demer, & Conti, 2004; Jech et al., 2015; Stanton, & Chu, 2000; Stanton et al., 1996). The TS amplitude and shape of the first scatterer (Figure 6.4 (b)) match closely to squid signatures given in Jones et al. (2009). The obtained TS spectrum was manually fitted with the predicted output from a model based on the Distorted Wave Born Approximation (DWBA) developed for fluid-filled animals (Figure 6.5) (Stanton et al., 1996; Stanton, Chu, et al., 1998). The predicted TS (bold black line) was obtained assuming the target to be a squid, 13.2 cm in length, with an aspect ratio of 2.5, and sound speed and density contrasts of 1.01. The predicted TS is a reasonable fit to the data for nulls and peaks positions and TS amplitude in the high-frequency region. However, in the absence of proper ground-truthing, the species of the organism cannot be uniquely determined, as

the possibility of other organisms or parameters providing an equally good or better fit cannot be ruled out.

The spectra of the second target (Figure 6.4 (c) exhibited a resonant scattering often linked to gas-enclosed organisms (Love, 1978b; Stanton, & Chu, 2010). This is confirmed by fitting the TS curves with the prediction of a resonant scattering model (Figure 6.6) as in Kloser et al. (2002). The model assumes that the target acts as a gas-filled spherical bubble at the target's measured depth, with a volume and damping factor fitted to the measured TS (Andreeva, 1974; Weston, 1967; Ye, 1997a). The fitted values of these parameters correspond to a bubble radius of 0.4 mm and a resonance quality factor, Q, of 10. This typical resonant scattering curve could either be attributed to micronekton with a gas enclosure of radius 0.4 mm or slightly larger or something of larger volume enclosed within a more substantial membrane, muscle layer etc. that itself has significant elasticity (Baik, 2013; Love, 1978b).

Although these results illustrate the insights that can be obtained using such a system they also highlight that definitively identifying targets in the absence of a visual verification remains a challenge due to the complexities of the scattering mechanism.

6.5 Discussion and Conclusion

This study highlights the advantages of a depth-profiling broadband sonar system over vessel mounted narrowband systems for monitoring of mesopelagic habitat. A brief review of principles of broadband acoustics is presented with the potential application to target detection and identification using TS-frequency curves of selected targets. Single target analyses using conventional vessel mounted narrowband echosounders are often challenging due to large sampling volume at a longer range, low spatial resolution, and the availability of a backscattered signal only at certain discrete frequencies [30]. Using a broadband sonar system on a depth profiling platform allowed high spatial resolution data to be obtained over a wide range of depths, and also the characterization of individual targets through measurement of their TS-frequency curves. Fitting, numerical scattering models to these TS-frequency curves provides a means of relating them to the physical characteristics of the scatterer, but there is much more still to be done in this regard. Measured broadband spectra of organisms may change due to size, shape, orientation or depth (in the case of gas-filled cavities), and therefore may not be unique to a species or size class of a species. This introduces uncertainties in using geometry-based acoustic scattering models to infer the species and size of the targets from the

measured values in the absence of appropriate visual verification.

Through comparison with the ship mounted narrowband system in Section 3, we have shown that pulse compressed broadband signals provide an enhanced resolution on the vertical scale allowing smaller micronekton to be acoustically imaged. Mounting the broadband echosounder on a depth-profiling platform enabled sampling mesopelagic depths at a finer spatial scale and constant smaller sampling volume. Recording targets at a small range may also enable extraction of acoustic properties of individual organisms which will aid in the identification and classification of other similar organisms. This will also assist in the interpretation of vessel-based volume scattering measurements for species composition and density (Kloser et al., 2009).

The disadvantage of a lowered platform include that it is only possible to make measurements when the vessel is stationary, and it could potentially modify the behaviour and response of organisms more than a vessel mounted system, leading to biased measurements (Stanton, & Chu, 2010). The former problem can be alleviated by using a variable depth towed system, but such a system would sample a smaller proportion of the water column at any one time than typical vessel mounted systems.

In theory, broadband systems have smaller sampling volumes and potentially better noise performance than narrowband systems. However, given the current transducer technology with frequency-dependent beamwidth, achieving these are practically challenging. Further, in a broadband sonar system, changes in the position of a target within the frequency dependent beam pattern induces variability to the TS measurements. Hence, removal of the beam pattern effect is critical to improving the accuracy of measurements (Ehrenberg, 1979; Stanton, 2012). Measurements from both the targets Figure 6.4 (b) and (c)) were compensated for their position using a method developed by the authors (paper in review).

It remains a challenge to incorporate the broadband technology into methods that quantify and characterise the distribution and abundance of key species and quantify their size and biomass (Godø et al., 2014). An integrated set-up simultaneously using acoustics, optics, and net sensors could provide the visual ground truthing, of the sampled biota(Kloser et al., 2016; Kloser et al., 2009). The Profiling Lagrangian Acoustical Optical System (PLAOS) allows active acoustics instruments to be merged with high-resolution optical stereotypes and video cameras for use in qualitative and quantitative analysis [69]. Future work will be to integrate the broadband acoustic system

with the optical still images and video camera of Kloser et al. (2016). This would enable validated acoustic measurements providing added information for interpreting broadband measurements.

Acknowledgements

This study is being undertaken as part of the Great Australian Bight Research Program, a collaboration between BP, CSIRO, the South Australian Research and Development Institute (SARDI), the University of Adelaide, and Flinders University. The Program aims to provide a whole-of-system understanding of the environment, economic and social values of the region; providing an information source for all to use. The authors would like to thank in particular Tim Ryan and Lars Nonboe Andersen for the software support and Matt Sherlock for configuring broadband sonar systems on the ICP. Thanks to Dezhang Chu Woods Hole at National Oceanic and Atmospheric Administration for providing the Distorted Wave Born Approximation model for fluid filled animals. Special thanks to the whole team of Marine National Facility (MNF) for managing and assisting the deployments.

Chapter 7

In situ Target Strength and Target Phase Measurements of Optically Verified Micronekton

Broadband echosounders complemented with optical sensors (video and still cameras) were used to investigate live micronekton in the mesopelagic region (~200 – 1000 m) of the Southern Ocean. To verify the presence of an acoustically sampled organisms, a technique was developed to transform a scatterer's position in the pulse-compressed echogram to its position in the concurrent photograph taken by the camera. The acoustic signature (frequency response of the target strength, $TS(f)$ and the residual phase, $RP(f)$) of several optically verified micronekton were used to classify them into acoustic groups thereby demonstrating the classification capacity of a broadband acoustic system. Further, to confirm the utility of $RP(f)$ in acoustic analysis, the acoustic signature of three different targets exhibiting resonant scattering were inverted using a numerical scattering model to infer its physical characteristics. The theoretically predicted $TS(f)$ and $RP(f)$ of the modelled targets matched the measured $TS(f)$ and $RP(f)$ values for all pings confirming the possibility of using $RP(f)$ as an acoustic classification metric. Further work is required to substantiate the technique by undertaking measurements from different organisms and matching them to the output of appropriate numerical scattering models. A detailed description of the system configuration, algorithm, and the processing is provided along with the discussion of advantages and challenges.

7.1 Introduction

The mesopelagic region of the Southern Ocean forms a habitat to many species of micronekton (fishes, cephalopods and crustaceans, and gelatinous organisms (Koslow et al., 1997; Williams et al., 2001; Williams, & Koslow, 1997; Young et al., 1996). These organisms are known to play a central part in the ocean's food web dynamics, linking the lower level zooplankton to the top-level pelagic predators (Brodeur et al., 1999; Sinclair et al., 1999). An insight into their distribution patterns, biomass abundance and ecological processes can provide valuable inputs for their sustainable conservation management (Handegard et al., 2013; Lehodey et al., 2010). The primary sampling tools to do this have been acoustic, net and optical samplers. A significant need is the improvement of these tools for broad-scale monitoring and in particular, the use and interpretation of new acoustic sensing methods (Verma et al., 2016).

The implementation of ecosystem-based management system strategies requires an increased focus on the quantification of micronekton biomass and more species-level information. Broadband acoustic scattering techniques are being used to investigate the individual and community level structures of these organisms (Au, & Benoit-Bird, 2008; Bassett et al., 2017; Verma et al., 2017). The extraction of the spectral response of backscattered energy over a wide frequency range and increased spatial-resolution from the signal pulse compression improves the detection of individual scatterers' (fish, squid or crustacean) (Lavery et al., 2010; Stanton, & Chu, 2010).

The frequency response of the target strength, $TS(f)$, (dB re 1 m^2) is a critical parameter for remote detection of individually resolvable targets as it depends on the organism's shape, size, orientation, behaviour, and even physiological condition (Foote, 1980; Martin Traykovski et al., 1998; Ona, 1990b; Simmonds, & MacLennan, 2005). In situ, $TS(f)$ remains one of the most effective ways to characterise an organism despite numerous challenges (Ehrenberg, 1983; Foote, 1991c). Nonetheless, obtaining the precise $TS(f)$ of individual scatterers' from a hull-mounted echosounder can be challenging due to the long sampling range and large acoustic sampling volume (Foote, 1991a). An alternative solution to using near-surface mounted transducers is to lower the transducer into the deep regions of the ocean using various hardware platforms (Kloser et al., 2002). A shorter range from the transducer minimises propagation loss, decreases the acoustic volume and increase the chances of sampling a single organism while minimising interpretation of multiple organisms as a single target (Soule et al.,

1995).

The target induced phase distortion in the backscattered signal has the potential to be used as an additional acoustic classifier for detection and identification purposes (Barr, & Coombs, 2005; Braithwaite, 1973). Unlike narrowband echosounders, a broadband echosounder conserves the signal in its complex form (Medwin, & Clay, 1998) from which the target phase, $\varphi_{bs}\,(f)$ (°) can be extracted as a function of frequency (shown in Chapter 5). However, uncertainties due to the wrapping (Al-Nashi, 1989) and the range accumulations (Lyon, 1984) in the signal phase causes challenges in obtaining meaningful information. As a result, several methods are used to minimise the propagation and range effects. Consequently, despite several controlled studies in the last few decades, there is a lack of application of the target phase to detection and classification of marine organisms.

In Chapter 5, two variables, differential phase, $DP(f), (DP(f) = \frac{d(\varphi_{bs}\,(f)}{df})$ (°/kHz) and residual phase, $RP(f)$ $(RP(f) = \varphi_{bs}\,(f) - f \times median\big(DP(f)\big)$ (°) were used to visualise the implicit target induced phase distortion in the signal. $DP(f)$ was found prone to the effect of noise, and thus, the target's specific features were masked. $RP(f)$ provided useful information, even when the signal to noise ratio was low.

For accurate interpretation, it is important that targets detected with echosounders are identified by using complementary techniques (McClatchie et al., 2000). Several methods such as nets (Didrikas, & Hansson, 2004; Ryan et al., 2009), or optical sensors (Kloser et al., 2016; Sawada et al., 2004) have been used, all with various limitations and advantages. The main issue with net capture is that the catch may not be representative of the acoustically sensed organism (Kloser et al., 1997; Koslow et al., 1995). Nets sample a large volume and capture a high diversity of organisms in the mesopelagic region. Allocation of the many net species to the independent acoustic system is not possible. Additionally, most gelatinous zooplanktons are severely damaged beyond recognition (in particular the gas-bearing siphonophores). To provide in situ visual verification, a synchronised camera is an attractive option as it can produce exact three-dimensional information of the acoustically sampled target (species, size, texture, and orientation) (Jaffe et al., 1998). On the downside, the use of a camera is limited by the small sampled volume, multiple targets in the optical field (Barange et al., 1996) and possible modification in the behaviour of organism due to the use of light (Sawada et al., 2009). In fisheries and ecosystem research, the use of complementary acoustic-optics

sensors is often used to provide visual verification of acoustic ensonified targets (Johnson et al., 1956; Kloser et al., 2016).

By utilising visually verified spectra the potential corruption of the in situ, $TS(f)$ and $\varphi_{bs}\ (f)$ by microbubbles, microstructure, or other small organisms in the pulse resolution volume can be minimised (Henderson, & Horne, 2007). Due to optical range resolution (<10 m) and the need for artificial light, the behaviour of organisms is often modified. Therefore it is not often possible to directly use $TS(f)$ and $\varphi_{bs}\ (f)$ of the observed spectra without understanding how behaviour induced tilt orientations influence $TS(f)$ and $\varphi_{bs}\ (f)$.

Acoustic scattering models are often developed and used to assist in the interpretation of in-situ data and its extrapolation. In a measurement-model approach, the experimental acoustic backscatter is matched to the output of the theoretical numerical acoustic scattering models (Jech et al., 2015). In situ, $TS(f)$ can be adequately modelled using the morphological and material information of the acoustically sampled scatterer. Using the known properties, these models approximate an organism as a simple or complex geometric shape, with homogenous or heterogeneous material properties and simulate the $TS(f)$ (Anderson, 1950; Love, 1978b; Reeder et al., 2004; Stanton, 1990; Stanton et al., 1993). For a given model, the parameters such as the size, shape and material properties are varied to find a match with the measured $TS(f)$. Though these models predict the complex backscattering amplitude, $F_{bs}(f)$ (m) only the absolute part or the amplitude ($|F_{bs}(f)|$) is usually used in the analysis (Clay, & Horne, 1994; Horne, 2000; Medwin, & Clay, 1998). By expanding these models to predict $RP(f)$, the capability of present models towards identification could be improved, especially when attempting to distinguish between targets with similar $TS(f)$. This would enable a two-parameter classification where both amplitude and phase are matched for identification.

The study aims to obtain $TS(f)$ and $RP(f)$ responses of optically verified live micronekton from the mesopelagic region. The question of whether $RP(f)$ can be used as a reliable acoustic classifier is also addressed. For this study, synchronised acoustic and optics data collected from the Profiling Langrangian Acoustic Optics System, (PLAOS), platform deployed in the Southern Ocean were used. The PLAOS has been designed and developed by the Marine National Facility, CSIRO, in Hobart, to collect high-resolution integrated acoustic-and optics data from the deep ocean at depths to ~1000 m (Marouchos et al., 2016). A method to visualise a target detected on the echogram on

the corresponding photo was developed. The acoustic signatures were drawn. The empirical values of different scatterers exhibiting resonance were matched to the output of an optimal numerical scattering model.

The theoretical development, PLAOS configuration and processing is detailed in section 7.2. The results are presented in section 7.3. The strengths, limitations of the technique and the future direction are discussed in section 7.4, followed by the conclusion in section 7.5.

7.2 Method

7.2.1 Data collection

As part of a Southern Ocean Time Series Voyage onboard Australians' Marine National Facility vessel, *RV Investigator* a Profiling Lagrangian Acoustic Optical System (PLAOS) was deployed to characterise the mesopelagic micronekton (Marouchos et al., 2016). For this work, we review data from the PLAOS (Figure 7.1) deployed to a mesopelagic depth of 1000 m at S 45.938°, E 142.060° from 08:50 to 10:13 UTC on the 23rd March 2017. This corresponds to local night time (19:20 to 20.40 hrs) as it captures the vertical diel migration of these animals to epipelagic (0 to 200 m) depths.

Figure 7.1: The PLAOS ready to be deployed. The platform carried two broadband and a narrowband echosounder, two optical cameras, a video recorder and two optical strobes. The buoys (green) on top allow the platform to maintain the motion.

The PLAOS has been designed and developed by CSIRO in Hobart, to collect high-resolution integrated acoustic-and optics data from the deep ocean at depths to ~1000 m based on a previous instrument (Marouchos et al., 2016). For the experiment, the PLAOS platform housed two broadband split-beam transducers (Simrad ES70-18CD and ES120-7CD), two single-lens reflex cameras (Canon EOS-1D X) and a video camera (GBO S1080 1'' Network). Two optical strobes were mounted to illuminate the sampled region. The platform held a motion sensor (Microstrain 3DM-GX1) and a CTD profiler (Seabird Electronics SBE37DO, SN 11417). A split-beam single frequency transducer (ES120-7CD) was also mounted on to the platform, but data from this instrument were not included. A detailed configuration of the acoustic and optics sensors PLAOS system configuration are shown in Table 7.1 and.Table 7.2.

Table 7.1: The configuration parameters of the two broadband echosounders.

Parameters	**Units**	**Values**	
		ES70 - 18 CD	**ES120-7CD**
Transceiver	EK 80	WBT 562899-15	WBT 536012-15
Serial number		116	109
Frequency	kHz	70	120
Beamwidth	Degrees	17.3	7.2
Power	W	400	250
Pulse length	µs	2048	2048
Pulse type		FM	FM
Frequency range	kHz	55 - 90	95-160
Equivalent beam angle	dB re 1 Steradian	-13	-20.7
Transducer Gain	dB	18	25
Sound speed	ms^{-1}	1493	1493
Angle sensitivity		10	23
Sphere range	m	5.5	4.4

Table 7.2: The configuration of the still and the video camera.

Variables	**Units**	**Oblique camera**	**Vertical camera**	**Vertical video**

Model		Canon EOS-1D X	Canon EOS-1D X	GBO S1080
Type		DSLR	DSLR	Network camera
Sensor size	mm	36 X 24	36 X 24	12.8 X 9.6
Focal length	mm	35	25	12.5
Dimensions	pixels	5184 X 3456	5184 X 3456	1920 X 1080
Resolution	dpi	72	72	
F-stop		f/6.3	f/11	
Exposure	sec	1/250	1/250	
ISO speed		6400	3200	

The transducers, ES70-18CD and ES120-7CD, operated at the frequency range 55 – 90 kHz and 95 – 160 kHz. The beamwidths were 18° and 7° at their centre frequencies of 70 kHz and 120 kHz. One of the cameras was installed so that its field of view included the acoustic axis of the 70 kHz echosounder. The other camera was placed at an oblique angle to capture the surrounding biota. The video camera was fitted to capture live recordings of the acoustic sampling volume. Additional datasets, conductivity, temperature, and depth and platform orientation were obtained from the CTD profiler and motion sensor. All the instruments were synchronised to the same time. During the deployment, the platform was lowered into the water and allowed to fall freely at its terminal velocity of approximately 0.4 m/s. The system was monitored from an onboard controller, and a rope tether was used for retrieval.

The echosounders recorded acoustic reflection with the maximum range set to 50 m. The cameras captured one photograph every two seconds. To perform in situ calibration, two tungsten carbide spheres (6% cobalt binder) 38.1 mm (WC38) and 22 mm (WC22) in diameter were suspended at 4.4 m and 5.5 m below the transducer. The intention of using two spheres was to optimise the entire frequency bandwidth from 55 – 160 kHz. The spheres need to be placed in the far-field range of the transducers. The near to far-field transition occurred around the range ($r > {}^{d^2}/_{\lambda}$) (Table 7.3), where d is the operational diameter of the transducer and λ is the wavelength. Three optical tags were placed at 1, 2 and 3 m below the transducer to provide a sense of depth in the photos.

Table 7.3: The near to far-field transition range of the transducers.

Parameter	Units	ES70-18 CD	ES120-7CD (m)
Frequency	kHz	55, 70, 90	95, 120, 160
Near to far-field transition range	m	0.31, 0.25, 0.19	1.01, 0.80,.0.61

7.2.2 The frequency response of the target strength and residual phase

To convert the raw broadband acoustic data collected by PLAOS to a single target amplitude and residual phase frequency response the following method was applied.

$F_{bs}(f)$ of any unknown acoustic target can be determined via Eq. (7.1)

$$F_{bs}(f) = \frac{CP_R(f)}{CP_T(f)L_{TL}(f)H(f,\theta)} \tag{7.1}$$

In the equation, $CP_T(f)$ is the autocorrelation of the transmitted signal and $CP_R(f)$ the cross-spectrum of the received and transmitted signals. $H(f,\theta)$ is the combined transmit/receive response of the transducer at the frequency, f and off-axis angle θ within the acoustic beam. Including θ allows us to include the directivity response of a circular transducer. $L_{TL}(f)$ is the two-way transmission loss due to the signal propagation, spreading and absorptions $\left(L_{TL}(f) = \frac{1}{r^2} e^{i\left(\frac{4\pi f}{c_w}\right)r} e^{2\alpha_w(f)r}\right)$ where r (m) is the range, c_w (m/s) is the speed of sound in water and $\alpha_w(f)$ is the absorption loss. Once $F_{bs}(f)$ is determined $TS(f)$ and $RP(f)$ of the target can be derived via Eq. (7.2) and (7.3). For a detailed description of the background theory, refer to section 3.2.1 and section 5.2.2.

$$TS(f) = 10\,log_{10}|F_{bs}(f)|^2 \tag{7.2}$$

and

$$\varphi_{bs}(f) = unwrap(angle(F_{bs}(f)) \tag{7.3}$$

The computed $TS(f)$ are corrected for the transducer directivity due to the use of $H(f,\theta)$ corresponding to the position within the acoustic beam. In Chapter 5 it was shown that the phase values within the main lobe are independent of θ. Therefore, to calculate $RP(f)$, $H(f,0)$ is used in Eq. (7.1) instead of $H(f,\theta)$.

7.2.3 Data analysis

The acoustic and video datasets were first investigated using Echoview (Echoview, 2017) and later a detailed analysis of all three (acoustic, video and photograph) was carried in Matlab (Toolbox, 2016).

7.2.3.1 Preliminary processing

A preliminary investigation was conducted using Echoview as it allowed simultaneous inspection of the video and acoustics data. Organisms within the 90° field of view of the camera could be distinguished at ranges up to ~6 m. The region between 0 and 2 m was in the near field of the transducer and hence was ignored. The Echoview single target detection algorithm (wideband) was run between 2 - 8 m. The variables for the algorithm were set to -70 dB for the compensation TS threshold, 6 dB the pulse length determination level (PLDL). The minimum and maximum normalised pulse length were 0.01 and 1.5, and the frequency graph size window was 0.15 m above and below the target. The maximum standard deviation of the major and minor axis angles was 0.6°, and the maximum beam compensation parameter was 12 dB (Echoview, 2017).

The pulse-compressed echogram was synchronised to the video file to link imaged and acoustic recordings. The video was inspected to confirm the presence of micronekton. Regions with multiple organisms were ignored. When a single acoustic target corresponded to an organism in the video, the frequency versus $TS(f)$ curve was drawn to make an initial impression of the scatterer's features. The objective was to include micronekton with different scattering characteristics. Micronekton seen on the video and as a single target in the echogram were searched for their presence in the corresponding photograph taken by the vertical camera. Once an organism's occurrence was confirmed by all three methods, the echogram, video and the photograph, the time and range were logged. Due to the poor frame rate of the camera, very few animals could be identified simultaneously in all the three datasets. Further processing was then carried out with custom-designed Matlab codes specially developed for the purpose.

7.2.3.2 Conversion from 3D acoustic to 2D pixel coordinates.

A split-beam transducer measures a scatter's location in the three dimensions: range and major and minor angles from the transducers central axis (Ehrenberg, 1981). It was assumed that the water within the sampling volume was homogenous at a constant density and sound speed. A single vision camera generates photographs in a two-dimensional pixel coordinate system from one viewpoint. An algorithm was formulated to transfer 3D acoustic coordinates of a scatterer to 2D pixel coordinates in the photograph. There were four coordinate systems, the PLAOS (x_p, y_p, z_p), echosounder (x_a, y_a, z_a) camera $((x_o, y_o, z_o)$ and the photo (u, v). The position and the tilt of the echosounder and the camera, to the centre of the PLAOS coordinate system, are given in Table 7.4.

Table 7.4: The tilt angles and distance of the camera and transducer to the centre of the PLAOS coordinate system.

Variables	Units	ES70-18CD	Canon EOS-1D X
Tilt in XZ plane	(°)	2.5	7.5
Tilt in YZ plane	(°)	1.5	1.5
Distance from 70 kHz (x, y and z)	mm	(0,0,0)	(-310,-140,0)

Assuming that a target, T1 was sampled simultaneously by the echosounder and the vertical camera.T1 was seen at (x_{a1}, y_{a1}, z_{a1}) in the echosounder coordinate system, and at (x_{o1}, y_{o1}, z_{o1}) in the camera coordinate system. In the PLAOS coordinate system, T1 was situated at (x_{w1}, y_{w1}, z_{w1}). The same T1 could be seen at (u_{o1}, v_{o1}) in the photograph.

The transfer of T1 from (x_{a1}, y_{a1}, z_{a1}) to (u_{o1}, v_{o1}) was realised in three steps (a) conversion from the echosounder to the PLAOS coordinate system, Eq. (7.4); (b) the transformation from the PLAOS to the camera coordinate system Eq. (7.5); and, finally (c) conversion from the 3D coordinate system of the camera to the 2D system of the photo Eq. (7.6) and Eq. (7.7). In the equation, $R_a = [R_{az}R_{ay}R_{ax}]$ and $R_o = [R_{oz}R_{oy}R_{ox}]$ were the rotational matrix and $\begin{bmatrix} \mathrm{T_{xa}} \\ \mathrm{T_{ya}} \\ \mathrm{T_{za}} \end{bmatrix}$ and $\begin{bmatrix} \mathrm{T_{xo}} \\ \mathrm{T_{yo}} \\ \mathrm{T_{zo}} \end{bmatrix}$ were the translation vector along x, y and z directions in the echosounder and camera coordinate system.

$$\begin{bmatrix} x_{w1} \\ y_{w1} \\ z_{w1} \end{bmatrix} = [R_a] \begin{bmatrix} x_{a1} \\ y_{a1} \\ z_{a1} \end{bmatrix} + \begin{bmatrix} T_{xa} \\ T_{ya} \\ T_{za} \end{bmatrix} \tag{7.4}$$

Similarly,

$$\begin{bmatrix} x_{o1} \\ y_{o1} \\ z_{o1} \end{bmatrix} = [R_o] \begin{bmatrix} x_{w1} \\ y_{w1} \\ z_w 1 \end{bmatrix} + \begin{bmatrix} T_{xo} \\ T_{yo} \\ T_{zo} \end{bmatrix} \tag{7.5}$$

The focal length, f_{oa} (m^{-1}) of the camera in air modifies to $f_{ow}, (f_{ow} = f_{oa}/n_w)$ in water with refractive index n_w. The horizontal and vertical sensor size of the camera were h and w (mm) given in Table 7.2 and h_{res} and w_{res} were the horizontal and vertical resolution in pixels.

$$u_{o1} = \left(f_{ow}\left(\frac{x_{o1}}{z_{o1}}\right) + \frac{h}{2}\right) \times h_{res} \quad (7.6)$$

$$v_{o1} = \left(f_{ow}\left(\frac{y_{o1}}{z_{o1}}\right) + \frac{w}{2}\right) \times w_{res} \quad (7.7)$$

To test the accuracy of the transformation technique acoustic coordinates of the optical tags and the calibration spheres were transformed (Figure 7.2). In another example, a single target identified at 3 m matched to a squid in the corresponding image file. The squid was also seen in the video at the same time.

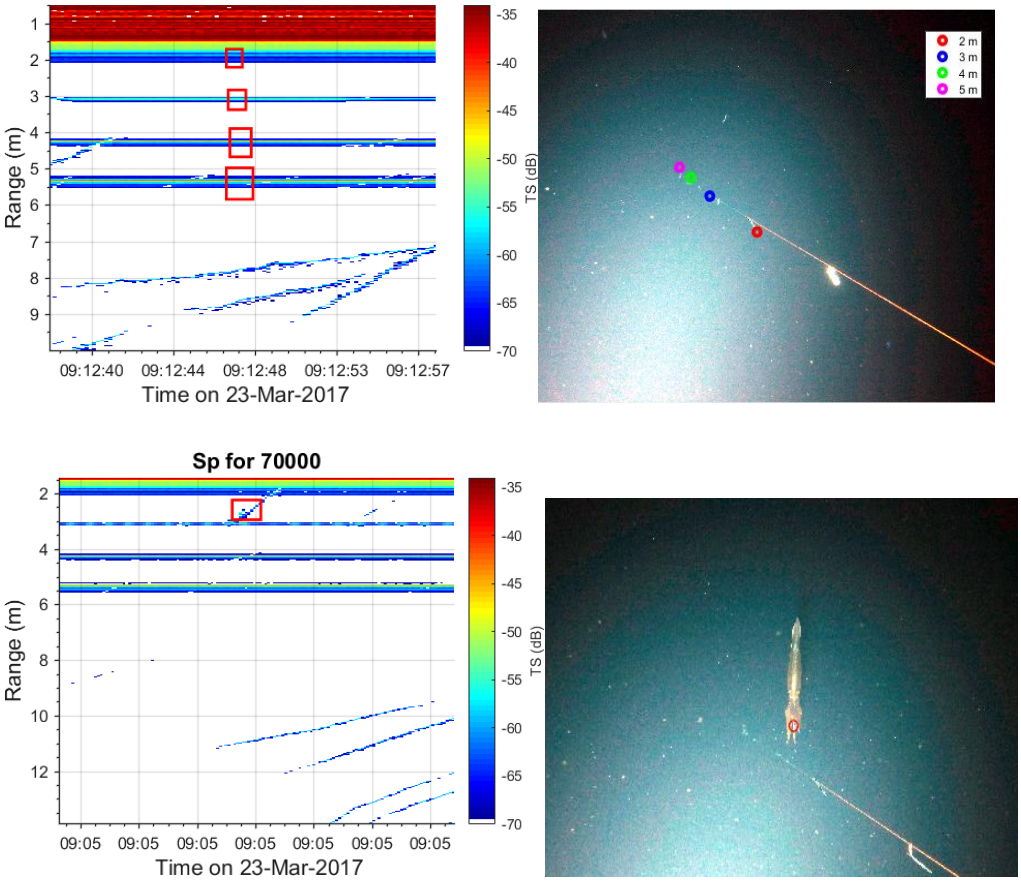

Figure 7.2: The optical tags at 2 and 3 m and spheres at 4.2 and 5.5 m marked with a red box in the echogram (top left) transformed to the image (top right). The range of each is shown in the legend. A single target at 3 m in the echogram (red box) was identified as a squid from the video (bottom left). The acoustic coordinates, when transformed pointed at the squid in the photo (bottom right).

7.2.3.3 Acoustic processing

To calibrate the acoustic system backscattered signals from the WC22 sphere was used to determine $H(f, \theta)$ of the transceivers. Although the WC22 sphere is not a preferred target for calibration in the frequency range 95- 160 kHz, it was chosen, due to a

comparatively flat response between 55 and 160 kHz as compared to the WC38 sphere (Demer et al., 2015). A Matlab code (Chu, 2011) was used to derive the $F_{bs,cal}(f)$ (Faran, 1951; MacLennan, 1982). Signals were time-gated using a Hanning window of length 0.4 m from the peak to both sides. Recordings between 0.0° and 3.5° off-axis angle and 200 – 500 m depth, were divided into bins, each of an angle width 0.5°. To remove noise from unwanted scatters and reverberation, recordings beyond one standard deviation of the mean TS for each bin were excluded (assuming the data distribution to be a Gaussian). A conservative 68% confidence interval based on a normal distribution was used to ensure that no error was introduced. The absorption and the transmission loss was found as a function of frequency at the recorded sound speed, salinity and temperature (Francois, & Garrison, 1982; Mackenzie, 1981). The averaged $H(f,\theta)$ for each bin was found by substituting match filtered transmitted and received signal and theoretical value of $F_{bs}(f)$ of the sphere derived using a Matlab code developed by Chu (2011) based on Faran (1951) and (Foote, & MacLennan, 1984).

Once a single target in the echogram was confirmed as an organism of interest, the acoustic data was extracted by windowing the pulse-compressed signals with a Hanning window, that extends 0.4 m on either side of the peak. Extra care was taken to ensure that there were no other scatterers in the vicinity. Earlier in Chapter 5, a window length of 0.7 m was used to extract $RP(f)$, but it was not possible to use a window that long in the open ocean due to the presence of multiple organisms. The signals from 0° – 3.5° were divided into off-axis bins of width 0.5°. To provide a conservative estimate data beyond a 68% confidence interval from the mean TS were removed. This could eliminate several signals but was deemed imperative as a precautionary measure to minimise the artefacts and interference from other sources within the window. For each ping, $TS(f)$ was computed by substituting the magnitude of $H(f,\theta)$ interpolated to the off-axis angle θ in Eq. (7.2) and Eq. (7.3).To derive $RP(f)$ the complex $H(f,0)$ function was used in the Eq. (7.2) and Eq. (7.4).

7.2.4 Scattering model

In this study, a simple scattering model consisting of a gas-filled sphere with homogenous acoustic properties has been used. The model is an approximation to predict backscatter from fishes with swim bladders or gaseous bubbles and has been previously used in fisheries with different modifications (Andreeva, 1974; Weston, 1967; Ye, 1997b). The complex backscattering amplitude, $F_{bs}(f)$ from a gas-filled sphere of

equivalent radius, a (m) can be expressed as Eq. (7.8) (Morse et al., 1969). The sphere acts as a point source independent of the orientation.

$$F_{bs}(f) = \frac{a}{\frac{f_0^2}{f^2} - 1 - \frac{1i}{Q}} \tag{7.8}$$

Here f_0 is the resonant frequency, and Q is the quality factor that is the inverse of the damping constant δ). Various components (thermal, viscous and radiation) contribute to the damping constant (Devin Jr, 1959). For a typical fish swim bladder, the value of Q is 5 (Diachok, 2001), which is also used as an approximation in the absence of accurate values (Lavery et al., 2007). f_0 remains a function of the radius and the depth, D (m) as given by Eq.(7.9).

$$f_0 = \frac{1}{2\pi a}\left(\frac{3\gamma(P_0(1+0.1D))}{\rho}\right)^{\frac{1}{2}} \tag{7.9}$$

Here γ, ($\gamma = 1.4$) is the ratio of the specific heat of the body, and the outer fluid, P_0 ($P_0 = 1.103 \times 10^5$ Pa) is the pressure at the surface, and the density is ρ ($\rho = 1027$ kg/m^3. In the absence of any empirical data, the values used were from earlier literature (Medwin, & Clay, 1998). $TS(f)$ and $\varphi_{bs}(f)$ can be computed via Eq. (7.10) and (7.11).

$$TS(f) = 10\,log_{10}\left|a^2\left(\left(\frac{f_0^2}{f^2} - 1\right)^2 + \frac{1}{Q^2}\right)^{-1}\right| \tag{7.10}$$

$$\varphi_{bs}(f) = unwrap\left(tan^{-1}\left(Q^{-1}\left(\frac{f_0^2}{f^2} - 1\right)^{-1}\right)\right) \tag{7.11}$$

7.3 Results

The PLAOS deployment of approximately 2.5 hours generated 12 GB of acoustic recordings with scattering from many single scatterers (2-20 cm fishes, squid, crustaceans and gelatinous), multiple scatterers and noise. The vertical and oblique cameras took approximately 5000 photographs (~40 GB) in 1 hour and 19 minutes duration. 2.78 GB of video footage was recorded. When taut, the tether coupled wave-induced ship motion to the PLAOS, causing it to undergo significant periodic vertical motion during the upward movement of the platform. Thus the investigation was limited

to the time the PLAOS was free-falling downward with a loose tether.

Many resonant scatterers were identified although some, which existed in the acoustic data, were not discoverable in the photographs. Several myctophids were observed but identifying them on the photographs was difficult due to their swimming patterns and avoidance of the platform. The spectra of five selected targets are presented as examples.

Even though the information obtainable from the photographs was insufficient to allow theoretical $RP(f)$ curves to be computed for the organisms, it was significant to determine whether in practice, it can be used as an acoustic discriminator and if it depends on the target's characteristic features. An approach to test the proposition was to fit both $TS(f)$ and $RP(f)$ to the prediction of a numerical scattering model by adjusting the model's parameters. Three examples of resonant scatterers found at different depths and with distinct resonant frequencies were fitted to the output of a resonant gas filled numerical scattering model. The spectra of an unknown fish and a squid is also shown, however no attempt has been made to fit these to data.

In the first example, the acoustic signature of a possible gas-filled target was matched to the output of a numerical scattering model of a gas-filled sphere (Figure 7.3). A single target could be seen in the echogram from ~11 m to ~5m. The target at ~7 m (green box) when transformed to image coordinates pointed to a group of targets. From the photo, it could not be confirmed if the targets were of biological or non-biological origin and if they had gas inclusions. It can be concluded that this target was not a large mesopelagic organism.

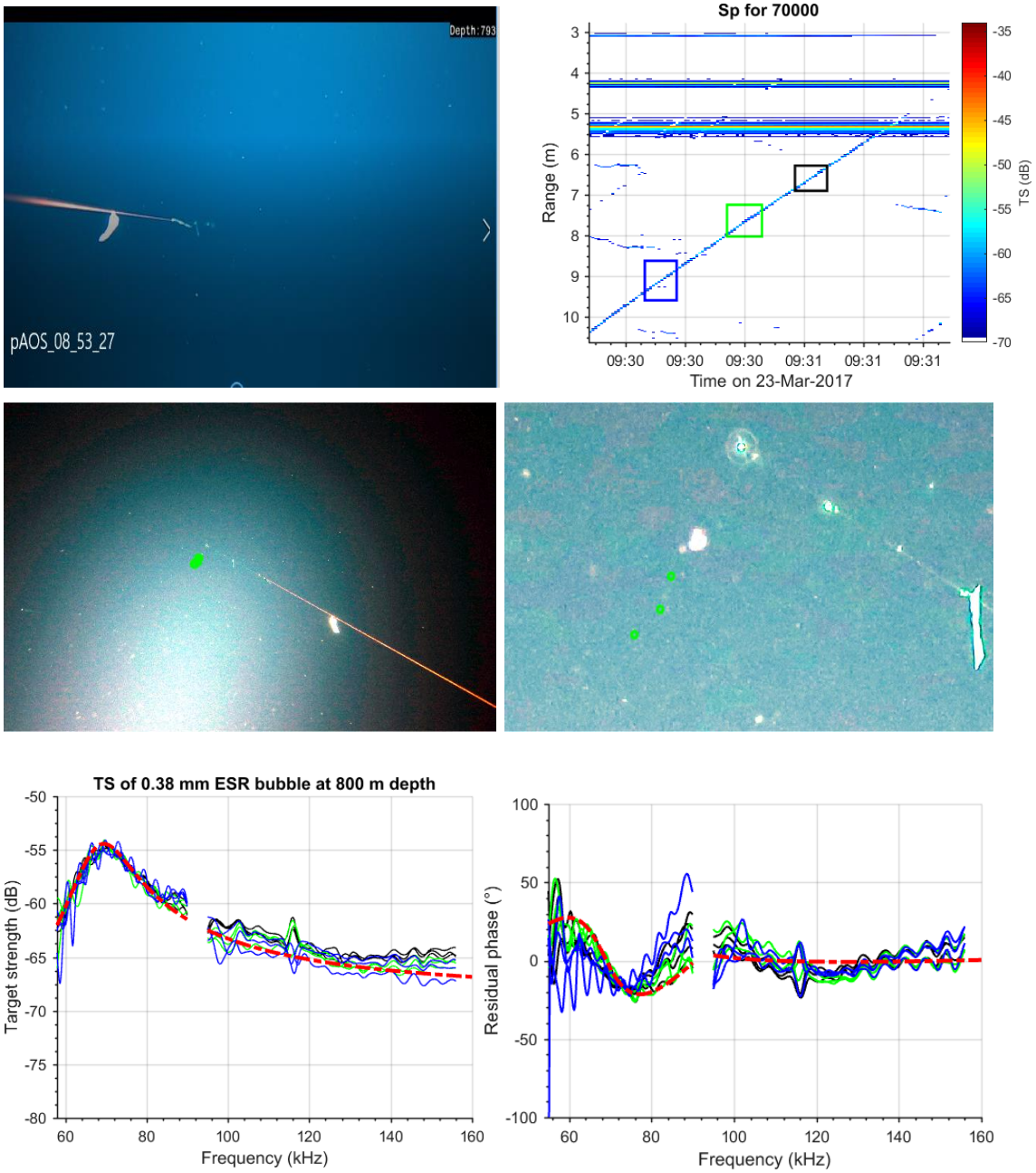

Figure 7.3: A single target detected on the video (not marked) and (top left) echogram (top right). The transformation at ~7 m (green box) to the still image points to small targets (middle). The left middle image is zoomed to produce middle right image. It could not be confirmed if the targets were biological or non-biological. The $TS(f)$ (bottom left) and $RP(f)$ (bottom right) between 55 – 90 kHz at all the three points matched to the output of the numerical model of a gas-filled sphere (red dotted line). The line colours blue, green and black on the bottom row correspond to the target positions seen in the top right echogram

The $TS(f)$ and $RP(f)$ of the target were plotted at different ranges, ~9 m, ~7.5 m and ~6.5 m, from the transducer (shown by blue, green and the black box). $TS(f)$ was consistent at all three points, exhibiting resonance at 69.5 kHz with a maximum target strength of -54 dB. The corresponding $RP(f)$ curve moved from +29° to -20° passing

through 0° at the resonant frequency, 69.5 kHz. The low signal to noise ratio at the high range (~9 m) led to larger fluctuations in the $RP(f)$ as compared to $TS(f)$ but improved as the target came nearer to the transducer. The simple numerical model for a gas-filled, homogenous sphere outlined in section 1.2.2 was fitted to the data. For the set of features, $Q = 5$ $a = 0.39$ mm and $\gamma = 1.4$, the model output (red dotted line) simultaneously fits $TS(f)$ and $RP(f)$ responses.

In another example, the acoustic signature of a single target at 633 m depth and 3.5 range from the transducer was plotted (Figure 7.4).

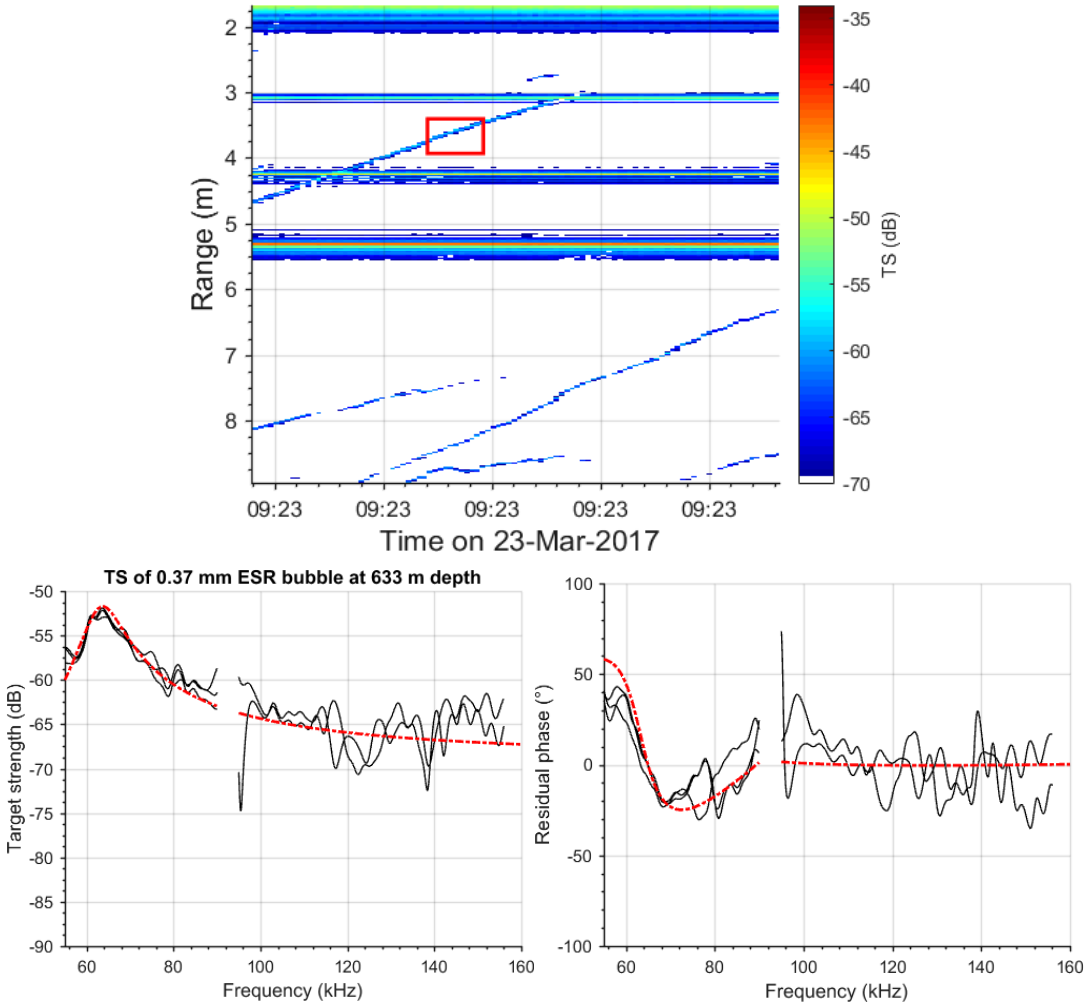

Figure 7.4: A single target (red box) observed between 3 and 4 m from the transducer (top). The $TS(f)$ (bottom left) and $RP(f)$ (bottom right) between 55 – 90 kHz fitted to the output of the numerical model of a gas-filled sphere (red dotted line).

The target could not be verified optically in the photograph. The $TS(f)$ exhibited resonant characteristics with a peak of -51.8 dB at 64 kHz. The $RP(f)$ moved from a maximum of 43 0° to minimum 23.1° between 58 kHz to 69 kHz passing through 0° at the resonant

frequency, 64 kHz. The signal was noisy between 100 kHz and 160 kHz. Both the $TS(f)$ and $RP(f)$ of the scatterer matched to the theoretically predicted output values for a modelled gas-filled sphere of radius 0.37 m and Q of 7.

A fish was seen in the video directly below the sphere when the platform was at a depth of 469 m (Figure 7.5).

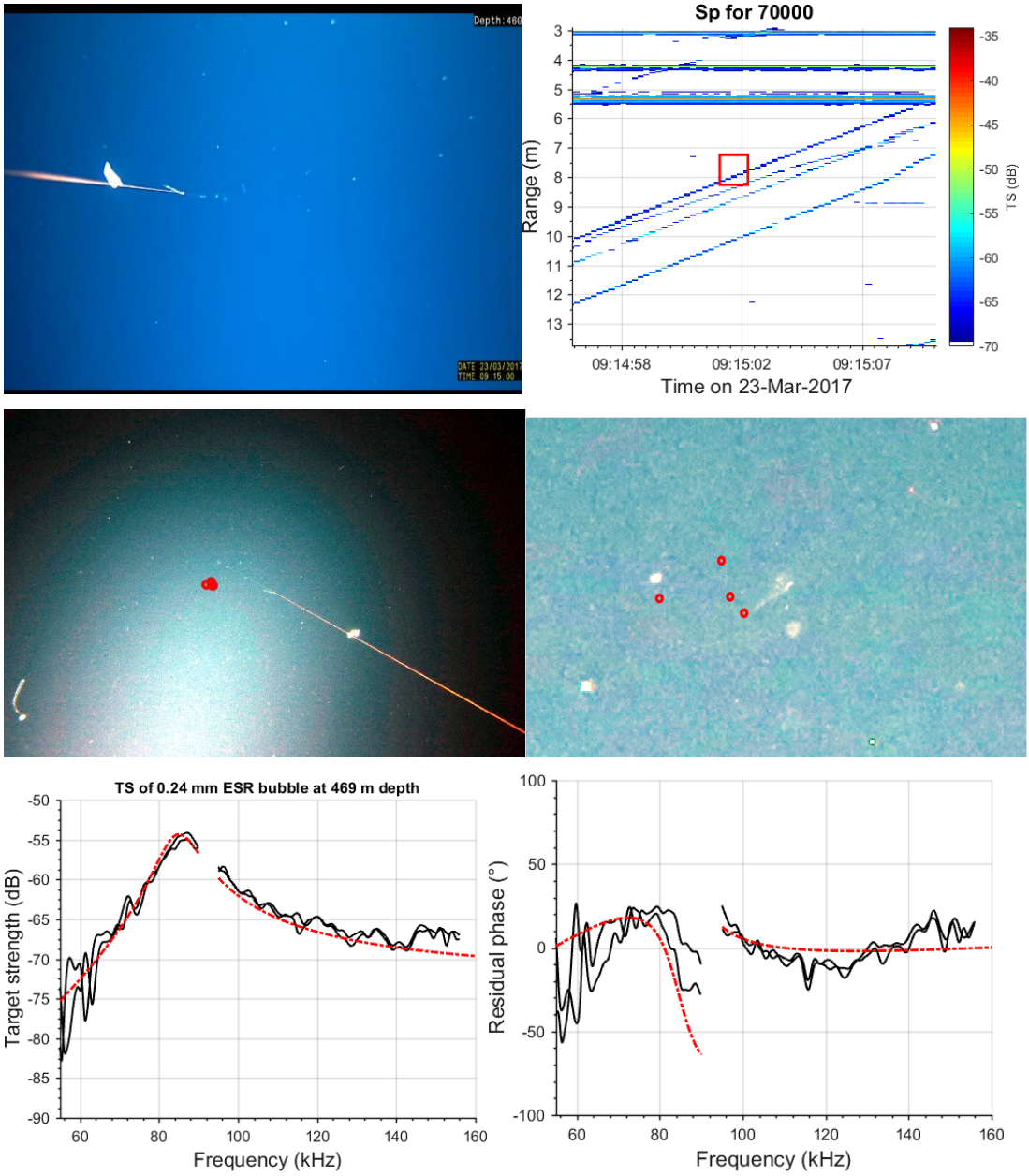

Figure 7.5: A fish below the sphere in the video clip (top left.) The corresponding target enclosed in a red box on the echogram (top right). The conversion of acoustic to the pixel coordinates points (in red circles) to a fish in the image (middle left). A zoomed view of the image showing fish and stationary targets (middle right). The target strength (bottom left) and the residual phase (bottom right) drawn to the frequency.

This corresponded to a single target in the echogram, which pointed to a fish in the still image after the transformation. The mark on the photograph encircled the whole fish. But when zoomed in, a few small targets were also seen and therefore, the possibility of them as a scattering source could not be ignored. The stationary target could not be verified and is unlikely to be a large fish as the fish was mobile and not seen in subsequent images. A target in an image can be at any range that could be resolved by stereo optics depending on the object size and optical resolution.

The $TS(f)$ was typical for a resonant target ranging from --75 dB at 55 kHz to a maximum of -54 dB at the resonant frequency 87 kHz, beyond which it dropped to -70 dB at 160 kHz. $RP(f)$ progressed from maxima to the minima through 0° at the resonant frequency. Both the curves simultaneously matched to the output of the numerical model (red dotted line) for gas-filled spheres for, $Q = 8$, $a = 0.24$ mm and $\gamma = 1.4$. The noise degraded the $RP(f)$ curves affecting the interpretation, especially below 60 kHz.

Another fish was seen in the video ~2.5 m and as a single target on the echogram (Figure 7.6).

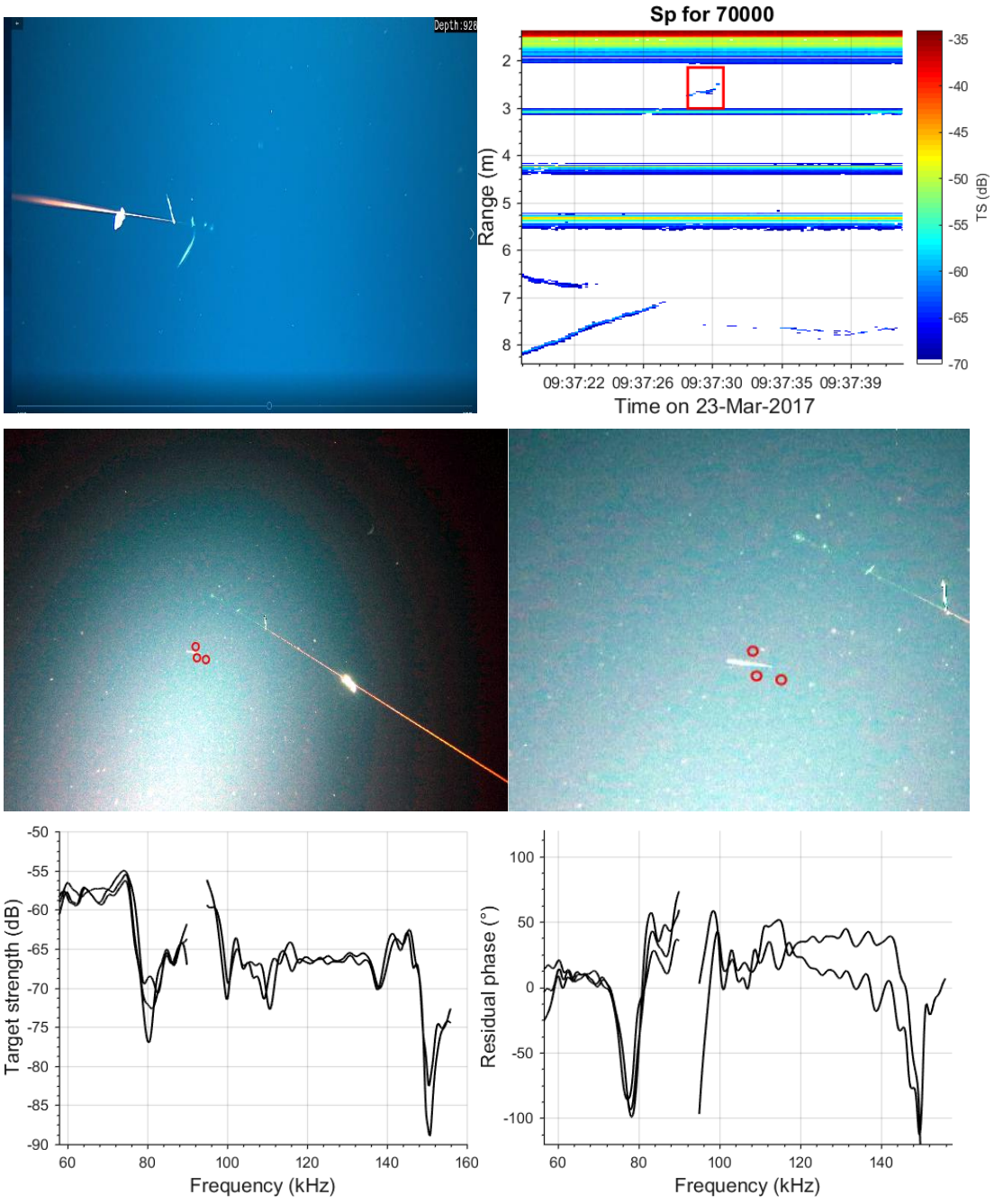

Figure 7.6: A fish visible at the ~3 m in the video (top left). A single target corresponding to the same depth and time enclosed within a red box in the echogram (top right). The conversion from the acoustic coordinate to the photo pointed to the fish (middle left). A zoomed view of the fish (middle right). The $TS(f)$ (bottom left) and the $RP(f)$ (bottom right) plotted to the frequency.

The spatial transformation confirmed the single target in the echogram as a fish. $TS(f)$ was steady at -60 dB but structures were noticed at 80 and 150 kHz. $RP(f)$ followed the

same pattern starting from ~0° and a sudden dip to -100° at 80 kHz and 150 kHz. This particular acoustic signature was observed several times in the acoustic recording. In the echogram, the target was seen to modify its movement as the platform came nearer to it (~8 m). This particular example was chosen because of the close range to the camera.

The sphere and the strobe light attracted squid near the platform providing some good imagery and acoustic datasets. However, most of the time they were observed near the sphere. A squid at a range ~5 m was seen in the video at a platform depth of 611 m (Figure 7.7).

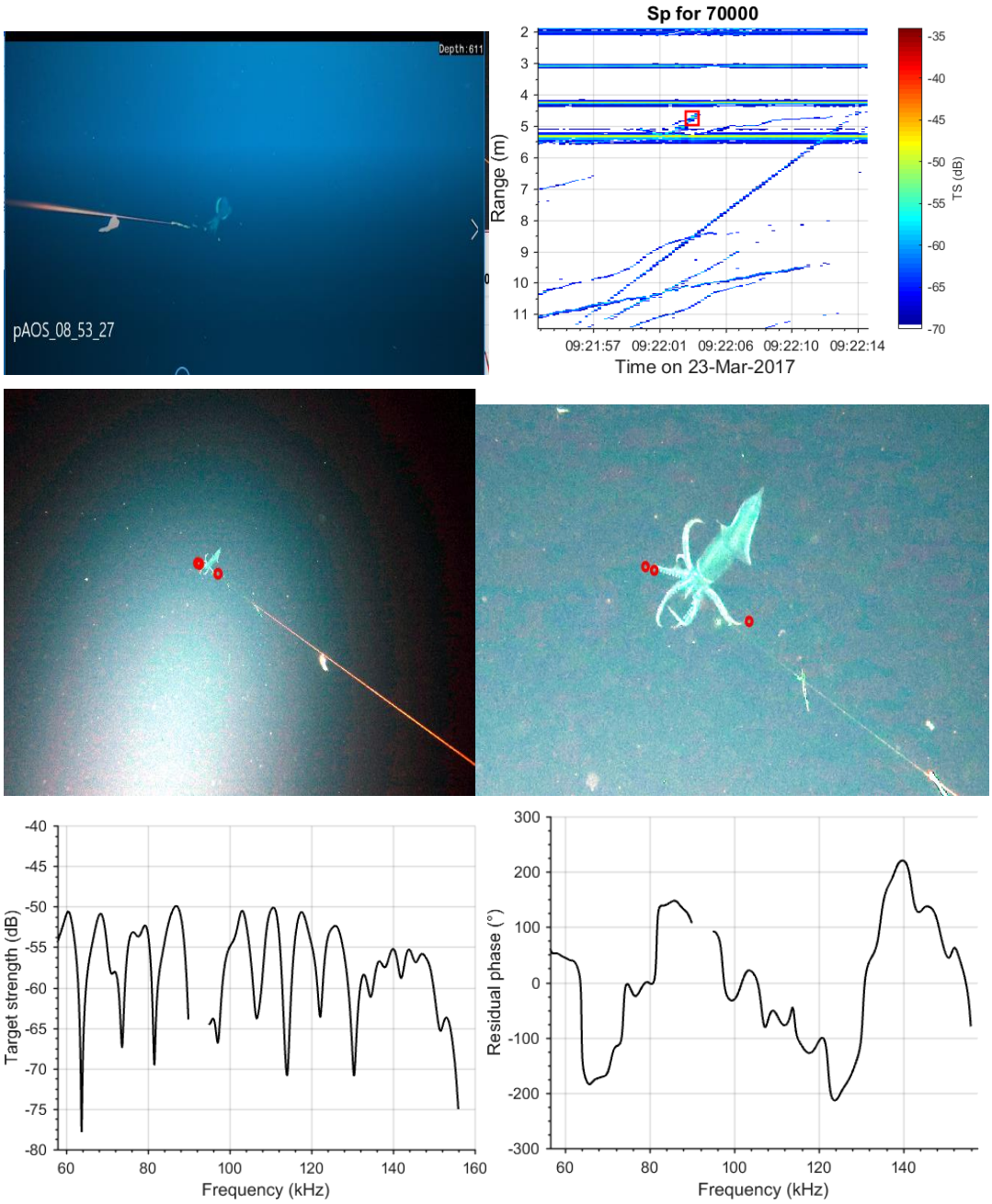

Figure 7.7: A squid is seen in the video clip (top left). A single target corresponding to the time and range in the echogram is highlighted by a red box (top right). The conversion of acoustic to the pixel coordinates in the image points to a squid (red circles) (middle). The $TS(f)$ (bottom left) and the $RP(f)$ (bottom right) obtained from the acoustic data. The plotted $TS(f)$ and phase results were from a single ping.

The time and the range matched a specific target in the echogram. The acoustic coordinates, when transformed pointed to a squid in the corresponding photograph. The $TS(f)$ was at -52 dB, with alternate nulls varying up to -20 dB due to the destructive interference from waves at the different interface. No definite pattern was visible in the $RP(f)$. This does not mean that $RP(f)$ was inefficient. The pattern was meagre because

of the inversion in the phase between, 65 and 130 kHz probably due to the incomplete unwrapping and and the particular target orientation.

7.4 Discussion

The study measured the acoustic signatures of five different micronekton and at the same time tried to establish if $TS(f)$ and $RP(f)$ drawn together could be of any significance in remote detection of marine organisms. Though many targets were observed, the synchronous analysis was limited to five targets of different behaviours and responses as the goal of the chapter was to demonstrate the realisation of the method. Three techniques were used in the study.

1. The application of geometric transformations to allow acoustic targets to be localised in optical images.

2. Broadband acoustic signatures consisting of both $TS(f)$ and $RP(f)$ spectrum.

3. An amplitude and phase inclusive numerical acoustic scattering model for gas-filled sphere targets.

The challenges and limitation of each are discussed.

7.4.1 Acoustic-optics conversion.

The unification of the acoustics, video and photos via the spatial transformation technique (section 7.2.3.2) enabled visual of all the targets analysed. In some cases, bias was noticed in the transformation outcome, especially when the photographs were zoomed out. This could be due to specific issues that remained unresolved by the algorithm.

1. The location of a scatter in the echogram was determined in the electric angles by the split-beam processing. It was assumed that the geometrical angles matched to the electrical angles, but this could not be confirmed by an independent experiment.

2. The tilt angles of each instrument were evaluated at the time of onboard installation. Any variation in these values could lead to significant errors as these act as input to the algorithm.

3. The camera specifications provided by the manufacturer were used. It is usually recommended to perform an independent assessment of the camera specification. However, this was not attempted due to logistic and time constraints.

The frame rate of the camera (one every two seconds) was lower than the ping rate of the echosounder. As a result, many organisms (more than 50) were rejected even though they were visible on the echogram and the video. Conversely, several times, animals were detected in the photo and the video but were outside the acoustic sampling volume. Furthermore, matching mesopelagic fishes was a challenge due to their constant and fast swimming movement. The fishes showed sensitivity to the flashlight (seen in the video), and the platform motion and hence very few came within the acoustic sampled volume at ranges at which they could be optically identified. As a result, the analysis of the 1.5 hours of data was a time consuming and lengthy procedure.

In this study, single lens, camera and echosounder measurements were quantitatively integrated. A single-lens camera is usually limited to qualitative scrutiny of the sampled biota such as size estimation, species identification (Dunlop et al., 2018; Warren, & Wiebe, 2008) or behavioural modification (Macaulay et al., 2012). Using a single camera had several limitations. Even if the position of a specific acoustic target is known, it cannot be distinguished optically from targets at other ranges that appear at the same location in the image. Thus, it is not possible to verify if the acoustic and optical targets are the same without more spatial or temporal information such as multiple images with acoustic registration. By contrast, a stereo vision or set of two cameras 3D system can optically determine the target range, which makes misidentification much less likely (Kang et al., 2005). A sophisticated stereo video was used by Takahashi et al. (2004) to identify and estimate the length of fish up to 300 m and by Sawada et al. (2009) to measure the tilt angles and length of anchovies. Briseño-Avena et al. (2015) used an advanced system to undertake broadband measurements from single copepods with stereoscopically calibrated microscopes.

The effectiveness of a camera is limited by its optical resolution or the real dimension a pixel represents. The size of the smallest object a camera can detect or the optical resolution plays an important role in the verification of the target. Targets smaller than this optical resolution cannot be verified. The spatial resolution is determined by the physical specification of the camera, surrounding environment and field of view. For the

vertical camera (Canon EOS-1D X).Table 7.5 gives the horizontal distance corresponding to one pixel as a function of range.

Table 7.5: The optical resolution of the vertical camera as a function of range

Range (m)	Optical resolution of the vertical camera (Canon EOS-1D X) (mm)
1	0.8
2	1.5
3	2.3
4	3.0
5	3.8
8	6.0
10	7.5

A 1-pixel resolution of the photograph corresponds to an object 1.5 mm at 2 m range, or 6 mm at 8 m range. In practice, multiple pixels are required to detect and identify an object, for example, a 3 cm fish at 4 m would have at most 10 pixels. This limits the size of the smallest object that can be resolved by the camera. Even if the transformation matrix points to an object in a photograph, the possibility of it corresponding to the single target detected in the echogram is limited by the optical resolution at that range. Thus, in all the examples shown in the result section, a possibility of the acoustic backscattering coming from a surrounding target smaller than the optical resolution cannot be ruled out. Further, even if stereo cameras are used, the ability to differentiate two objects will be limited by its resolution.

7.4.2 Broadband acoustic signature

One of the main improvements with the broadband echosounder was the simultaneous extraction of both $TS(f)$ and $RP(f)$ from the backscattered echoes. $H(f,\theta)$ was computed during the deployment, which included any modification in the transducer parameters due to the mounting or the platform motion.

The consistency of $TS(f)$ and $RP(f)$ plots of the small gas-filled target at all three ranges verified that the acoustic signature of a single target is unique and that together $TS(f)$ and $RP(f)$ can be reliably used for characterisation of acoustic targets. The position of the gas-filled target changed within the acoustic beam due to the continuous movement but $RP(f)$ spectra remained consistent for different pings. This result validated the insensitivity phase to the target position (in Chapter 5) and thus the use of on-axis system

response in the computation. This result could be significant for the identification of organisms without the need for compensation for the directivity as done for $TS(f)$ measurements. The acoustic signature of other two resonant targets (an unknown and a fish) further confirmed the stability of $RP(f)$for each target. On the downside, $RP(f)$ profiles were prone to the presence of noise that significantly impeded visualisation of the actual target induced phase in some cases. This was evident at the extremes of the frequency bands, which was probably due to the lower SNR.

The $TS(f)$ of the squid (Figure 7.7) matched the spectra shown in Jones et al. (2009) and Lee et al. (2012). The ping-to-ping variation (not shown in the figure) was probably due to the change in the orientation and scattering from different parts such as the tentacles or the mantle. The squid was found near to the sphere, which is a strong scatterer as compared to the squid. Hence, possibilities of contamination due to the overlap of side lobes could not be ruled out. In the video footage, each time a squid was found, it was near the sphere leaving no chance to derive their acoustic spectra without contamination. Therefore, it would be worthwhile investigating the acoustic spectra of squid in other deployments without the calibration sphere. The $TS(f)$ of the fish in Figure 7.5 is typical of adult mesopelagic fish, where the gas-filled thin-walled swim bladders contribute to the overall backscattering (Butler, & Pearcy, 1972). The signature was noisier due to the low signal to noise ratio at the higher range. This acoustic signature shown in Figure 7.6 was observed several other times during the deployment. However, the quality of the optical images was insufficient to allow identification of the fish species

The difference in the $RP(f)$ plots confirmed its link to the shape, size and the material properties of the organisms. The calibration would be simple, as it would only require determining the on-axis system response or off-axis response. One of the challenges would be to avert the incomplete unwrapping that leads to an abrupt jump in the phase by ±360°, as seen in the case of squid. In the previous chapter, the window length was increased to 0.7 m. This was not realistic in an open ocean due to the presence of several targets in proximity.

The current study presents the first set of frequency responses of the target phase of in situ live organisms. Despite an extensive set of literature available on the processing and analysis of phase, the measurements achieved so far could not indicate its efficacy as a reliable acoustic index for characterisation. Earlier, Barr, and Coombs (2005) obtained the target phase of three fishes and compared the result to the model output. This was

achieved at a single frequency of 38 kHz, and the precision could be argued due to the absence of system calibration. Atkins et al. (2007) presented phase measurements in angles from copepods and euphausids with LFM across 1600 – 2500 kHz.

7.4.3 A comprehensive numerical scattering model.

A common practice in marine acoustics is to estimate the relationship between an organisms characteristics and the target strength by using numerical scattering model (Horne, & Clay, 1998). This study attempted to investigate if like target strength, residual phase could also be linked to the target physical and morphological features. The comparison of the measured $RP(f)$ from three different resonant targets to the output of a numerical scattering model for gas-filled sphere verified that $RP(f)$ describes the target characteristics in the same way as the echo amplitude or $TS(f)$. The in situ $RP(f)$ measurements were consistent (from ping to ping) at the different range and in the case of the resonant target agreed with the theoretical phase at all points (Figure 7.3). Even for the two other resonant targets with a disparate resonant frequency, the $TS(f)$ and $RP(f)$ simultaneously fitted to the output of the numerical scattering models. This provided a strong basis to the hypothesis that $RP(f)$ can be useful as an acoustic metric. For all the three resonant targets, $TS(f)$ was maximum, and the corresponding $RP(f)$ was 0° at the resonant frequency.

The results presented in this chapter are preliminary and intensive efforts are required to substantiate the use of $RP(f)$ as an acoustic classifier. For example, ex-situ experiments can be performed with a fish of known geometric and physical parameters and the acoustic backscatter be recorded. A comparison of the $RP(f)$ value derived with the output of the numerical model will enable assessment of phase as an acoustic classifier. Furthermore, exact or approximate analytical models for different shapes should be extended to predict the theoretical $RP(f)$ values (Jech et al., 2015). This would enable evaluation of $RP(f)$ for other acoustic groups such as zooplankton, cephalopods or crustaceans.

7.5 Conclusion

The remote sensing of the mesopelagic micronekton is presented in this chapter. The broadband echosounder together with the video and still camera mounted on PLAOS platform, served as a comprehensive tool to sample micronekton. The combination of the acoustic and optics coordinates provided qualitative verification of the single targets

observed in the echogram, although due to the small size of the resonance gas inclusions this was sometimes ambiguous. The frequency response of the target strength and residual phase of five different targets (a squid, mesopelagic fish, two small targets gas-filled unknown target) enabled confirmation of the proposed method. The target strength and residual phase of each target (except the squid) was consistent from ping to ping. The matching of the numerical acoustic scattering model outputs to the measured acoustic signature of an in-situ small gas-filled target, an unknown target and a mesopelagic fish provided validation to the inclusion of the residual phase as a reliable acoustic index. The implementation of this technique in the future could provide an avenue to study the spatial-temporal dynamics of micronekton and investigate their distribution.

Acknowledgements

We would like to thank the team members and crew of RV Investigator for the efforts and help in the deployment of PLAOS. Special thanks to Jeff Cordell for the setup of the experiment. Special thanks to Tim Ryan and Haris Kunnath for the valuable inputs to the deployment. This study was undertaken as a part of the Great Australian Bight Research Program, a collaboration between BP, CSIRO, the South Australian Research and Development Institute (SARDI), the University of Adelaide, and Flinders University.

Chapter 8

Discussion, recommendations and conclusion.

The research presented in this thesis focuses on the development and implementation of a technique for the calibration of a broadband echosounder to allow it to measure the frequency response of target strength and phase. The feasibility of the method was explored through its application to in-situ micronekton distributed in the mesopelagic regions of the Great Australian Bight and the Southern Ocean. A procedure was developed to simultaneously calibrate the echosounder for both target strength and phase measurements, and an evaluation was carried out to explore its capabilities and limitations. The approach uses the same system response function to derive the target strength and phase by keeping the variables in complex form. It was also important to ascertain that the outputs were not affected by variations in the transducer parameters from the manufacturer provided nominal values due to external factors (such as mounting and local environmental variables). This research makes a significant contribution to the field of remote sensing using broadband echosounders by providing a distinct calibration and characterisation technique and exploring a new acoustic classifier. The main goals achieved were

1. Development of a technique to calibrate the target strength measurements of a broadband echosounder and extract the frequency response of target strength of a target compensated for the transducer directivity for its position. This was achieved by calculating the system response function for all off-axis positions within the main lobe using a calibration sphere. Instead of a mathematical function, the system response function was used to compensate the

measurements. The technique was explored for fast and slow ramp transmission settings.

2. The system response function was extended to measure the effective geometrical and directional parameters of the transducer. In the same calibration experiment, the difference between the measured and modelled beam pattern was minimised in the least-squares sense by allowing the geometrical parameter to vary within a specified range. The effective GP of the transducer was found to be constant across the entire frequency.

3. A new acoustic variable; residual phase was quantified to visualise the target induced phase distortion in the backscattered echo. This was done to overcome difficulties in interpreting the absolute phase due to its inherent phase wrapping and high fluctuations in the differential phase.

4. A Simrad EK80 broadband echosounder was calibrated for the phase measurements. Later the frequency response of all the three-phase variables (absolute, differential and residual) were derived for two sphere targets in all the positions within the main lobe. This was obtained by using the system response in the complex form.

5. The developed technique was applied to derive the in situ $TS(f)$ of different organisms from the Great Australian Bight region. For the purpose, the system response was calculated by suspending a sphere underneath the transducer and allowing it to move to all positions.

6. The frequency response of the target strength and phase of in-situ micronekton from the Southern Ocean region was derived. This was achieved by determining the in-situ system response function of the transceiver in complex form for a large number of target positions. Depending upon the requirement, the magnitude or the complex form of system response function was used in subsequent processing.

7. A technique to combine the acoustic and optical measurements was formulated. The basis was the use of transformation matrices which allowed the rotation and translation of the target position from one coordinate system to the other.

8. The utility of target phase measurements was demonstrated by inverting the

target strength and phase measured for an optically verified target to predict the characteristics.

8.1 Contribution and significance

8.1.1 Calibration for the target strength

Chapter 3 investigates the calibration of a broadband echosounder for the frequency response of the target strength variable. The approach was based on the work of Stanton, and Chu (2008) with the extension that the frequency-dependent system response function was expanded to include the off-axis angles. The performance of the calibrated system was explored using scattering from standard sphere targets, WC22 and WC38, which allowed comparison between the measured and theoretically predicted values. The suggested system response function efficiently includes the beam pattern effect, the amplitude ramping and even the response of the system phase function.

For the transducer used in these tests, the compensated $TS(f)$ achieved with system response function showed improvement in comparison with the modified Bessel function method. The process was stable enough to compensate data beyond the half beamwidth (3.5°). The system response function was found to change when the echosounder's transmit amplitude ramping was changed. However, $TS(f)$ was adequately compensated for the position of the target within the beam by whichever system response function was appropriate to the transmit amplitude ramping used for the measurement.

Calibrating an echosounder in a survey location is difficult, particularly when the instrument accuracy is restricted by the preciseness of the parameters provided by the manufacturer. The result from this particular study indicated that the system response is capable of extracting the compensated $TS(f)$, irrespective of the knowledge of the effective beamwidth.

A somewhat similar concept was adapted by MacLennan, and Svellingen (1986), for a single-beam transducer where the mean sensitivity was determined for the entire beam by partitioning it into seven cross-sections of equal areas. The number of data points was as low as 30. In the current study, even though the sensitivity was averaged for each off-axis bin, the intention was to collect as many samples as possible. Even though a similar result could be achieved with fewer data points, it is not recommended as it could

compromise the accuracy of the calibration result.

8.1.2 Calibration for the target phase

One of the main aims of the thesis was to substantiate the target phase as a new metric in acoustic analysis and apply it to identify a scatterer's characteristics from the backscattered echo. Chapter 5 theoretically and experimentally investigated the application of the system response function for phase extraction and calibration. To the candidate's knowledge, the result comprises the first set of phase measurements undertaken with Simrad EK80 and includes the effects of transducer directivity and 'fast' and 'slow' amplitude ramping. A crucial aspect of this study is that it confirmed the theoretical prediction that the system phase response should be independent of the target position within the transducer's main beam. This is a significant result for fisheries acoustic surveys because any target moving in the acoustic beam would have a consistent phase irrespective of its position within the beam. However, if the target changes orientation when moving through beam possibly both the amplitude and phase response would change depending on the structure of the organism.

Earlier studies had indicated the difficulty of using absolute phase, $\varphi_{bs}(f)$ as a quantitative indicator, as it was prone to the effects of the range and frequency accumulation. To rectify the effect variables such as the rate of change of phase (Barr, & Coombs, 2005), gross phase shifts (Bolus et al., 1982) and phase differences (Atkins et al., 2007) have been proposed each with its own set of merits and limitation. The current study introduced two variables, the differential $DP(f)$ and the residual phase $RP(f)$ to visualise the target induced phase distortion.

$DP(f)$ was calculated by differentiating the absolute phase with respect to the frequency. $RP(f)$ was obtained by subtracting the product of frequency and median of the differential phase from the absolute phase. The obtained spectra of $\varphi_{bs}(f)$, $DP(f)$ and $RP(f)$ for the two spheres (WC22 and WC38) were evaluated through comparison with the respective modelled response. Even though $DP(f)$ exhibited the target-induced phase, this was overshadowed by the resonant induced nulls of the sphere, which made interpretation of the phase at another frequency difficult. The frequency response of $RP(f)$ appeared stable and displayed the more subtle target induced phase variations even near its resonant frequency.

8.1.3 Characterisation of the geometrical and directional parameters of a broadband split-beam transducer

One of the research topics was the development of a broadband specific method for the determination of the transducer parameters. In Chapter 4, the algorithm framework was used to quantify the effective values of the transducer's geometrical (ratio of transducer radius to segment distance) and directional parameters (beamwidth, beam pattern). An optimisation model was formulated that allowed selecting the most suitable geometrical parameter from a set of available values for the minimisation of the cost function. For the specific transducer, the effective geometrical parameter and the beamwidth both were found to be almost independent of frequency. The GP was higher (4 - 5%) from the nominal value, whereas the directional parameter was slightly lower (3 - 4%) than the nominal value. The results were verified by estimating $TS(f)$ with the derived and manufacturer-quoted values. In this case, using the nominal value leads to an under-compensated $TS(f)$ that was rectified by the use of derived effective parameters.

Several studies had earlier quantified the variation of the beamwidth from the nominal values (Ona, & Vestnes, 1985; Reynisson, 1998) for a constant frequency. In these earlier studies, the directivity of a transducer was usually evaluated by mapping the beam at several positions and fitting it with a mathematical function (bicubic spine or a modified Bessel function) (Degnbol, 1988; Kieser, & Ona, 1988; MacLennan, & Svellingen, 1986; Ona, 1990a). In the case of a broadband echosounder, uncertainties in the parameters due to the wide frequency bandwidth need to be tested and verified. The model employed in this study is simple and could be useful in a survey for assessing the beamwidth even with fewer data points across the acoustic beam. Measurements should be carried out on other transducers to substantiate the model.

8.1.4 In situ target strength and residual phase of optically verified micronekton

Although the results in Chapter 3 and Chapter 5 demonstrated the capability of the proposed algorithm for the calibration and processing of broadband echosounder data for target strength and phase measurements, it remained pertinent to investigate the practicality of applying the proposed algorithm to in-situ live micronekton. Chapter 6 uses a preliminary set of data collected from mesopelagic depths of the Great Australian Bight to extract the frequency-dependent target strength from selected single targets (Verma et al., 2017). Plausible results were obtained for targets with different acoustic scattering features; however, in the absence of any visual verification, the target types could not be

verified. The problem motivated the installation of an EK80 broadband echosounder on the PLAOS platform to allow simultaneous optical and acoustic sampling of the mesopelagic biota. This formed the basis for chapter 7.

Chapter 7 used acoustic data taken from the improved PLAOS system deployed in the Southern Ocean that provided live video recordings and real-time images of the organisms sampled by the echosounder. An attempt was made to ensure that the signatures of only optically identified micronekton were processed. The 3D transformation model allowed checking for the identity of the acoustic targets, yet the investigation of just 2 hours of data proved to be a substantial effort. Even though hundreds of organisms were found by the echosounder, they rarely matched the concurrent photo. Moreover, the use of a single camera limited range resolution and organism avoidance made the task difficult.

The first set of acoustic signatures (frequency response of target strength and residual phase) from different types of organisms (fish and small gas-filled targets) appear promising, as they were consistent for all the pings and at different depths. The new variable, residual phase, proved to be more prone to noise than the target strength but gave consistent results from ping to ping when the signal to noise ratio was sufficient. Squid were strongly attracted to the calibration sphere, which made it impossible to obtain uncontaminated acoustic signatures of these animals from data collected during this deployment. However, this should be possible during future PLAOS deployments without calibration spheres.

The underlying algorithms on which most acoustic scattering models are based inherently calculate both the amplitude and phase of the scattering function, but usually only output the amplitude component in the form of target strength. Relatively simple modifications, such were made here for a resonant bubble model, would be required to allow these models to also output the modelled phase so that this can be compared to measured phase as an aid to target classification.

8.2 Limitations

1. A significant aspect of the echosounder is the application for echo integration for abundance and density estimates that requires calibration of the equivalent beam angle. The evaluation of the effective equivalent beam angle involves the determination of the actual angles evaluated by a geometrical method instead of

the split-beam processing as exhibited by Simmonds (1984) and Ona, and Vestnes (1985) or even Reynisson (1998). This requires an independent measurement of the absolute position of the target. In the study undertaken, the electrical angles were used and hence estimating volume backscattering strength using a system calibrated by this method is not recommended unless an independent measurement of equivalent beam angle is available.

2. In fisheries acoustics, elliptical or rectangular transducers are sometimes used. The system response in this study was formulated for the off-axis angle of circular transducers. Nonetheless, the process can easily be extended to non-circular transducers by making appropriate adjustments to include the angles along the major and minor axis.

3. The resonance peak of the calibration sphere introduces an artefact into the system response function that leads to unwanted spikes in the target response curves. During the experiment, the peak was removed by ignoring the corresponding frequency region, but this could be undesirable in a situation where the system bandwidth includes multiple calibration sphere resonances. Methods to avoid this could comprise interpolating the system response in the resonant frequency region or using multiple calibration spheres with resonances at different frequencies.

4. The 3D transformation model presented in chapter 7 provided a reasonable estimate of the expected location of acoustically sampled objects in the still photographs. There is, however, still a certain degree of ambiguity in the identification of the target. This was mainly due to the use of the single-lens camera, which lacked a sense of depth. Moreover, the model was complicated due to the inclusion of several coordinate systems in the transformation model. To avoid this ambiguity in future, further research should be conducted using synchronised stereo cameras.

8.3 Summary of thesis contribution

The contributions achieved in the thesis are described below:

1. Developing a method to calibrate a broadband echosounder that allows it to measure both the amplitude (target strength) and phase of a target's scattering

response as a function of frequency (Chapter 3 and Chapter 5).

2. Establishing that this method correctly compensates the target strength measurements for the target's position in the beam and that, at least for the tested transducer, the phase measurements are independent of the position of the target in the beam. Theory suggests that this latter result is likely to apply to the majority of fisheries transducers, providing the target is within the main lobe of the beam pattern (Chapter 5).

3. Developing a measure of the phase response of a target (residual phase) that minimises distortions caused by uncertainties in the measured range to the target, making it much easier to compare the measured phase response to scattering models (Chapter 5).

4. Demonstrating that these methods can be applied to in-situ field data from descending platforms. These field data sets included small, resonant targets, from which consistent results were obtained for both target strength and phase as the target's range and position in the beam changed, and larger optically verified targets such as fish and squid that had much greater ping to ping variation because of their larger size and rapid movement, but gave results consistent with expectations. For the resonant targets, the measured phase responses were consistent with the predictions of a scattering model that was fitted to the measured frequency-dependent target strength (Chapter 6 and Chapter 7).

These contributions required several additional tasks to be carried out, including:

5. Characterising the geometrical and directional parameters of a split-beam broadband echosounder and verifying that the effective GP of the transducer is independent of frequency (Chapter 4).

6. Developing a method to convert a target's three-dimensional coordinates measured by an echosounder to its two-dimensional pixel coordinates in a photograph (Chapter 7).

7. Extending the theoretical numerical acoustic scattering model of a gas-filled sphere to predict the frequency response of the residual phase (Chapter 7).

8. Participating in two research surveys during which broadband acoustic data were

collected from the mesopelagic zone using descending platforms. In the second survey, the platform also acquired still photographs and video, allowing optical verification of targets. (Chapter 6 and Chapter 7).

8.4 Recommendation for future work

Target phase is not routinely used in the detection and classification of marine organisms, however, for the transducer used in this project, it was found to be unaffected by the position of the target in the main lobe. This result is significant for the classification of targets moving within the acoustic beam. This is in accordance with theoretical results for ideal piston transducers (Kinsler et al., 1999), but it is important that it be experimentally verified for other transducers.

Many different numerical scattering models are described in the literature, appropriate to a variety of marine organisms (Jech et al., 2015). Although backscattered signals from a range of target types were collected during the deployments described in this thesis, only the simplest numerical scattering model (gas-filled sphere) was matched to the measured data. Straightforward extensions to other scattering models should allow them to be used to predict the frequency-dependent phase response of other types of targets. Some of the models that could be explored in this respect are Distorted Wave Born Approximation (Chu et al., 1993; Stanton et al., 1993), Kirchhoff approximation (Foote, & Francis, 2002) and the Finite element method (Ihlenburg, 2006). The weak targets, which are modelled as liquid-filled shapes, are ecologically and biologically important so this would greatly extend the applicability of this method.

Lately, there has been an increase in the use of deep profiling platforms and towed bodies (Fernandes et al., 2003). Accurate interpretation of the output from broadband echosounders mounted on these platforms requires that any pressure-dependent effects on the transducer be compensated for by calibrating the system for both the target strength (Haris et al., 2017) and phase across all depths (Dalen et al., 2003; Kloser, 1996; Koslow et al., 1997). This would enable an accurate estimation of the abundance and remove the uncertainties. The determination of depth sensitivity would be straight forward with the system utilised in chapter 7 and would require analysing the data with respect to the depth of the echosounder.

The measurement of the acoustic signature of live in-situ squid shows the potential of the broadband acoustic method. However, the presence of the calibration sphere

restricted the usefulness of the data. The work could be further explored by carrying out other PLAOS deployments without a calibration sphere.

One of the challenges of fisheries acoustics is developing specifies level classification algorithms using both target strength and phase, and investigation of how effective they are compared to methods that rely solely on target strength.

8.5 Conclusions

The thesis aimed at presenting an improved processing and analysis technique for the derivation of the target strength and phase spectra using a broadband echosounder. The system response function was flexible and included provision for the extraction of both the target strength and phase. The calibrations of the phase and the target strength were derived by using the obtained complex transfer function, which also allowed appropriate compensation for the target strength measurements. The method was simple but as accurate as of the compensation achieved with the directivity pattern models. The technique was successful even in the case of different ramp settings. The evidence supporting the flexibility of the method with both fast and slow ramped transmit signals was encouraging. The technique described was shown to be in good agreement with the standard beam models (Bessel function and LOBE algorithm).

The non-linear optimisation model allowed verification of the effective geometrical and the directional parameters of the transducer. The inversion algorithm had to deal with a large number of variables to represent the directionality for each frequency and angle component. The obtained parameters provided a snapshot of the variability of the beam parameters within the frequency. The assumption of the broadband split-beam echosounder as a constant geometrical parameter transducer was confirmed.

The thesis provides the first set of phase measurements made with the Simrad EK80 scientific echosounders. The ‘residual phase’ was introduced as a new phase variable. The consistency of phase obtained across all off-axis angles from the standard sphere provides a basis to the hypothesis of phase as a target classifier made at the beginning of the research. The method was accurately implemented using a set of acoustic-sensors to characterise marine organism from the open ocean, which demonstrates the success of the method. The consistent target strength and residual phase of the real organisms across different pings and the matching of both the variables to the output of the numerical scattering model verified the method for the case of resonant targets.

List of Agreements

SPRINGER NATURE LICENSE TERMS AND CONDITIONS

Sep 17, 2019

This Agreement between Curtin University -- Arti Verma ("You") and Springer Nature ("Springer Nature") consists of your license details and the terms and conditions provided by Springer Nature and Copyright Clearance Center.

License Number	4666550527605
License date	Sep 12, 2019
Licensed Content Publisher	Springer Nature
Licensed Content Publication	Acoustics Australia
Licensed Content Title	Potential Use of Broadband Acoustic Methods for Micronekton Classification
Licensed Content Author	Arti Verma, Rudy J. Kloser, Alec J. Duncan
Licensed Content Date	Jan 1, 2017
Licensed Content Volume	45
Licensed Content Issue	2
Type of Use	Thesis/Dissertation
Requestor type	academic/university or research institute
Format	print and electronic
Portion	full article/chapter
Will you be translating?	no
Circulation/distribution	1000 - 1999
Author of this Springer Nature content	yes
Title	Potential Use of Broadband Acoustic Methods for Micronekton Classification
Institution name	Curtin University
Expected presentation date	Sep 2019
Order reference number	0814-6039
Requestor Location	Curtin University Department of Physics and Astronomy Kent Street Bentley Perth, WA 6102 Australia Attn: Curtin University
Total	0.00 AUD

Terms and Conditions

Springer Nature Customer Service Centre GmbH
Terms and Conditions

This agreement sets out the terms and conditions of the licence (the **Licence**) between you and **Springer Nature Customer Service Centre GmbH** (the **Licensor**). By clicking 'accept' and completing the transaction for the material (**Licensed Material**), you also confirm your acceptance of these terms and conditions.

1. Grant of License

1. 1. The Licensor grants you a personal, non-exclusive, non-transferable, world-wide licence to reproduce the Licensed Material for the purpose specified in your order only. Licences are granted for the specific use requested in the order and for no other use, subject to the conditions below.

1. 2. The Licensor warrants that it has, to the best of its knowledge, the rights to license reuse of the Licensed Material. However, you should ensure that the material you are requesting is original to the Licensor and does not carry the copyright of another entity (as credited in the published version).

1. 3. If the credit line on any part of the material you have requested indicates that it was reprinted or adapted with permission from another source, then you should also seek permission from that source to reuse the material.

2. Scope of Licence

2. 1. You may only use the Licensed Content in the manner and to the extent permitted by these Ts&Cs and any applicable laws.

2. 2. A separate licence may be required for any additional use of the Licensed Material, e.g. where a licence has been purchased for print only use, separate permission must be obtained for electronic re-use. Similarly, a licence is only valid in the language selected and does not apply for editions in other languages unless additional translation rights have been granted separately in the licence. Any content owned by third parties are expressly excluded from the licence.

2. 3. Similarly, rights for additional components such as custom editions and derivatives require additional permission and may be subject to an additional fee. Please apply to Journalpermissions@springernature.com/bookpermissions@springernature.com for these rights.

2. 4. Where permission has been granted **free of charge** for material in print, permission may also be granted for any electronic version of that work, provided that the material is incidental to your work as a whole and that the electronic version is essentially equivalent to, or substitutes for, the print version.

2. 5. An alternative scope of licence may apply to signatories of the STM Permissions Guidelines, as amended from time to time.

3. Duration of Licence

3. 1. A licence for is valid from the date of purchase ('Licence Date') at the end of the relevant period in the below table:

Scope of Licence	Duration of Licence
Post on a website	12 months
Presentations	12 months
Books and journals	Lifetime of the edition in the language purchased

4. Acknowledgement

4. 1. The Licensor's permission must be acknowledged next to the Licenced Material in print. In electronic form, this acknowledgement must be visible at the same time as the figures/tables/illustrations or abstract, and must be hyperlinked to the journal/book's

homepage. Our required acknowledgement format is in the Appendix below.

5. Restrictions on use

5. 1. Use of the Licensed Material may be permitted for incidental promotional use and minor editing privileges e.g. minor adaptations of single figures, changes of format, colour and/or style where the adaptation is credited as set out in Appendix 1 below. Any other changes including but not limited to, cropping, adapting, omitting material that affect the meaning, intention or moral rights of the author are strictly prohibited.

5. 2. You must not use any Licensed Material as part of any design or trademark.

5. 3. Licensed Material may be used in Open Access Publications (OAP) before publication by Springer Nature, but any Licensed Material must be removed from OAP sites prior to final publication.

6. Ownership of Rights

6. 1. Licensed Material remains the property of either Licensor or the relevant third party and any rights not explicitly granted herein are expressly reserved.

7. Warranty

IN NO EVENT SHALL LICENSOR BE LIABLE TO YOU OR ANY OTHER PARTY OR ANY OTHER PERSON OR FOR ANY SPECIAL, CONSEQUENTIAL, INCIDENTAL OR INDIRECT DAMAGES, HOWEVER CAUSED, ARISING OUT OF OR IN CONNECTION WITH THE DOWNLOADING, VIEWING OR USE OF THE MATERIALS REGARDLESS OF THE FORM OF ACTION, WHETHER FOR BREACH OF CONTRACT, BREACH OF WARRANTY, TORT, NEGLIGENCE, INFRINGEMENT OR OTHERWISE (INCLUDING, WITHOUT LIMITATION, DAMAGES BASED ON LOSS OF PROFITS, DATA, FILES, USE, BUSINESS OPPORTUNITY OR CLAIMS OF THIRD PARTIES), AND
WHETHER OR NOT THE PARTY HAS BEEN ADVISED OF THE POSSIBILITY OF SUCH DAMAGES. THIS LIMITATION SHALL APPLY NOTWITHSTANDING ANY FAILURE OF ESSENTIAL PURPOSE OF ANY LIMITED REMEDY PROVIDED HEREIN.

8. Limitations

8. 1. ***BOOKS ONLY:*** Where **'reuse in a dissertation/thesis'** has been selected the following terms apply: Print rights of the final author's accepted manuscript (for clarity, NOT the published version) for up to 100 copies, electronic rights for use only on a personal website or institutional repository as defined by the Sherpa guideline (www.sherpa.ac.uk/romeo/).

9. Termination and Cancellation

9. 1. Licences will expire after the period shown in Clause 3 (above).

9. 2. Licensee reserves the right to terminate the Licence in the event that payment is not received in full or if there has been a breach of this agreement by you.

Appendix 1 — Acknowledgements:

For Journal Content:
Reprinted by permission from [**the Licensor**]: [**Journal Publisher** (e.g. Nature/Springer/Palgrave)] [**JOURNAL NAME**] [**REFERENCE CITATION** (Article name, Author(s) Name), [**COPYRIGHT**] (year of publication)

For **Advance Online Publication papers:**
Reprinted by permission from [**the Licensor**]: [**Journal Publisher** (e.g. Nature/Springer/Palgrave)] [**JOURNAL NAME**] [**REFERENCE CITATION** (Article name, Author(s) Name), [**COPYRIGHT**] (year of publication), advance online publication, day month year (doi: 10.1038/sj.[JOURNAL ACRONYM].)

For Adaptations/Translations:
Adapted/Translated by permission from [**the Licensor**]: [**Journal Publisher** (e.g. Nature/Springer/Palgrave)] [**JOURNAL NAME**] [**REFERENCE CITATION** (Article name, Author(s) Name), [**COPYRIGHT**] (year of publication)

Note: For any republication from the British Journal of Cancer, the following credit line style applies:

Reprinted/adapted/translated by permission from [**the Licensor**]: on behalf of Cancer Research UK: : [**Journal Publisher** (e.g. Nature/Springer/Palgrave)] [**JOURNAL NAME**] [**REFERENCE CITATION** (Article name, Author(s) Name), [**COPYRIGHT**] (year of publication)

For **Advance Online Publication** papers:
Reprinted by permission from The [**the Licensor**]: on behalf of Cancer Research UK: [**Journal Publisher** (e.g. Nature/Springer/Palgrave)] [**JOURNAL NAME**] [**REFERENCE CITATION** (Article name, Author(s) Name), [**COPYRIGHT**] (year of publication), advance online publication, day month year (doi: 10.1038/sj.[JOURNAL ACRONYM])

For Book content:
Reprinted/adapted by permission from [**the Licensor**]: [**Book Publisher** (e.g. Palgrave Macmillan, Springer etc) [**Book Title**] by [**Book author**(s)] [**COPYRIGHT**] (year of publication)

Other Conditions:

Version 1.2

Questions? customercare@copyright.com or +1-855-239-3415 (toll free in the US) or +1-978-646-2777.

List of References

Abramowitz, M., and Irene A. Stegun, eds. (1965). *Handbook of mathematical functions with formulas, graphs, and mathematical tables*: US Government printing office, 1948.

Al-Nashi, H. (1989). Phase unwrapping of digital signals. *IEEE Transactions on Acoustics, Speech, and Signal Processing, 37*(11), 1693-1702. doi: https://doi.org/10.1109/29.46552

Anderson, V. C. (1950). Sound Scattering from a Fluid Sphere. *The Journal of the Acoustical Society of America, 22*(4), 426-431. doi: https://doi.org/10.1121/1.1906621

Andreeva, I. (1974). Scattering of sound by air bladders of fish in deep sound-scattering ocean layers. *Sov. Phys. Acoust, 10*(1), 17-20. doi:

Anthony, K. J., et al. (1994). The mid-slope demersal fish community off southeastern Australia. *Deep Sea Research Part I: Oceanographic Research Papers, 41*(1), 113-141. doi: https://doi.org/10.1016/0967-0637(94)90029-9

Atkins, P. R., et al. (2007). Transmit-Signal Design and Processing Strategies for Sonar Target Phase Measurement. *IEEE Journal of Selected Topics in Signal Processing, 1*(1), 91-104. doi: https://doi.org/10.1109/jstsp.2007.897051

Au, W. W., & Benoit-Bird, K. J. (2003). Acoustic backscattering by Hawaiian lutjanid snappers. II. Broadband temporal and spectral structure. *The Journal of the Acoustical Society of America, 114*(5), 2767-2774. doi: https://doi.org/10.1121/1.1614257

Au, W. W., & Benoit-Bird, K. J. (2008). Broadband backscatter from individual Hawaiian mesopelagic boundary community animals with implications for spinner dolphin foraging. *The Journal of the Acoustical Society of America, 123*(5), 2884-2894. doi: https://doi.org/10.1121/1.2902187

Baik, K. (2013). Comment on "Resonant acoustic scattering by swimbladder-bearing fish" J. Acoust. Soc. Am. 64, 571-580 (1978) (L). *Journal of the Acoustical*

Society of America, 133(1), 5-8. doi: https://doi.org/10.1121/1.4770261

Barange, M., et al. (1996). Empirical determination of in situ target strengths of three loosely aggregated pelagic fish species. *ICES Journal of Marine Science:, 53*(2), 225-232. doi: https://doi.org/10.1006/jmsc.1996.0026

Barham, E. G. (1966). Deep scattering layer migration and composition: observations from a diving saucer. *Science, 151*(3716), 1399-1403. doi: https://doi.org/10.1126/science.151.3716.1399

Barr, R., & Coombs, R. F. (2005). Target phase: An extra dimension for fish and plankton target identification. *The Journal of the Acoustical Society of America, 118*(3), 1358-1371. doi: https://doi.org/10.1121/1.1979503

Bassett, C., et al. (2017). Broadband echosounder measurements of the frequency response of fishes and euphausiids in the Gulf of Alaska. *ICES Journal of Marine Science*. doi: https://doi.org/10.1093/icesjms/fsx204

Batzler, W., & Barham, E. (1963). Acoustic Scattering from a Layer of Siphonophores. *The Journal of the Acoustical Society of America, 35*(5), 792-793. doi: https://doi.org/10.1121/1.2142469

Béhagle, N., et al. (2016). Acoustic micronektonic distribution is structured by macroscale oceanographic processes across 20–50 S latitudes in the South-Western Indian Ocean. *Deep Sea Research Part I: Oceanographic Research Papers, 110*, 20-32. doi: https://doi.org/10.1016/j.dsr.2015.12.007

Béhagle, N., et al. (2014). Mesoscale features and micronekton in the Mozambique Channel: An acoustic approach. *Deep Sea Research Part II: Topical Studies in Oceanography, 100*(0), 164-173. doi: https://doi.org/10.1016/j.dsr2.2013.10.024

Benfield, M. C., et al. (2003). Distributions of physonect siphonulae in the Gulf of Maine and their potential as important sources of acoustic scattering. *Canadian Journal of Fisheries and Aquatic Sciences, 60*(7), 759-772. doi: https://doi.org/10.1139/f03-065

Benoit-Bird, K. J., & Au, W. W. (2001). Target strength measurements of Hawaiian mesopelagic boundary community animals. *The Journal of the Acoustical Society of America, 110*(2), 812-819. doi: https://doi.org/10.1121/1.1382620

Bodholt, H. (2002). *The effect of water temperature and salinity on echo sounder measurements.* Paper presented at the ICES Symposium on Acoustics in Fisheries.

Bodholt, H., & Solli, H. (1992). *Application of the split-beam technique for in-situ, target-strength measurements.* Paper presented at the World Fisheries Congress, Athens.

Bolus, R. L., et al. (1982). Subbottom acoustic impedance profiles from magnitude and phase analysis of echoes. *IEEE Transactions on Geoscience and Remote Sensing*(3), 338-342. doi: https://doi.org/10.1109/tgrs.1982.350452

Bracewell, R. N. (1986). *The Fourier transform and its applications* (Vol. 31999): McGraw-Hill New York.

Braithwaite, H. (1973). Discrimination between sonar echoes from fish and rocks on the basis of “hard” and “soft” characteristics. *Journal of Sound and Vibration, 27*(4), 549-IN541. doi: https://doi.org/10.1016/0041-624x(74)90109-7

Brierley, A., et al. (1998). Variations in echosounder calibration with temperature, and some possible implications for acoustic surveys of krill biomass. *Ccamlr Science, 5*, 273-281. doi:

Briseño-Avena, C., et al. (2015). ZOOPS-O2: A broadband echosounder with coordinated stereo optical imaging for observing plankton in situ. *Methods in Oceanography, 12*, 36-54. doi: https://doi.org/10.1016/j.mio.2015.07.001

Brodeur, R. D., et al. (2005). Micronekton–What are they and why are they important. *Pac Mar Sci Org Pices Press, 13*, 7-11. doi:

Brodeur, R. D., et al. (1999). Forage fishes in the Bering Sea: distribution, species associations, and biomass trends. *Dynamics of the Bering Sea*, 509-536. doi:

Burdic, W. S. (1991). *Underwater acoustic system analysis*: Prentice Hall.

Butler, J. L., & Pearcy, W. G. (1972). Swimbladder Morphology and Specific Gravity of Myctophids off Oregon. *Journal of the Fisheries Research Board of Canada, 29*(8), 1145-1150. doi: https://doi.org/10.1139/f72-170

Chestnut, P., et al. (1979). A sonar target recognition experiment. *The Journal of the Acoustical Society of America, 66*(1), 140-147. doi: https://doi.org/10.1109/icassp.1979.1170631

Chu, D. (2011). "TS Package", ComputeSolidElasticSphereTS Matlab Gui. from NOAA

Chu, D., & Eastland, G. C. (2015). Calibration of a broadband acoustic transducer with a standard spherical target in the near field. *The Journal of the Acoustical Society of America, 137*(4), 2148-2157. doi: https://doi.org/10.1121/1.4916281

Chu, D., et al. (1993). Further analysis of target strength measurements of Antarctic krill at 38 and 120 kHz: Comparison with deformed cylinder model and inference of orientation distribution. *The Journal of the Acoustical Society of America, 93*(5), 2985-2988. doi: https://doi.org/10.1121/1.405818

Chu, D., & Stanton, T. K. (1998). Application of pulse compression techniques to broadband acoustic scattering by live individual zooplankton. *The Journal of the Acoustical Society of America, 104*(1), 39-55. doi: https://doi.org/10.1121/1.424056

Clay, C. S., & Horne, J. K. (1994). Acoustic models of fish: The Atlantic cod (Gadus morhua). *The Journal of the Acoustical Society of America, 96*(3), 1661-1668. doi: https://doi.org/10.1121/1.410245

Conti, S. G., et al. (2005). An improved multiple-frequency method for measuring in situ target strengths. *ICES Journal of Marine Science:, 62*(8), 1636-1646. doi: https://doi.org/10.1016/j.icesjms.2005.06.008

Cook, M. R., et al. (2017). *Coherence-based phase unwrapping for broadband acoustic signals.* Paper presented at the Proceedings of Meetings on Acoustics 173EAA.

Dalen, J., & Bodholt, H. (1991). *Deep towed vehicle for fish abundance estimation concept and testing*.

Dalen, J., et al. (2003). A comparative acoustic-abundance estimation of pelagic redfish (Sebastes mentella) from hull-mounted and deep-towed acoustic systems. *ICES Journal of Marine Science:, 60*(3), 472-479. doi: https://doi.org/10.1016/s1054-3139(03)00045-6

Davison, P., et al. (2015). Mesopelagic fish biomass in the southern California current ecosystem. *Deep Sea Research Part II: Topical Studies in Oceanography, 112*, 129-142. doi: https://doi.org/10.1016/j.dsr2.2014.10.007

Degnbol, P. (1988). *A calibration method for split beam echo sounders including calibration of directivity compensation and level*: Danmarks Fiskeri-og Havundersøgelser.

Demer, D., et al. (2017). Evaluation of a wideband echosounder for fisheries and marine ecosystem science. *ICES Cooperative research report*(336). doi:

Demer, D., et al. (2015). Calibration of acoustic instruments. *ICES Cooperative research report*(326). doi:

Demer, D. A., & Conti, S. G. (2003). Validation of the stochastic distorted-wave Born approximation model with broad bandwidth total target strength measurements of Antarctic krill. *ICES Journal of Marine Science, 60*(3), 625-635. doi: https://doi.org/10.1016/j.icesjms.2003.12.002

Demer, D. A., & Conti, S. G. (2004). Validation of the stochastic distorted-wave Born approximation model with broad bandwidth total target strength measurements of Antarctic krill. *ICES Journal of Marine Science:, 61*(1), 155-156. doi: https://doi.org/10.1016/j.icesjms.2003.12.002

Demer, D. A., & Conti, S. G. (2005). New target-strength model indicates more krill in the Southern Ocean. *ICES Journal of Marine Science:, 62*(1), 25-32. doi: https://doi.org/10.1016/j.icesjms.2004.07.027

Demer, D. A., & Renfree, J. S. (2008). Variations in echosounder–transducer performance with water temperature. *ICES Journal of Marine Science, 65*(6), 1021-1035. doi: https://doi.org/10.1121/1.4787073

Devin Jr, C. (1959). Survey of thermal, radiation, and viscous damping of pulsating air bubbles in water. *The Journal of the Acoustical Society of America, 31*(12), 1654-1667. doi: https://doi.org/10.1121/1.1907675

Diachok, O. (2001). Interpretation of the spectra of energy scattered by dispersed anchovies. *The Journal of the Acoustical Society of America, 110*(6), 2917-2923. doi: https://doi.org/10.1121/1.1413996

Didrikas, T., & Hansson, S. (2004). In situ target strength of the Baltic Sea herring and sprat. *ICES Journal of Marine Science, 61*(3), 378-382. doi: https://doi.org/10.1016/s1054-3139(04)00005-0

Dosso, S. E., et al. (1993). Estimation of ocean-bottom properties by matched-field inversion of acoustic field data. *IEEE Journal of Oceanic Engineering, 18*(3), 232-239. doi: https://doi.org/10.1109/joe.1993.236361

Dunlop, K. M., et al. (2018). Detection and characterisation of deep-sea benthopelagic animals from an autonomous underwater vehicle with a multibeam echosounder: A proof of concept and description of data-processing methods. *Deep Sea Research Part I: Oceanographic Research Papers, 134*, 64-79. doi: https://doi.org/10.1016/j.dsr.2018.01.006

Echoview. (2017). Echoview software, version 8.0 Hobart, Australia.: Echoview Software Pty Ltd (2017).

Ehrenberg, J. (1974). *Two applications for a dual-beam transducer in hydroacoustic fish assessment systems.* Paper presented at the Engineering in the Ocean Environment, Ocean'74-IEEE International Conference on.

Ehrenberg, J. (1981). Analysis of split beam backscattering cross section estimation and single echo isolation techniques. *Applied Physics Labratory, University of Washington, APL-WU, 8108*. doi:

Ehrenberg, J. (1983). A review of in situ target strength estimation techniques. *FAO Fisheries Report, 300*, 85-90. doi: https://doi.org/10.1007/978-94-009-2289-1_17

Ehrenberg, J. E. (1979). A comparative analysis of in situ methods for directly measuring the acoustic target strength of individual fish. *IEEE Journal of Oceanic Engineering, 4*(4), 141-152. doi: https://doi.org/10.1109/joe.1979.1145434

Ehrenberg, J. E., & Torkelson, T. C. (1996). Application of dual-beam and split-beam target tracking in fisheries acoustics. *ICES Journal of Marine Science, 53*(2), 329-334. doi: https://doi.org/10.1080/00344899028438932

Ehrenberg, J. E., & Torkelson, T. C. (2000). FM slide (chirp) signals: a technique for significantly improving the signal-to-noise performance in hydroacoustic assessment systems. *Fisheries Research, 47*(2-3), 193-199. doi:

https://doi.org/10.1016/s0165-7836(00)00169-7

Faran, J. J. (1951). Sound Scattering by Solid Cylinders and Spheres. *The Journal of the Acoustical Society of America, 23*(4), 405-418. doi: https://doi.org/10.1121/1.1906780

Fernandes, P. G., et al. (2002). *Acoustic applications in fisheries science: the ICES contribution.* Paper presented at the ICES Marine Science Symposia.

Fernandes, P. G., et al. (2003). Autonomous underwater vehicles: future platforms for fisheries acoustics. *ICES Journal of Marine Science:, 60*(3), 684-691. doi: 10.1016/s1054-3139(03)00038-9

Flax, L., et al. (1978). Theory of elastic resonance excitation by sound scattering. *The Journal of the Acoustical Society of America, 63*(3), 723-731. doi: https://doi.org/10.1121/1.381780

Foote, K., et al. (1987). Calibration of acoustic instruments for fish density estimation: a practical guide. doi:

Foote, K. G. (1980). Importance of the swimbladder in acoustic scattering by fish: A comparison of gadoid and mackerel target strengths. *The Journal of the Acoustical Society of America, 67*(6), 2084-2089. doi: https://doi.org/10.1121/1.384452

Foote, K. G. (1982). Optimizing copper spheres for precision calibration of hydroacoustic equipment. *The Journal of the Acoustical Society of America, 71*(3), 742-747. doi: https://doi.org/10.1121/1.387497

Foote, K. G. (1983). Linearity of fisheries acoustics, with addition theorems. *The Journal of the Acoustical Society of America, 73*(6), 1932-1940. doi: https://doi.org/10.1016/0198-0254(83)96413-0

Foote, K. G. (1991a). Acoustic sampling volume. *The Journal of the Acoustical Society of America, 90*(2), 959-964. doi: https://doi.org/10.1121/1.2027231

Foote, K. G. (1991b). *Comparison of two 120-kHz split-beam transducers*.

Foote, K. G. (1991c). Summary of methods for determining fish target strength at

ultrasonic frequencies. *ICES Journal of Marine Science, 48*(2), 211-217. doi: https://doi.org/10.1093/icesjms/48.2.211

Foote, K. G. (2000). Standard-target calibration of broadband sonars. *The Journal of the Acoustical Society of America, 108*(5), 2484-2484. doi: https://doi.org/10.1121/1.4743169

Foote, K. G. (2007a). *Acoustic robustness of two standard spheres for calibrating a broadband multibeam sonar.* Paper presented at the OCEANS 2007-Europe.

Foote, K. G. (2007b, 18-21 June 2007). *Acoustic Robustness of Two Standard Spheres for Calibrating a Broadband Multibeam Sonar.* Paper presented at the OCEANS 2007 - Europe.

Foote, K. G., et al. (1986). Measurement of fish target strength with a split-beam echo sounder. *The Journal of the Acoustical Society of America, 80*(2), 612-621. doi: https://doi.org/10.23919/oceans.2011.6107261

Foote, K. G., & Francis, D. T. I. (2002). Comparing Kirchhoff-approximation and boundary-element models for computing gadoid target strengths. *The Journal of the Acoustical Society of America, 111*(4), 1644-1654. doi: https://doi.org/10.1121/1.1458939

Foote, K. G., & MacLennan, D. N. (1984). Comparison of copper and tungsten carbide calibration spheres. *The Journal of the Acoustical Society of America, 75*(2), 612-616. doi: https://doi.org/10.1121/1.390489

Francois, R. E., & Garrison, G. R. (1982). Sound absorption based on ocean measurements. Part II: Boric acid contribution and equation for total absorption. *The Journal of the Acoustical Society of America, 72*(6), 1879-1890. doi: https://doi.org/10.1016/0198-0254(83)90034-1

Furusawa, M. (1988). Prolate spheroidal models for predicting general trends of fish target strength. *Journal of the Acoustical Society of Japan (E), 9*(1), 13-24. doi: https://doi.org/10.1250/ast.9.13

GABRP. (2013). Great Australian Bight Research Program. Retrieved from www.misa.net.au/GAB

Giryn, A. (1982). A Species Classifier of Sea Creatures Compiled on the Basis of Their Echo Sounder Signals. *IEEE transactions on pattern analysis and machine intelligence*(6), 666-671. doi: https://doi.org/10.1109/tpami.1982.4767323

Godø, O. R., et al. (2014). Marine ecosystem acoustics (MEA): quantifying processes in the sea at the spatio-temporal scales on which they occur. *ICES Journal of Marine Science, 71*(8), 2357-2369. doi: https://doi.org/10.1093/icesjms/fsu116

Greenlaw, C. F. (1977). Backscattering spectra of preserved zooplankton. *The Journal of the Acoustical Society of America, 62*(1), 44-52. doi:

Gunderson, D. R. (1993). *Surveys of fisheries resources*: John Wiley & Sons.

Han, J., et al. (2010). *Automated three-dimensional measurement method of in situ fish with a stereo camera.* Paper presented at the OCEANS'10 IEEE SYDNEY.

Handegard, N. O., et al. (2013). Towards an acoustic-based coupled observation and modelling system for monitoring and predicting ecosystem dynamics of the open ocean. *Fish and Fisheries, 14*(4), 605-615. doi: https://doi.org/10.1111/j.1467-2979.2012.00480.x

Haris, K., et al. (2017). Deep-water calibration of echosounders used for biomass surveys and species identification. *ICES Journal of Marine Science, 75*(3), 1117-1130. doi:

Hayman, G., & Robinson, S. P. (2013). Phase calibration of hydrophones by the free-field reciprocity method. *Proceedings of Meetings on Acoustics, 17*(1), 070026. doi: https://doi.org/10.1121/1.4770061

He, P. (1999). Direct measurement of ultrasonic dispersion using a broadband transmission technique. *Ultrasonics, 37*(1), 67-70. doi:

Henderson, M. J., & Horne, J. K. (2007). Comparison of in situ, ex situ, and backscatter model estimates of Pacific hake (Merluccius productus) target strength. *Canadian Journal of Fisheries and Aquatic Sciences, 64*(12), 1781-1794. doi: 10.1139/f07-134

Heyser, R. C. (1969). Loudspeaker phase characteristics and time delay distortion: Part 1. *Journal of the Audio Engineering Society, 17*(1), 30-41. doi:

Hickling, R. (1962). Analysis of echoes from a solid elastic sphere in water. *The Journal of the Acoustical Society of America, 34*(10), 1582-1592. doi: https://doi.org/10.1016/0011-7471(63)90077-9

Hobæk, H., & Forland, T. N. (2013). Characterization of target spheres for broad-band calibration of acoustic systems. *Acta Acustica United with Acustica, 99*(3), 465-476. doi:

Holliday, D. V. (1972). Resonance Structure in Echoes from Schooled Pelagic Fish. *The Journal of the Acoustical Society of America, 51*(4B), 1322-1332. doi:

Holliday, D. V., et al. (1989). Determination of zooplankton size and distribution with multifrequency acoustic technology. *ICES Journal of Marine Science, 46*(1), 52-61. doi:

Horne, J. K. (2000). Acoustic approaches to remote species identification: a review. *Fisheries Oceanography, 9*(4), 356-371. doi:

Horne, J. K., & Clay, C. S. (1998). Sonar systems and aquatic organisms: matching equipment and model parameters. *Canadian Journal of Fisheries and Aquatic Sciences, 55*(5), 1296-1306. doi: 10.1139/f97-322

Ihlenburg, F. (2006). *Finite element analysis of acoustic scattering* (Vol. 132): Springer Science & Business Media.

Islas-Cital, A., et al. (2011a). *Broadband amplitude and phase sonar calibration using LFM pulses for high-resolution study of hard and soft acoustic targets.* Paper presented at the OCEANS 2011 IEEE-Spain.

Islas-Cital, A., et al. (2010, 24-27 May 2010). *Standard target calibration of broad-band active sonar systems in a laboratory tank.* Paper presented at the OCEANS 2010 IEEE - Sydney.

Islas-Cital, A., et al. (2011b). Phase calibration of sonar systems using standard targets and dual-frequency transmission pulses. *The Journal of the Acoustical Society of America, 130*(4), 1880-1887. doi: 10.1121/1.3628325

Jaffe, J., et al. (1998). OASIS in the sea: measurement of the acoustic reflectivity of zooplankton with concurrent optical imaging. *Deep Sea Research Part II: Topical*

Studies in Oceanography, 45(7), 1239-1253. doi:

Jason Phillips, A., et al. (2009). Micronekton community structure in the epipelagic zone of the northern California Current upwelling system. *Progress in Oceanography, 80*(1–2), 74-92. doi:

Jech, J. M., et al. (2003). *Calibrating two scientific echo sounders.* Paper presented at the OCEANS 2003. Proceedings.

Jech, J. M., et al. (2003, 22-26 Sept. 2003). *Comparing two scientific echo sounders.* Paper presented at the OCEANS 2003. Proceedings.

Jech, J. M., et al. (2015). Comparisons among ten models of acoustic backscattering used in aquatic ecosystem research. *The Journal of the Acoustical Society of America, 138*(6), 3742-3764. doi:

Jech, J. M., et al. (2017). Wideband (15–260 kHz) acoustic volume backscattering spectra of Northern krill (Meganyctiphanes norvegica) and butterfish (Peprilus triacanthus). *ICES Journal of Marine Science, 74*(8), 2249-2261. doi: 10.1093/icesjms/fsx050

Johnson, H. R., et al. (1956). Suspended echo-sounder and camera studies of midwater sound scatterers. *Deep Sea Research (1953), 3*(4), 266-272. doi:

Jones, B. A., et al. (2009). Use of the distorted wave Born approximation to predict scattering by inhomogeneous objects: Application to squid. *The Journal of the Acoustical Society of America, 125*(1), 73-88. doi:

Kang, D., et al. (2005). The influence of tilt angle on the acoustic target strength of the Japanese common squid (Todarodes pacificus). *ICES Journal of Marine Science, 62*(4), 779-789. doi: 10.1016/j.icesjms.2005.02.002

Kieser, R., & Ona, E. (1988). *Comparative analysis of split beam data*.

Kinsler, L. E., et al. (1999). Fundamentals of acoustics. *Fundamentals of Acoustics, 4th Edition, by Lawrence E. Kinsler, Austin R. Frey, Alan B. Coppens, James V. Sanders, pp. 560. ISBN 0-471-84789-5. Wiley-VCH, December 1999.*, 560. doi: https://doi.org/10.1063/1.3051072

Kloser, R., et al. (1997). Problems with acoustic target strength measurements of a deepwater fish, orange roughy (Hoplostethus atlanticus, Collett). *ICES Journal of Marine Science, 54*(1), 60-71. doi:

Kloser, R. J. (1996). Improved precision of acoustic surveys of benthopelagic fish by means of a deep-towed transducer. *ICES Journal of Marine Science:, 53*(2), 407-413. doi: https://doi.org/10.1006/jmsc.1996.0057

Kloser, R. J., et al. (2002). Species identification in deep water using multiple acoustic frequencies. *Canadian Journal of Fisheries and Aquatic Sciences, 59*(6), 1065-1077. doi:

Kloser, R. J., et al. (2016). Deep-scattering layer, gas-bladder density, and size estimates using a two-frequency acoustic and optical probe. *ICES Journal of Marine Science*, fsv257. doi:

Kloser, R. J., et al. (2011). In situ measurements of target strength with optical and model verification: a case study for blue grenadier, Macruronus novaezelandiae. *ICES Journal of Marine Science:, 68*(9), 1986-1995. doi: https://doi.org/10.1093/icesjms/fsr127

Kloser, R. J., et al. (2009). Acoustic observations of micronekton fish on the scale of an ocean basin: potential and challenges. *ICES Journal of Marine Science:, 66*(6), 998-1006. doi:

Knudsen, H. P. (2009). Long-term evaluation of scientific-echosounder performance. *ICES Journal of Marine Science, 66*(6), 1335-1340. doi: https://doi.org/10.1093/icesjms/fsp025

Koch, C. (2003). Amplitude and phase calibration of hydrophones by heterodyne and time-gated time-delay spectrometry. *IEEE transactions on ultrasonics, ferroelectrics, and frequency control, 50*(3), 344-348. doi: https://doi.org/10.1109/tuffc.2003.1193629

Koslow, J. A. (2009). The role of acoustics in ecosystem-based fishery management. *ICES Journal of Marine Science*. doi: 10.1093/icesjms/fsp082

Koslow, J. A., et al. (1995). Avoidance of a camera system by a deepwater fish, the orange roughy (Hoplostethus atlanticus). *Deep Sea Research Part I:*

Oceanographic Research Papers, 42(2), 233-244. doi:

Koslow, J. A., et al. (1997). Pelagic biomass and community structure over the mid-continental slope off southeastern Australia based upon acoustic and midwater trawl sampling. *Marine Ecology Progress Series, 146*, 21-35. doi: https://doi.org/10.3354/meps146021

Lavery, A. C., et al. (2017). Exploiting signal processing approaches for broadband echosounders. *ICES Journal of Marine Science, 74*(8), 2262-2275. doi: https://doi.org/10.1093/icesjms/fsx155

Lavery, A. C., et al. (2010). Measurements of acoustic scattering from zooplankton and oceanic microstructure using a broadband echosounder. *ICES Journal of Marine Science:, 67*(2), 379-394. doi: https://doi.org/10.1093/icesjms/fsp242

Lavery, A. C., et al. (2007). Determining dominant scatterers of sound in mixed zooplankton populations. *The Journal of the Acoustical Society of America, 122*(6), 3304-3326. doi: https://doi.org/10.1121/1.2793613

Lee, W.-J., et al. (2012). Orientation dependence of broadband acoustic backscattering from live squid. *The Journal of the Acoustical Society of America, 131*(6), 4461-4475. doi: https://doi.org/10.1121/1.3701876

Lee, W. J., & Stanton, T. K. (2015). Statistics of Broadband Echoes: Application to Acoustic Estimates of Numerical Density of Fish. *IEEE Journal of Oceanic Engineering*(99), 1-15. doi: https://doi.org/10.1109/joe.2015.2476619

Lehodey, P., et al. (2015). Optimization of a micronekton model with acoustic data. *ICES Journal of Marine Science, 72*(5), 1399-1412. doi: 10.1093/icesjms/fsu233

Lehodey, P., et al. (2010). Bridging the gap from ocean models to population dynamics of large marine predators: A model of mid-trophic functional groups. *Progress in Oceanography, 84*(1–2), 69-84. doi: https://doi.org/10.1016/j.pocean.2009.09.008

Lerch, T., et al. (1996). Characterization of spherically focused transducers using an ultrasonic measurement model approach. *Research in Nondestructive Evaluation, 8*(1), 1-21. doi: https://doi.org/10.1007/bf02434041

Love, R. H. (1978a). RESONANT ACOUSTIC SCATTERING BY SWIMBLADDER-BEARING FISH. *Journal of the Acoustical Society of America, 64*(2), 571-580. doi:

Love, R. H. (1978b). Resonant acoustic scattering by swimbladder-bearing fish. *The Journal of the Acoustical Society of America, 64*(2), 571-580. doi:

Luker, L., & Van Buren, A. (1981). Phase calibration of hydrophones. *The Journal of the Acoustical Society of America, 70*(2), 516-519. doi: https://doi.org/10.1121/1.2004688

Lundgren, B., & Nielsen, J. R. (2008). A method for the possible species discrimination of juvenile gadoids by broad-bandwidth backscattering spectra vs. angle of incidence. *ICES Journal of Marine Science, 65*(4), 581-593. doi: https://doi.org/10.1093/icesjms/fsn031

Lyon, R. H. (1983). Progressive phase trends in multi-degree-of-freedom systems. *The Journal of the Acoustical Society of America, 73*(4), 1223-1228. doi: https://doi.org/10.1121/1.389269

Lyon, R. H. (1984). Range and frequency dependence of transfer function phase. *The Journal of the Acoustical Society of America, 76*(5), 1433-1437. doi: https://doi.org/10.1121/1.391426

Macaulay, G. J., et al. (2012). In situ target strength estimates of visually verified orange roughy. *ICES Journal of Marine Science:*. doi: https://doi.org/10.1093/icesjms/fss154

Mackenzie, K. V. (1981). Nine-term equation for sound speed in the oceans. *The Journal of the Acoustical Society of America, 70*(3), 807-812. doi: https://doi.org/10.1121/1.386920

MacLennan, D. (1981). *The theory of solid spheres as sonar calibration targets*: Scottish Fisheries Research Report.

MacLennan, D., & Dunn, J. (1984). Estimation of sound velocities from resonance measurements on tungsten carbide calibration spheres. *Journal of Sound and Vibration, 97*(2), 321-331. doi: https://doi.org/10.1016/0022-460x(84)90325-0

MacLennan, D., & Svellingen, I. (1986). *Simple calibration of a split-beam echo-sounder.* Paper presented at the International Council for the Exploration of the Sea.

MacLennan, D. N. (1982). *Target strength measurements on metal spheres*: Librarian Department of Agriculture and Fisheries for Scotland, Marine ….

MacLennan, D. N. (1990). Acoustical measurement of fish abundance. *The Journal of the Acoustical Society of America, 87*(1), 1-15. doi: https://doi.org/10.1121/1.399285

Maclennan, D. N., et al. (2002). A consistent approach to definitions and symbols in fisheries acoustics. *ICES Journal of Marine Science:, 59*(2), 365-369. doi: https://doi.org/10.1006/jmsc.2001.1158

MacLennan, D. N., & Holliday, D. V. (1996). Fisheries and plankton acoustics: past, present, and future. *ICES Journal of Marine Science, 53*(2), 513-516. doi: https://doi.org/10.1006/jmsc.1996.0074

Marouchos, A., et al. (2016). *A profiling acoustic and optical system (pAOS) for pelagic studies; Prototype development and testing.* Paper presented at the OCEANS 2016-Shanghai.

Marston, P. L., et al. (1990). Rayleigh, Lamb, and whispering gallery wave contributions to backscattering from smooth elastic objects in water described by a generalization of GTD. *Elastic Wave Propagation and Ultrasonic Nondestructive Evaluation*, 211-216. doi:

Martin, L. V., et al. (1996). Acoustic classification of zooplankton. *ICES Journal of Marine Science, 53*(2), 217-224. doi: https://doi.org/10.1575/1912/5351

Martin Traykovski, L. V., et al. (1998). Effect of orientation on broadband acoustic scattering of Antarctic krill Euphausia superba: Implications for inverting zooplankton spectral acoustic signatures for angle of orientation. *The Journal of the Acoustical Society of America, 104*(4), 2121-2135. doi: https://doi.org/10.1121/1.423726

Matsumoto, H. (1990). Characteristics of SeaMARC II phase data. *IEEE Journal of Oceanic Engineering, 15*(4), 350-360. doi: https://doi.org/10.1109/48.103531

McCartney, B. S., & Stubbs, A. R. (1971). Measurements of the acoustic target strengths of fish in dorsal aspect, including swimbladder resonance. *Journal of Sound and Vibration, 15*(3), 397-420. doi: https://doi.org/10.1016/0022-460x(71)90433-0

McClatchie, S., et al. (1996). A re-evaluation of relationships between fish size, acoustic frequency, and target strength. *ICES Journal of Marine Science, 53*(5), 780-791. doi: https://doi.org/10.1006/jmsc.1996.0099

McClatchie, S., et al. (1996). Consequence of swimbladder model choice and fish orientation to target strength of three New Zealand fish species. *ICES Journal of Marine Science, 53*(5), 847-862. doi: https://doi.org/10.1006/jmsc.1996.0106

McClatchie, S., & Dunford, A. (2003). Estimated biomass of vertically migrating mesopelagic fish off New Zealand. *Deep Sea Research Part I: Oceanographic Research Papers, 50*(10–11), 1263-1281. doi: https://doi.org/10.1016/s0967-0637(03)00128-6

McClatchie, S., et al. (2000). Ground truth and target identification for fisheries acoustics. *Fisheries Research, 47*(2), 173-191. doi: https://doi.org/10.1016/s0165-7836(00)00168-5

McGehee, D. E., et al. (1998). Effects of orientation on acoustic scattering from Antarctic krill at 120 kHz. *Deep Sea Research Part II: Topical Studies in Oceanography, 45*(7), 1273-1294. doi: https://doi.org/10.1016/s0967-0645(98)00036-8

Medwin, H., & Clay, C. (1998). Fundamentals of Acoustical Oceanography Academic. *New York*, 11-12. doi:

Midttun, L. (1984). Fish and other organisms as acoustic targets. *Rapports et Procès-Verbaux des Réunions du Conseil International pour l'Exploration de la Mer, 184*, 25-33. doi:

Misund, O. A. (1997). Underwater acoustics in marine fisheries and fisheries research. *Reviews in Fish Biology and Fisheries, 7*(1), 1-34. doi:

Mitri, F., et al. (2008). Investigating the absolute phase information in acoustic wave resonance scattering. *Ultrasonics, 48*(3), 209-219. doi:

Morse, P. M., et al. (1969). Theoretical acoustics: American Society of Mechanical

Engineers Digital Collection.

Murty, K. S. R., & Yegnanarayana, B. (2006). Combining evidence from residual phase and MFCC features for speaker recognition. *IEEE signal processing letters, 13*(1), 52-55. doi: https://doi.org/10.1109/lsp.2005.860538

Nadeborn, W., et al. (1996). A robust procedure for absolute phase measurement. *Optics and Lasers in Engineering, 24*(2-3), 245-260. doi: https://doi.org/10.1016/0143-8166(95)00017-8

Nakken, O., & Olsen, K. (1977). *Target strength measurements of fish*.

Ona, E. (1990a). *Optimal acoustic beam pattern corrections for split beam transducers*.

Ona, E. (1990b). Physiological factors causing natural variations in acoustic target strength of fish. *Journal of the Marine Biological Association of the United Kingdom, 70*(1), 107-127. doi: https://doi.org/10.1017/s002531540003424x

Ona, E. (1999). Methodology for target strength measurements. *ICES Cooperative research report, 235*, 59. doi:

Ona, E., & Vestnes, G. (1985). *Direct measurements of equivalent beam angle on hull-mounted transducers*.

Oppenheim, A. V. (1999). *Discrete-time signal processing*: Pearson Education India.

Oppenheim, A. V., & Lim, J. S. (1981). The importance of phase in signals. *Proceedings of the IEEE, 69*(5), 529-541. doi: https://doi.org/10.1109/proc.1981.12022

Oppenheim, A. V., & Schafer, R. W. (2014). *Discrete-time signal processing*: Pearson Education.

Peña, H., & Foote, K. G. (2008). Modelling the target strength of Trachurus symmetricus murphyi based on high-resolution swimbladder morphometry using an MRI scanner. *ICES Journal of Marine Science, 65*(9), 1751-1761. doi: https://doi.org/10.1093/icesjms/fsn190

Pieper, R. E., et al. (1990). Quantitative zooplankton distributions from multifrequency acoustics. *Journal of Plankton Research, 12*(2), 433-441. doi: https://doi.org/10.1093/plankt/12.2.433

Pikitch, E. K., et al. (2004). Ecosystem-Based Fishery Management. *Science, 305*(5682), 346-347. doi: Ecosystem-Based Fishery Management

Press, W. H., et al. (1988). Numerical recipes in C. *Cambridge University Press, 1*, 3. doi:

Quatieri, T., & Oppenheim, A. (1981). Iterative techniques for minimum phase signal reconstruction from phase or magnitude. *IEEE Transactions on Acoustics, Speech, and Signal Processing, 29*(6), 1187-1193. doi: https://doi.org/10.1109/tassp.1981.1163714

Ramp, H. O., & Wingrove, E. R. (1961). Principles of Pulse Compression. *IRE Transactions on Military Electronics, MIL-5*(2), 109-116. doi: https://doi.org/10.1109/iret-mil.1961.5008328

Raymond Brede, F. H. K., Haakon Solli, and Egil Ona (1990). Target tracking with a split-beam echo sounder *International Symposium on Fisheries Acoustics*. doi: https://doi.org/10.23919/oceans.2011.6107261

Reeder, D. B., et al. (2004). Broadband acoustic backscatter and high-resolution morphology of fish: Measurement and modeling. *The Journal of the Acoustical Society of America, 116*(2), 747-761. doi: https://doi.org/10.1121/1.4784938

Reynisson, P. (1998). Monitoring of equivalent beam angles of hull-mounted acoustic survey transducers in the period 1983–1995. *ICES Journal of Marine Science, 55*(6), 1125-1132. doi: https://doi.org/10.1006/jmsc.1998.0369

Robison, B. H., et al. (1998). Seasonal abundance of the siphonophore, Nanomia bijuga, in Monterey Bay. *Deep Sea Research Part II: Topical Studies in Oceanography, 45*(8), 1741-1751. doi: https://doi.org/10.1016/s0967-0645(98)80015-5

Rogers, P. J., et al. (2013). *Physical processes, biodiversity and ecology of the Great Australian Bight region: a literature review*: CSIRO (Australia).

Ryan, T. E., et al. (2009). Measurement and visual verification of fish target strength using an acoustic-optical system attached to a trawlnet. *ICES Journal of Marine Science:, 66*(6), 1238-1244. doi: https://doi.org/10.1093/icesjms/fsp122

Sawada, K., et al. (2009). Target-strength, length, and tilt-angle measurements of Pacific

saury (Cololabis saira) and Japanese anchovy (Engraulis japonicus) using an acoustic-optical system. *ICES Journal of Marine Science, 66*(6), 1212-1218. doi: https://doi.org/10.1093/icesjms/fsp079

Sawada, K., et al. (2004). Development of an acoustic-optical system (J-QUEST) for fisheries surveys, 1: Acoustic system. *Technical Report of National Research Institute of Fisheries Engineering (Japan)*. doi:

Sawada, K., et al. (1999). Target strength measurements and modeling of walleye pollock and Pacific hake. *Fisheries science, 65*(2), 193-205. doi: https://doi.org/10.2331/fishsci.65.193

Scoulding, B., et al. (2015). Target strengths of two abundant mesopelagic fish species. *The Journal of the Acoustical Society of America, 137*(2), 989-1000. doi: https://doi.org/10.1121/1.4906177

Sherlock, M., et al. (2014). *An instrumented corer platform for seabed sampling and water column characterisation.* Paper presented at the OCEANS 2014-TAIPEI.

Shi, G., et al. (2006). On the importance of phase in human speech recognition. *IEEE transactions on audio, speech, and language processing, 14*(5), 1867-1874. doi: https://doi.org/10.1109/tsa.2005.858512

Simmonds, E. J. (1984). A comparison between measured and theoretical equivalent beam angles for seven similar transducers. *Journal of Sound and Vibration, 97*(1), 117-128. doi: https://doi.org/10.1016/0022-460x(84)90472-3

Simmonds, J., & MacLennan, D. N. (2005). *Fisheries acoustics: theory and practice*: John Wiley & Sons.

Simrad. (2001). EK60 Scientific echo sounder instruction manual (pp. 246). Simrad Subsea A/S, Horten, Norway.

Simrad. (2016). Simrad EK80 Scientific wide band echo sounder.

Sinclair, E., et al. (1999). Distribution and ecology of mesopelagic fishes and cephalopods. *Dynamics of the Bering Sea (TR Loughlin and K Ohtani, eds.), Alaska Sea Grant College Program AK-SG-99-03, University of Alaska Fairbanks*, 485-508. doi:

Sinclair, E., & Stabeno, P. (2002). Mesopelagic nekton and associated physics of the southeastern Bering Sea. *Deep Sea Research Part II: Topical Studies in Oceanography, 49*(26), 6127-6145. doi: https://doi.org/10.1016/s0967-0645(02)00337-5

Skarbnik, N., et al. (2010). The importance of phase in image processing. *CCIT Report# 773*. doi:

Smith, J. N., et al. (2013). A distorted wave Born approximation target strength model for Bering Sea euphausiids. *ICES Journal of Marine Science:, 70*(1), 204-214. doi: https://doi.org/10.1093/icesjms/fss140

Soule, M., et al. (1995). Evidence of bias in estimates of target strength obtained with a split-beam echo-sounder. *ICES Journal of Marine Science:, 52*(1), 139-144. doi: https://doi.org/10.1016/1054-3139(95)80022-0

Spagnolini, U. (1995). 2-D phase unwrapping and instantaneous frequency estimation. *IEEE Transactions on Geoscience and Remote Sensing, 33*(3), 579-589. doi: https://doi.org/10.1190/geo2016-0185.1

Stansfield, D., & Elliott, A. (2017). *Underwater electroacoustic transducers*: Peninsula Publishing.

Stanton, T. K. (1989). Sound scattering by cylinders of finite length. III. Deformed cylinders. *The Journal of the Acoustical Society of America, 86*(2), 691-705. doi: https://doi.org/10.1121/1.398193

Stanton, T. K. (1990). Sound scattering by spherical and elongated shelled bodies. *The Journal of the Acoustical Society of America, 88*(3), 1619-1633. doi: https://doi.org/10.1121/1.400321

Stanton, T. K. (2012). 30 years of advances in active bioacoustics: A personal perspective. *Methods in Oceanography, 1–2*(0), 49-77. doi: https://doi.org/10.1016/j.mio.2012.07.002

Stanton, T. K., & Chu, D. (2000). Review and recommendations for the modelling of acoustic scattering by fluid-like elongated zooplankton: euphausiids and copepods. *ICES Journal of Marine Science:, 57*(4), 793-807. doi: https://doi.org/10.1006/jmsc.1999.0517

Stanton, T. K., & Chu, D. (2008). Calibration of broadband active acoustic systems using a single standard spherical target. *The Journal of the Acoustical Society of America, 124*(1), 128-136. doi: https://doi.org/10.1109/oceanskobe.2008.4530923

Stanton, T. K., & Chu, D. (2010). Non-Rayleigh echoes from resolved individuals and patches of resonant fish at 2–4 kHz. *IEEE Journal of Oceanic Engineering, 35*(2), 152-163. doi: https://doi.org/10.1109/joe.2009.2035240

Stanton, T. K., et al. (1996). Acoustic scattering characteristics of several zooplankton groups. *ICES Journal of Marine Science:, 53*(2), 289-295. doi: https://doi.org/10.1006/jmsc.1996.0037

Stanton, T. K., et al. (1998). Sound scattering by several zooplankton groups. II. Scattering models. *The Journal of the Acoustical Society of America, 103*(1), 236-253. doi: https://doi.org/10.1121/1.421110

Stanton, T. K., et al. (1993). Average echoes from randomly oriented random-length finite cylinders: Zooplankton models. *The Journal of the Acoustical Society of America, 94*(6), 3463-3472. doi: https://doi.org/10.1121/1.407200

Stanton, T. K., et al. (2000). Acoustic scattering by benthic and planktonic shelled animals. *The Journal of the Acoustical Society of America, 108*(2), 535-550. doi: https://doi.org/10.1121/1.429584

Stanton, T. K., et al. (2012). Resonance classification of mixed assemblages of fish with swimbladders using a modified commercial broadband acoustic echosounder at 1–6 kHz. *Canadian Journal of Fisheries and Aquatic Sciences, 69*(5), 854-868. doi: https://doi.org/10.1139/f2012-013

Stanton, T. K., et al. (1998). Differences between sound scattering by weakly scattering spheres and finite-length cylinders with applications to sound scattering by zooplankton. *The Journal of the Acoustical Society of America, 103*(1), 254-264. doi: https://doi.org/10.1121/1.421135

Takahashi, H., et al. (2004). *Development of a stereo TV camera system to complement fish school measurements by a quantitative echo sounder.* Paper presented at the Oceans' 04 MTS/IEEE Techno-Ocean'04 (IEEE Cat. No. 04CH37600).

Tichy, F., et al. (2003). Non-linear effects in a 200-kHz sound beam and the consequences for target-strength measurement. *ICES Journal of Marine Science, 60*(3), 571-574. doi: https://doi.org/10.1016/s1054-3139(03)00033-x

Toolbox, M. a. S. (2016). Release 2016a The MathWorks, Inc., Natick, Massachusetts, United States.

Tribolet, J. (1977). A new phase unwrapping algorithm. *IEEE Transactions on Acoustics, Speech, and Signal Processing, 25*(2), 170-177. doi:

Tucker, D., & Barnickle, N. (1969). Distinguishing automatically the echoes from acoustically “hard” and “soft” objects with particular reference to the detection of fish. *Journal of Sound and Vibration, 9*(3), 393-397. doi: https://doi.org/10.1016/0022-460x(69)90179-5

Turin, G. (1960). An introduction to matched filters. *IRE transactions on Information theory, 3*(6), 311-329. doi: https://doi.org/10.1109/proc.1976.10274

Überall, H. (1973). Surface waves in acoustics *Physical acoustics* (Vol. 10, pp. 1-60): Academic Press.

Urick, R. J. (1983). *Principles of underwater sound*.

Vagle, S., et al. (1996). A technique for calibration of monostatic echosounder systems. *IEEE Journal of Oceanic Engineering, 21*(3), 298-305. doi: https://doi.org/10.1109/48.508160

Verma, A., et al. (2016). *Developing active broadband acoustic methods to investigate the pelagic zone of the Great Australian Bight.* Paper presented at the 2nd Australasian Acoustical Societies Conference, ACOUSTICS 2016.

Verma, A., et al. (2017). Potential use of broadband acoustic methods for micronekton classification. *Acoustics Australia, 45*(2), 353-361. doi: https://doi.org/10.1007/s40857-017-0105-8

Ward, T. M., et al. (2008). *Ecological importance of small pelagic fishes in the Flinders Current System* (D. o. t. E. a. W. Resources, Trans.): SARDI Aquatic Sciences.

Warren, J. D., et al. (2002). Effect of animal orientation on acoustic estimates of

zooplankton properties. *Oceanic Engineering, IEEE Journal of, 27*(1), 130-138. doi: https://doi.org/10.1109/48.989899

Warren, J. D., & Wiebe, P. H. (2008). Accounting for biological and physical sources of acoustic backscatter improves estimates of zooplankton biomass. *Canadian Journal of Fisheries and Aquatic Sciences, 65*(7), 1321-1333. doi: https://doi.org/10.1139/f08-047

Weston, D. E. (1967). Sound propagation in the presence of bladder fish. *Underwater acoustics, 2*, 55-88. doi: https://doi.org/10.1016/0022-460x(82)90394-7

Williams, A., et al. (2001). Feeding ecology of five fishes from the mid-slope micronekton community off southern Tasmania, Australia. *Marine Biology, 139*(6), 1177-1192. doi: https://doi.org/10.1007/s002270100671

Williams, A., & Koslow, J. A. (1997). Species composition, biomass and vertical distribution of micronekton over the mid-slope region off southern Tasmania, Australia. *Marine Biology, 130*(2), 259-276. doi: https://doi.org/10.1007/s002270050246

Williams, K. L., & Marston, P. L. (1986). Synthesis of backscattering from an elastic sphere using the Sommerfeld–Watson transformation and giving a Fabry–Perot analysis of resonances. *The Journal of the Acoustical Society of America, 79*(6), 1702-1708. doi: https://doi.org/10.1121/1.393231

Wilson, O. B. (1988). *Introduction to theory and design of sonar transducers* (Vol. 3): Peninsula Publishing Los Altos, CA.

Ye, Z. (1997a). Acoustic resonant scattering by an ellipsoid air bubble in a liquid. *Physical Review E, 56*(2), 2318-2320. doi: https://doi.org/10.1103/physreve.56.2318

Ye, Z. (1997b). Low-frequency acoustic scattering by gas-filled prolate spheroids in liquids. *The Journal of the Acoustical Society of America, 101*(4), 1945-1952. doi:

Ye, Z., & Hoskinson, E. (1998). Low-frequency acoustic scattering by gas-filled prolate spheroids in liquids. II. Comparison with the exact solution. *The Journal of the Acoustical Society of America, 103*(2), 822-826. doi: https://doi.org/10.1121/1.421470

Yen, N. c., et al. (1990). Time–frequency analysis of acoustic scattering from elastic objects. *The Journal of the Acoustical Society of America, 87*(6), 2359-2370. doi: https://doi.org/10.1121/1.399082

Young, J., et al. (1996). Biomass of zooplankton and micronekton in the southern bluefin tuna fishing grounds off eastern Tasmania, Australia. *Marine Ecology Progress Series, 138*, 1-14. doi: https://doi.org/10.3354/meps138001

Zakharia, M. E., et al. (1996). Wideband sounder for fish species identification at sea. *ICES Journal of Marine Science, 53*(2), 203-208. doi: https://doi.org/10.1006/jmsc.1996.0023